Quantitative analysis of dynamic tumor cell phenotypes regulated by tumor associated macrophages.

Citation
Luthria, Gaurav. 2021. Quantitative analysis of dynamic tumor cell phenotypes regulated by tumor associated macrophages.. Doctoral dissertation, Harvard University Graduate School of Arts and Sciences.

Permanent link
https://nrs.harvard.edu/URN-3:HUL.INSTREPOS:37368382

Terms of Use

Share Your Story

Accessibility

HARVARD UNIVERSITY
Graduate School of Arts and Sciences

DISSERTATION ACCEPTANCE CERTIFICATE

The undersigned, appointed by the

Division of Medical Sciences

Biomedical Informatics

have examined a dissertation entitled

Quantitative analysis of dynamic tumor cell phenotypes regulated by tumor associated macrophages.

presented by Gaurav Luthria

candidate for the degree of Doctor of Philosophy and hereby certify that it is worthy of acceptance.

Signature: Mikael Pittet (May 5, 2021 15:44 GMT+2)

Typed Name: Dr. Mikael Pittet

Signature: Soumya Raycchaudhuri
Soumya Raycchaudhuri (May 5, 2021 10:34 EDT)

Typed Name: Dr. Soumya Raychaudhuri

Signature: Chirag Patel (May 5, 2021 10:43 EDT)

Typed Name: Dr. Chirag Patel

Signature:

Typed Name: Dr. Brian Bryson

Date: April 29, 2021

Quantitative analysis of dynamic tumor cell phenotypes regulated by tumor associated

macrophages.

A dissertation presented

by

Gaurav Luthria

to

The Division of Medical Sciences

in partial fulfillment of the requirements

for the degree of

Doctor of Philosophy

in the subject of

Biomedical Informatics

Harvard University

Cambridge, Massachusetts

April 2021

Quantitative analysis of dynamic tumor cell phenotypes regulated by tumor associated

macrophages.

Abstract

Cancer cells and the tumor microenvironment (TME) dynamically interact to promote cancer progression. One such cell type demonstrated to create an immunosuppressive TME are tumor-associated macrophages (TAMs). Furthermore, macrophage infiltration has been associated with disease progression, angiogenesis, and metastasis. Methods such as single-cell RNA sequencing and multiplexed histology provide a detailed image of the tumor composition, including spatial co-localization and global ligand-receptor expression between TAMs and tumor cells. Nonetheless, it remains challenging to translate static snapshots of tissue composition into understanding how communication networks operate to coordinate dynamic biological processes.

In this dissertation, I aim to address this challenge by creating a computational pipeline to quantify dynamic phenotypes *in vivo*, focusing on understanding how TAMs influence cancer cell cytoskeletal dynamics and migration. To quantify cytoskeletal changes in individual cancer cells, I developed an integrated pipeline combining *in vivo* confocal (intravital) microscopy, automated tracking of individual microtubules, and multivariate statistics to study dynamics in live xenograft models of cancer. I discovered that in addition to the extracellular matrix, interaction with TAMs can lead to coherent microtubule alignment correlating with increased migration rates in individual cancer cells. Furthermore, I identified specific growth factors and

cytokine signaling mechanisms underlying this phenomenon. Although *in vivo* imaging allows signaling pathways to be monitored and manipulated in real-time, its limited multiplexing prevents global characterization of intercellular communication affecting disease progression. Therefore, I also developed a computational method utilizing known ligand-receptor interactions and single-cell transcriptomic data to understand how intercellular communication changes during biological processes such as cancer progression.

Altogether, this work aims to develop methods to capture and quantify cancer cell dynamics and understand how specific tumor microenvironment components regulate such dynamics. Developing new approaches that can accurately model the TME and detect subtle changes during cancer progression are essential to obtain a complete picture of how cancer cells evade treatment and metastasize.

Table of Contents

Acknowledgements

Throughout this journey, I have been incredibly fortunate to have supportive family, friends, colleagues, and mentors.

I want to thank my adviser, **Dr. Miles Miller**, for his guidance and mentorship during my PhD. Your passion and enthusiasm for research are a constant source of encouragement. You were always available to answer any questions, and I have learned so much from you. Because of your mentorship, I have grown as a critical thinker, writer, and scientist.

I want to thank my advisory committee members. **Dr. Ralph Weissleder**, thank you for introducing me to the Miller lab as a first-year student and remaining by my side, providing honest feedback on how to improve my work and further my career. **Dr. Mikael Pittet**, your expertise on cancer immunology has been invaluable in helping me overcome experimental hurdles and identify approaches to test new hypotheses. **Dr. Michael Talkowski**, thank you for helping me address computational challenges in my project and serving as the chair for my committee. I would also like to thank my dissertation committee members, **Dr. Soumya Raychaudhuri**, **Dr. Chirag Patel**, **Dr. Bryan Bryson**, and **Dr. Mikael Pittet,** for their feedback and scientific insights during my PhD. Additionally, I would like to thank **Dr. Douglas Lauffenburger** and **Dr. Timothy Mitchison** for their ongoing advice and important suggestions during my dissertation work.

I am grateful to have fantastic lab members who taught me new experimental techniques, helped with troubleshooting, and provided guidance. Thank you to **Dr. Ran**

Li, **Dr. Thomas Ng**, **Dr. Stephanie Wang**, **Dr. Michelle Garlin**, **Dr. Rainer Kohler**, **Mark Prytyskach**, and **Jeremy Gungabeesoon** for making my lab experiences exciting and memorable.

To Harvard's Department of Biomedical Informatics and the Bioinformatics and Integrative Genomics PhD program's leadership team, including **Dr. Peter Park**, **Dr. Isaac Kohane**, **Dr. Susanne Churchill**, and **Cathy Haskell**. Thank you for believing in me and allowing me to pursue my PhD here. The BIG program has provided me with a community and resources that have laid the foundations for my success.

I am also thankful for my friends along the east coast, west coast, and between that have made my graduate school years so enjoyable. I especially want to thank my confidante and partner, **Samantha Eng**, and her family for always being by my side, supporting my decisions, and serving as a constant source of motivation.

I want to dedicate this work to **my mom, my dad, my brother, Karan**, and my family in India. Achieving this milestone would not have been possible without your sacrifices and dedicated support. You have always been the foundation of my support system through the ups and downs and instilled in me the most important values and morals. This journey is as much yours as mine, and began long before graduate school and will continue long after.

Chapter 1: Introduction

This thesis details research I have conducted under the mentorship of Dr. Miles Miller on applying computational and imaging methods to quantitatively study how intercellular interactions modulate dynamic properties of cancer cells. Cancer is a dynamic disease, where tumor cells are constantly engaging in transient and long-term communication with other cells over varying distances. Furthermore, this communication can be modulated by extracellular and intracellular perturbations which may drive processes such as cancer metastasis and treatment resistance, the primary causes of cancer-related deaths. Therefore, there is an essential need to understand how local interactions affect cancer cell behavior and dynamic phenotypes to improve cancer outcomes.

I begin this introduction detailing static and dynamic techniques to infer cell-cell communication in mammalian tissue in general, but with a special focus on examples from studies of solid cancers. I review the important successes and challenges of these various methods (sections 1.1-1.5), followed by describing current challenges and the need for new methods that can capture dynamic phenotypes and (1.6-1.7). I conclude with an outline of the remaining chapters(1.8).

1.1 Challenges with studying cell-cell communication in mammalian tissue

New genomic and imaging methods provide increasingly detailed descriptions of the single-cell compositions of mammalian tissues. Initiatives such as the Human Cell Atlas, Tabula Muris, and the Human BioMolecular Atlas Program [1–3] generate maps of tissue composition helpful for quantifying cell-type abundance and organization. Such efforts yield static snapshots of tissue composition helpful for quantifying what cell-types are present and where; what cell-cell communication pathways are likely active; and how features differ across cohorts of tissues. Given the data complexity, computational tools have been essential at every step of analysis. Dimensionality reduction techniques like principal components analysis (PCA), UMAP and t-SNE organize multivariate data to identify cell-types. Co-localization analyses identify patterns in cellular organization. Cross-referencing data with known molecular interactions, for instance defined by a catalogue of curated ligand and receptor relationships, can identify extracellular communication networks and intracellular signaling pathways that may be active.

How can such detailed yet static single-cell maps of tissue structure inform function and causality? Optogenetics has been used with revolutionary success to address this question in neuroscience[4]. Here, I focus on communication outside the brain and largely on examples in the microenvironment of solid cancers. As reviewed elsewhere, methods for dynamic measurements and targeted perturbations[5,6] are key to studying function and causality, generally interpreted by computational models incorporating directional probabilistic relationships (e.g., bayesian and boolean networks[7]) or molecular reaction/diffusion kinetics[8]. Unfortunately, approaches with high

spatiotemporal resolution lose multiplexing ability — the capacity to measure multiple

genes or molecules — which is typically required to understand network-level features

including feedback loops and higher-order signal processing.
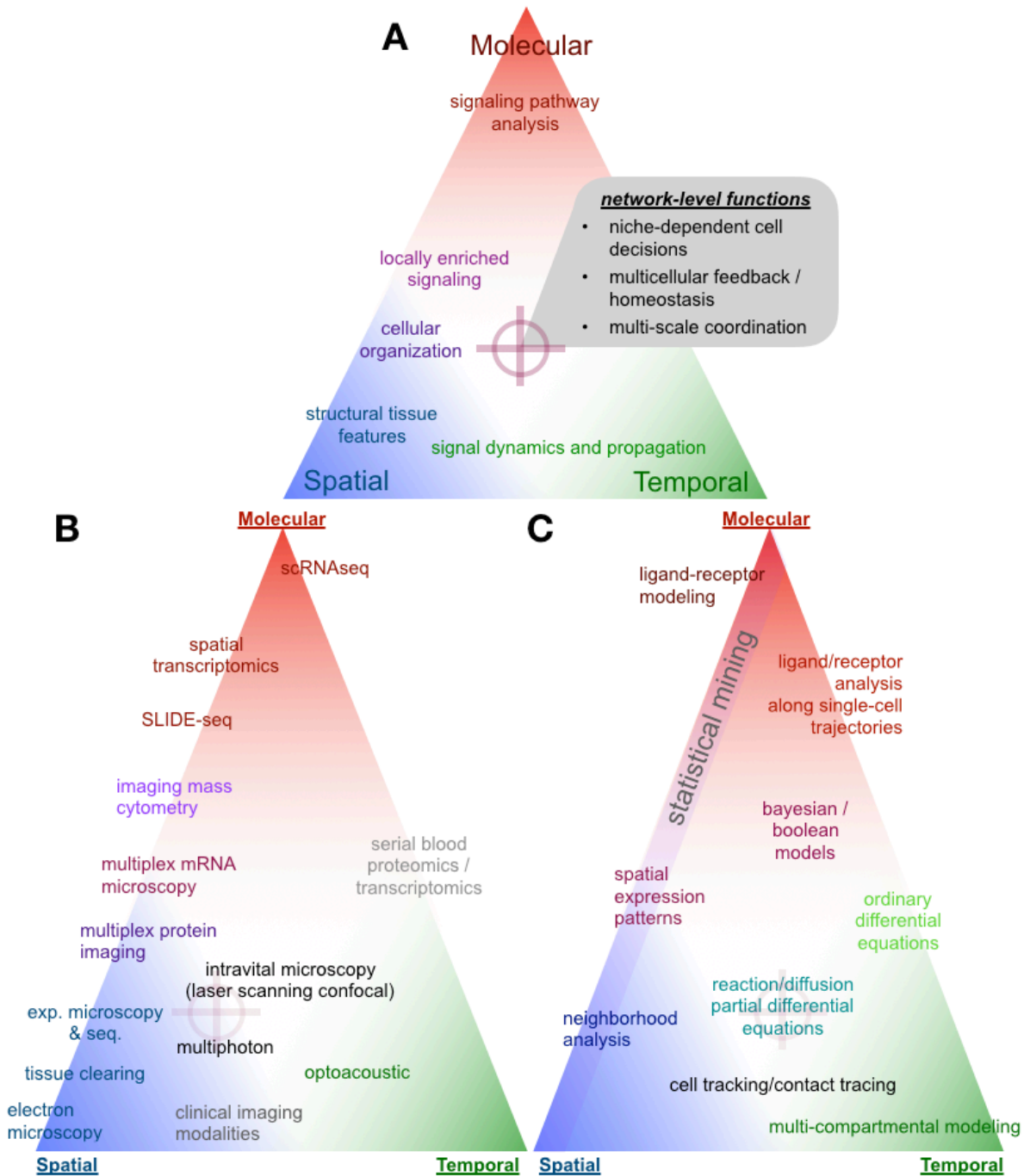
Figure 1-1: Matching biological questions with tools to study cell-cell communication.

Biological concepts (**A**) experimental tools (**B**) and computational methods (**C**) fall along a spectrum of molecular detail and spatiotemporal resolution. Understanding network-level functions of cell-cell communication (see targeted gray box at top) benefits from an integration across methods including in vivo confocal/multiphoton microscopy and reaction/diffusion modeling frameworks. Figure A-1 lists specific examples of experimental and modeling techniques listed in *B-C*.

1.2 Defining network structure / function along axes of space, time, and molecular breadth.

Techniques for studying cell-cell communication, and conceptualization of the biological processes they describe, can be categorized by where they fall along three dimensions of space, time, and molecular multiplexing breadth (**Figure 1-1**). Understanding where a given biological question lies along these axes (**Figure 1-1a**) may help select appropriately matched experimental (**Figure 1-1b**) and computational (**Figure 1-1c**) approaches (see **Figure A-1** for a more detailed version of **Figure 1**). In this review we highlight a subset of experimental strategies (**Figure 1-2**) and computational analyses (**Figure 1-3**) drawn from recent investigations of cell-cell communication that offer insight at varying spatial, temporal, and molecular resolutions.

Communication by cell-surface or secreted proteins and their cognate receptors is an important class of signaling made complicated by its sheer size. >1000 extracellular ligand/receptor (LR) relationships have been catalogued, and many LR pairs involve higher-order protein complexes, overlapping specificities, and competitive binding[9]. Ligands and receptors are conveniently inferred by gene expression, antibodies, and commercial reagents for tissue analysis, compared to communication via small molecules and mechanical force. Therefore many studies of communication networks in mammalian tissues focus on LR relationships, as does this review.
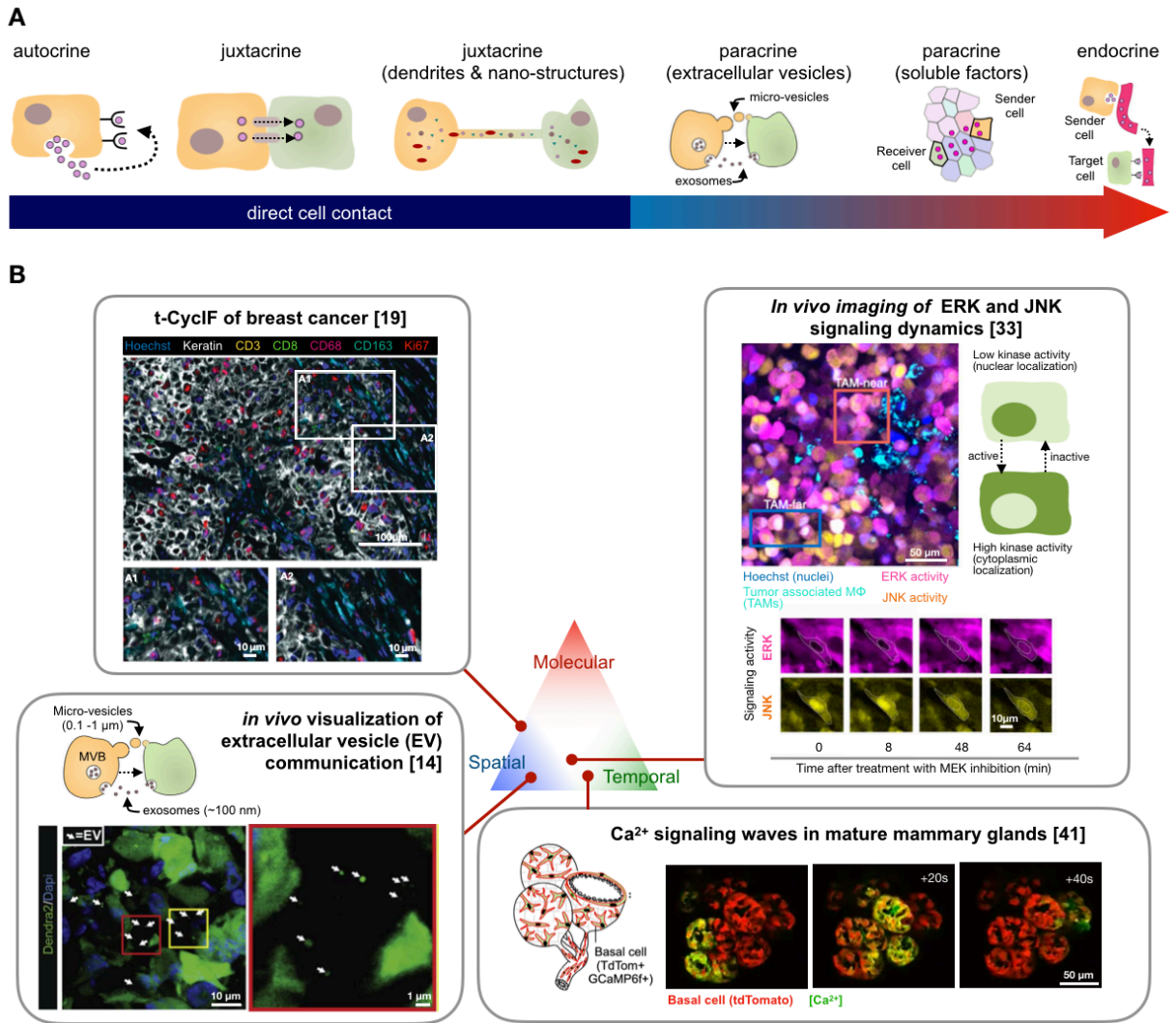
Figure 1-2: Experimental strategies for elucidating cell interactions in tissue. (A) Cartoon

illustrating the range of distances over which cell-cell communication occurs. **(B)** *Top*

left: Tissue cyclic Immunofluorescence (t-CyclF) of triple-negative breast cancer(TNBC) patient

biopsies[10]. Tumor components were stained using panels of dyes and antibodies targeting cell

nuclei (Hoechst), macrophages (CD68, CD163), t-cells (CD3, CD8), epithelium (keratin),

proliferation (Ki67). Adapted from [10]. *Top right:* ERK and JNK signaling activities were measured

in ovarian cancer xenografts via intravital microscopy. Time-lapse imaging revealed adaptive

ERK and JNK signaling in macrophage-proximal tumor cells. Adapted from [11]. *Bottom left*:

Intravital microscopy of extracellular vesicle release and transport in xenograft tumors. Adapted

from [12]. *Bottom right*: Time-lapse confocal microscopy of mouse mammary tissue cultures visualizes coordinated basal cell contraction and calcium signaling propagation. Adapted from [13].

LR signaling is categorized by the distances over which it occurs, classically ranging from autocrine signaling of cells communicating to themselves, to endocrine signaling of secreted ligands reaching receptors at distant tissues (**Figure 1-2a**). New biological understanding, in part driven by high resolution imaging, continues to offer refined perspectives of how processes such as cellular protrusions[14], extracellular vesicle budding[15], and extracellular matrix properties [12] all influence intercellular LR behaviors.

1.3 scRNAseq maps of cell-cell communication

Techniques best suited for global molecular characterization at a single-cell level generally lack information about spatial organization and temporal dynamics, but are ideal for quantifying cell-types and broad programs of cell communication. scRNAseq has become the most popular technique for these objectives, and measures the gene expression of thousands of individual cells from tissue that has been digested into a single-cell suspension[16–19]. Numerous reports use scRNAseq to infer cell-cell communication by referencing a curated list of LR pairs from external databases[9,15,20–22].

A typical workflow for these studies begins with data preprocessing (quality control, normalization), dimensionality reduction (TSNE, SPRING), and unsupervised clustering (hierarchical or k-means clustering) to determine cell types. Each LR pair is then systematically evaluated between and within different cell types. Multiple scoring strategies have been employed to assess the strength of a particular LR interaction. In general, if a gene encoding a ligand is highly expressed in one cell type, while the gene encoding the cognate receptor is highly expressed in another cell type, the interaction between two cell types for that particular LR pair is enriched. Scoring functions range from a simple product of ligand and receptor expressions[20] to more complicated functions that mitigate bias or weigh specific types of interactions such as those between receptors and extracellular matrix components[15]. Statistical significance calculations also vary between different methods, including parametric tests (i.e., regression, t-test), non-parametric tests (i.e., wilcoxon ranksum), and permutation-based methods[9]. Because thousands of LR interactions are scored simultaneously, one

concern that arises is the high rate of false positives, and therefore, it is imperative for statistical significance analysis to correct for multiple hypotheses.

Workflow variations incorporate additional information to improve predictions. CellPhoneDB includes multi-subunit LR complexes[23], and CellChat incorporates soluble agonists, antagonists, as well as stimulatory and inhibitory co-receptors to identify enriched interactions[24]. ICELLNET enables the prediction of cell interactions across different scRNAseq and bulk RNAseq datasets[25]. Methods such as RNAmagnet use a composite LR "adhesion" score to predict the attraction between different cell types[15]. In addition to identifying potential LR pairs mediating directional communication between cells, graph theory methods have also been applied to study the topology of intercellular communication networks. Specifically, graphical properties such as centrality, transitivity, and information flow can identify key cell-types and molecular signals that influence cell interactions[24].

Extending beyond cell-cell communication, gene regulatory networks infer the effect of ligand-receptor interactions on downstream signaling pathways and consequent gene expression[26–28]. As many of these methods are dependent on the quality of external datasets, especially tables of LR interactions, curated dataset updates are periodically published in manuscript supplements[9,23]. scRNAseq has helped formulate hypotheses of cell communication that drive biological processes such as organ and tissue development[15], homeostasis[22], and disease progression[11,20].

1.4 Spatial snapshots of cell-cell communication

Highly multiplexed imaging has expanded the ability to analyze communication across spatial length-scales. Resolving cell boundaries in dense tissue, classifying cell types, and assessing cellular functional states requires visualizing many molecular targets over the same region. New strategies overcome the limited multiplexing capability of traditional imaging modalities, and several are now commercialized.

One approach for multiplexed protein imaging is iterative cycles of fluorescent labeling, imaging, and bleaching or dissociating markers for multiple rounds. For example, cyclic immunofluorescence (CycIF) uses panels of standard, commercially available fluorescent antibodies to iteratively stain tissue over 8-20 cycles[29]. CODEX (Akoya Biosciences) stains tissue samples with a cocktail of DNA-conjugated antibodies followed by successive treatment with fluorescent nucleotide reporters[30]. Imaging mass cytometry is a non-cyclic imaging method that uses metal-conjugated antibodies followed by spatially resolved mass spectrometry to image over 40 different proteins simultaneously (Fluidigm)[31]. In addition to protein imaging, diverse protocols exist for imaging multiple RNA transcripts. Methods such as SLIDE-seq (Broad Institute)[32], Spatial Transcriptomics (10x Genomics)[33], and fluorescence in situ sequencing (FISSEQ; 10x Genomics)[34] analyze RNA transcripts mapped to specific spatial coordinates in tissue by sequencing, while other methods such as STARMap[35] and SABER-FISH[36] achieve subcellular resolution by imaging select, targeted RNA transcripts.

To date, most methods to examine spatial communication measure enriched interactions between different neighboring cell types. Computational methods scan

tissue images at multiple scales and search for "neighborhoods," or regions within the tissue of similar cell composition, thereby revealing enriched clusters of co-localized cell-types[29,30,37,38]. One approach identified spatial segregation of TAMs, activated macrophages (aMacs), dendritic cells (DCs), and others in a mouse colorectal cancer allograft model (**Figure 1-3, bottom left**). TAMs enriched in the tumor core compared to the lymphocyte-rich periphery. Cell adhesion, for instance via cadherins, promotes spatial segregation[38]. In another example, spatial analysis of ovarian cancer biopsies found that patients responding to combined PARP and PD1 inhibition displayed more co-localized clusters of PD-L1+ macrophages, hypofunctional CD8+ T cells, and tumor cells compared to non-responding patients[39].
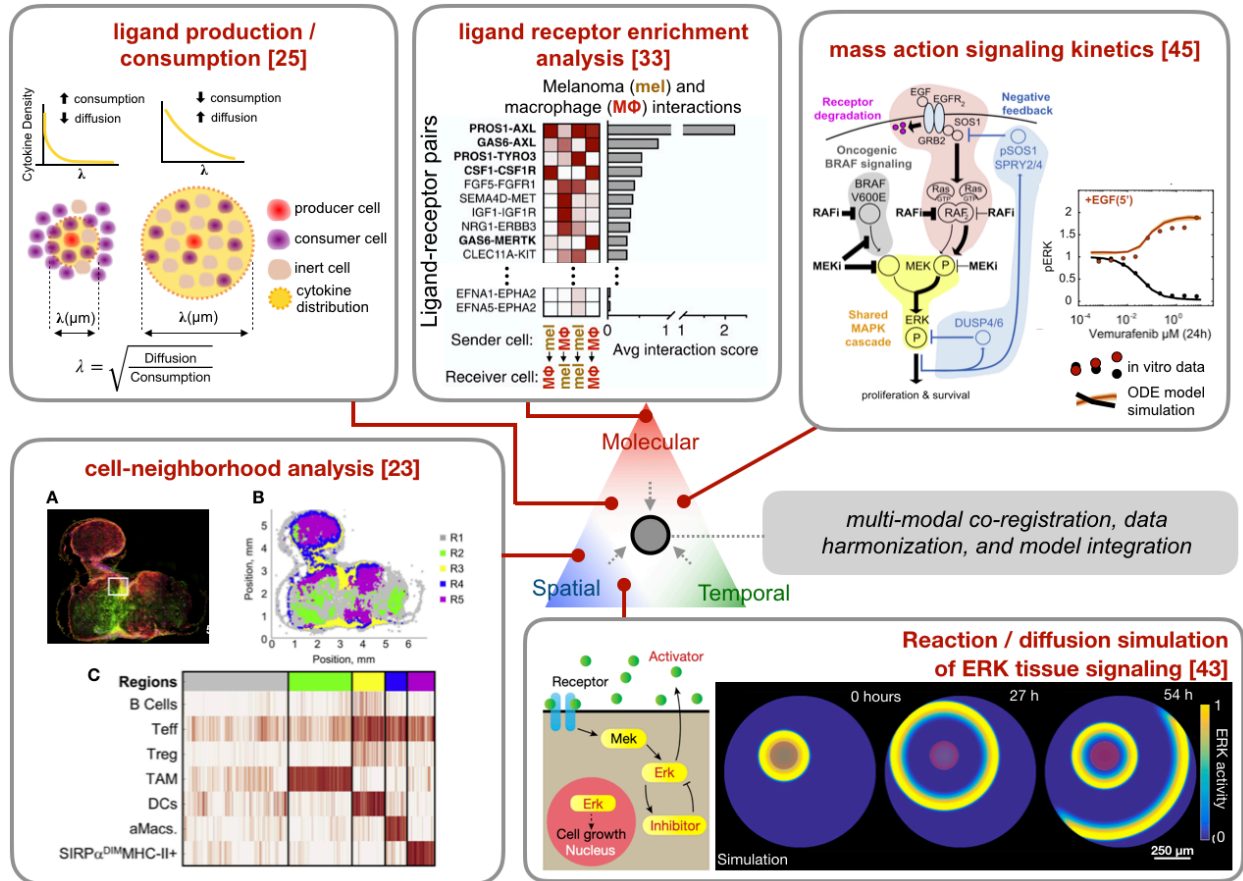
Figure 3: Quantitative modeling of cell-cell communication. *Top Left:* Computational modeling of cytokine concentration over characteristic length scales (**λ**), governed by rates of diffusion and consumption from cytokine producing and consuming cells[Oyler-Yaniv et al., 2017, Immunity, 46, 609-620]. *Top Middle:* scRNAseq ligand / receptor scoring from melanoma biopsies ranks tumor-macrophage signaling pathways by co-expression. Adapted from [Wang et al., 2020, Sci Adv, 6, eaaz8521]. *Top right:* Coupled ordinary differential equations model the kinetics of ligand-mediated signal transduction in melanoma cells and their response to BRAF inhibition. Adapted from [Gerosa et al., 2020, Cell Syst, 11, 478-494.e9]. *Bottom left*: (A) Neighborhood analysis of multiplex image mass cytometry data from syngeneic mouse tumors. Clustering highlights (B) different tissue regions, each with a (C) distinct cell composition. Adapted from [Stoltzfus et al., 2020, Cell Rep, 31, 107523]. *Bottom right*: Partial differential equation model of ligand-mediated ERK signaling in regenerating osteoblasts. Model

simulations generated periodic activity waves seen *in vivo*. Adapted from [De Simone et al., 2021, Nature].

Intercellular communication can also be modeled on a smaller scale by studying direct cell-cell contact and visualized using data structures such as graphs and adjacency matrices[24,30]. Open-source software tools such as histoCAT[37](analysis of neighbors and cellular interaction networks), Facetto[40] (visual analytics platform), and CytoMap[38](cell patterning, region networks, spatial correlations, etc.) have streamlined many of computational analyses for multiplexed imaging. Cell localization with a tissue is heavily regulated by intracellular gene regulatory programs and communication networks. By inferring gene expression gradients from from scRNA-seq, the spatial origin of individual cells and relationships between cells can also be computationally reconstructed[41].

Multiplexed tissue imaging and spatial transcriptomics complement scRNAseq in quantifying LR communication while also supporting spatial analysis. For instance, Mehta et al. used t-CycIF (**Figure 1-2B, top left**) to assess TAM polarization in biopsies of patients with triple negative breast cancer, focusing on CD68, CD163, and the immunosuppressive ligand PDL1, which canonically binds the immune checkpoint PD1 in juxtacrine. Elevated CD163+ PDL1+ TAMs and PD1+ T-cells in *BRCA1*-mutant tumors suggested TAM-mediated immunosuppression and motivated testing of a TAM-targeted anti-CSF1R therapy[10].

1.5 Complexity beyond cell-cell contact

It remains especially challenging to systematically parse how spatial organization impacts soluble ligands. In one study, the spatial range over which soluble ligands operate was approximated as a function of ligand production, effective diffusion, and cellular consumption rates[42] (**Figure 1-3, top left**). By comparing locations of IL2-producing CD4+ T-cells with pSTAT5 signaling in IL2-consuming regulatory T-cells in mice, soluble IL2 was modeled to exhibit gradients over 30-100 μm. In application to cancer, two recent studies combined scRNAseq with *in vivo* confocal (intravital) microscopy to find sustained, local IFNγ production from CD8+ T-cells could propagate >800 μm and elicit bystander effects[43,44]. This evidence adds context to studies examining IFNγ and IL12 communication in response to anti-PDL1 treatment[45] and CAR-T cell therapy[46,47]. Convection, extracellular matrix and decoy receptor binding, and cell migration are factors for future studies of other soluble ligands to weigh.

Additional factors beyond mere cell-cell contact can influence juxtacrine LR interactions. Extracellular forms of PDL1 have been demonstrated to modulate the PDL1-PD1 interaction, including via PDL1 anchored on secreted extracellular vesicles (EVs). The 30-150 nm exosome subset of EVs have been especially implicated and can be monitored in the blood of patients receiving PD1-targeted therapy[48]. In addition to modulating LR communication, EVs can transport mRNAs and intracellular proteins. In one study, the transport and action of EVs in tissue were studied by combining intravital microscopy with a Cre-LoxP system that reported on EV-uptake in individual cells. Malignant tumor cells produced EVs carrying pro-metastatic mRNAs to distant, less aggressive tumor populations **(Figure 1-2B, bottom left)**[12]. Communication mediated

by vesicles, cell debris, and albumin- or lipid-complexed components is also important for leukocytes exhibiting macropinocytosis, phagocytosis, and expressing high levels of relevant receptors. For example, subcapsular macrophages can capture tumor-derived EVs in the draining lymph node, thereby containing EV dissemination and modulating humoral immunity[49].

Cell communication mediated by vesicles, including apoptotic bodies, is implicated in sensing cellular turnover and death. Wang et al. systematically examined LR communication between tumor cells and TAMs, since TAM recruitment correlated with drug resistance in a melanoma cohort[11]. scRNAseq from patient biopsies indicated communication between tumor cells and macrophages via the TYRO3, AXL, and MERTK family of receptors: receptors and their ligands GAS6 or PROS1 were expressed at high levels in both cell-types (**Figure 1-3, top center**)[11]. These receptors are associated with drug resistance in tumor cells, immunosuppressive efferocytosis in macrophages, and their ligands bind externalized phosphatidylserine on apoptotic debris to promote receptor clustering[50]. Thus, their signaling may be amplified by tumor-targeted therapy, such as demonstrated with BRAF inhibition in melanoma[11]. In another example, RNA-seq analysis of purified cell populations from mice identified GAS6-AXL communication from dermal papillae to hair follicle stem cells as important in maintaining hair growth, and GAS6 expression was inhibited by both corticosterone and BMP as endocrine (systemic) and niche (local) cues, respectively[51]. These examples highlight how RNA-sequencing can identify putative LR pathways for mechanistic studies.

1.6 Interrogating cell dynamics by intravital imaging

While static measurements show how tissue communication is structured, spatiotemporal dynamics and perturbations better capture how such structures operate, particularly on a post-translational level. Given the limited multiplexing of intravital imaging (typically ~four fluorescence channels) compared to *ex vivo* methods, analysis usually focuses on key signaling components including FAK[52], mTORC1[53], and ERK1/2[54,55] as well as strategies to optically perturb them in vivo[56]. Recent examples in tissue have used intravital microscopy to monitor waves of Ca^{2+} signaling in the mouse mammary gland that travel through gap junctions in neighboring cells[13]. Here, Stevenson et al. imaged calcium-driven contraction of ducts and alveoli following stimulation with the hormone oxytocin (**Figure 1-2, bottom right**).

Multiplexed imaging of *in vivo* signaling dynamics was used in the example from Wang et al. described above. Intravital microscopy examined how putative LR interactions, including via AXL and MERTK, impacted downstream kinase signaling dynamics in tumor cells near (<40 µm) TAMs (**Figure 1-2B, top right**)[11]. Kinase translocation genetic reporters[57] recorded how ERK and JNK kinase pathways responded to therapeutic MEK1/2 inhibition, revealing local pro-resistance bypass signaling TAM-proximal cells[11].

In vivo imaging can guide quantitative modeling of interstitial ligand transport and target binding. For instance, rhythmic waves of single-cell ERK activity have been observed to travel radially outward in regenerating zebrafish scales to control tissue growth[58]. Spatial wave propagation was modeled by diffusion of soluble ligand reacting with intracellular positive and negative feedbacks (**Figure 1-3, bottom right**). Dynamic

ERK activity has also been observed in mouse blastocysts[59] and human xenograft tumors in mice[60]. In the latter example, pulsatile ERK activity was found in drug-adapted melanoma cells, and neighboring cells shared pulsing via autocrine/paracrine communication. Mass action kinetic models explained intracellular dynamics and related them to intravital observations (**Figure 1-3, top right**)[60]. Future modeling may incorporate spatial information via multi-compartment or finite element strategies, similar to as done for pharmacology[61,62].

1.7 Role of intercellular communication on cellular dynamics

Even though cellular dynamics in the form of cell migration and proliferation have been studied since the advent of the microscope, recent advancements in intravital confocal microscopy have enabled the exploration of additional dynamic readouts. Examples include calcium signaling and the activity of downstream signaling pathways such as ERK as described in the previous section.

Despite success in measuring new types of dynamics in tissue, there remain several unmet challenges. First, due to the ability to measure a small number of molecular markers simultaneously, it is difficult to understand how interactions with other cell types affect these dynamic readouts. Second, the dynamic readouts themselves are limited and cannot capture sub-cellular changes which often precede cell-wide changes. Third, computational methods to analyze dynamic readouts require improvements to gain a better insight into various contributing extracellular and intracellular factors.

In this thesis, I address the challenges above by studying the role of tumor-associated macrophages on cancer cell dynamics at varying scales ranging from sub-cellular cytoskeletal changes to alterations in cell migration and morphology. In the context of cancer, communication with several cell types including dendritic cells, t-cells, fibroblasts, and other key components have been shown to play an important role in disease progression, and some elements can be reprogrammed to target cancer. Highlighted by the examples in the above sections, tumor-associated macrophages also play a vital role in these interactions by secreting several pro-inflammatory and anti-inflammatory cytokines that can have variable effects on disease progression.

I hope the analyses presented in this thesis paves the way for a more systematic and quantitative evaluation of how local environments affect cellular behavior, especially in the field of cancer, where our understanding of the tumor microenvironment has only scratched the surface.

1.8 Overview

In this thesis, I aim to develop single-cell computational and experimental approaches to decipher how tumor-associated macrophages affect cancer cell microtubule dynamics and other high-level dynamic phenotypes including cell migration and disease progression.

In chapter 2, I detail a novel computational and imaging pipeline to visualize and quantitatively analyze microtubules dynamics *in vivo*. Intravital imaging in combination with plus-end tip tracking enables capturing of microtubules dynamics in live xenograft tumor models. *In vivo* microtubules behavior was compared to MT behavior observed in 2D *in vitro* cultures, and 3D collagen gel cultures.

In chapter 3, I apply the detailed method presented in chapter 2 to understand how an important component of the TME, tumor-associated macrophages, affects MT dynamics. Furthermore, I describe how such dynamics also correlate cancer with cell morphology and cancer cell dynamics. Lastly, I perform a series of experiments to gain a mechanistic understanding of the phenomenon observed.

In chapter 4, I present a more generalized method to study dynamic biological processes, including cancer, from scRNA-seq datasets. Rather than focusing on sub-cellular dynamics as in chapters 2 and 3, I aim to understand how intercellular communication changes and drives biological processes such as cancer progression.

Finally, in chapter 5, I discuss exciting new steps that can improve our understanding of how intercellular communication contributes to fundamental biological processes and disease progression.

Chapter 2 Developing and applying a framework to quantify microtubules dynamics of tumor cells in vivo.

Abstract

As a core cytoskeleton component, microtubules (MTs) mediate mitosis, directional signaling, and are therapeutic targets in cancer. *In vitro* studies have shown that microenvironmental biological and mechanical cues regulate MT dynamics, yet it has been a challenge to measure actual MT behavior of cancer cells *in vivo*. Here we used a newly developed imaging pipeline, based on computational plus-end tip tracking and *in vivo* confocal fluorescent (intravital) microscopy, to quantify the structure and dynamics of cancer cell MTs in a live xenograft mouse model. Despite finding no substantial differences in features including the speed of individual MTs *in vivo* compared with 2D *in vitro* cultures, cancer cells *in vivo* displayed more consistent alignment of MT growth along the major length axis of their respective cell bodies. This *in vivo* phenotype was only partially recovered when cells were cultured in 3D collagen gels as opposed to on tissue culture plastic.

2.1 Introduction

To study sub-cellular dynamic cell phenotypes, this chapter describes work on capturing intracellular microtubule dynamics *in vivo.* Microtubules are excellent candidates for studying cellular dynamics because they are dynamic in nature undergoing polymerization and depolymerization. Furthermore, they are involved in numerous cellular processes including migration, vesicular transport, cellular asymmetry, and cell division. Therefore, capturing this dynamic phenotype and understanding of how these important structures are changing provides a picture of a particular cells machinery.

Microtubules are one of three major of components the cell cytoskeleton. The cytoskeleton is a dynamic network of polymeric filaments and regulatory proteins that coordinate cellular morphology, mitosis, and migration. It consists most prominently of actin filaments (F-actin) and microtubules (MTs), which are co-regulated through the small GTPases of the Rho family including Rac1 and Cdc42[63,64]. Both F-actin and MT structures are maintained through a balance of near constant polymerization and depolymerization[65]. While F-actin organizes into highly branched networks conducive to force generation, MTs are often longer (>50 μm in some cases), straighter, and turn over more slowly (every 3-5 min)[66]. F-actin governs rapid cycles of local cytoskeletal protrusion, adhesion, and contraction that are responsible for physical cellular propulsion. However, MTs control these cycles by establishing and stabilizing cell polarization through the directional trafficking of molecules and vesicles. In fact, MT-controlled molecular asymmetry between the front and rear end of a migrating cell— and the correspondingly selective allocation of cell migration machinery including focal

adhesion proteins, proteases, and secretory vesicles — is critical for cellular migration[67–69].

Persistent cellular migration is central to development, wound-healing, and immune responses. Moreover, directional migration of cancer cells drives metastatic invasion and dissemination, which is responsible for 90% of cancer death[70]. Decades of effort have gone into understanding how MTs and their dynamics are regulated in the context of metastatic solid tumors. However, the majority of these studies have been conducted using monocultures of cells growing on 2D tissue culture substrates[71,72], which do not reflect the complex biological and mechanical environments that cancer cells encounter *in vivo*. MTs are typically more important for cell shape and migration in three-dimensional cultures than in 2D on stiff substrates, and 3D culture is more representative of the mechanical and adhesion environments found *in vivo*. For example, actin-rich lamellae, which are characteristic of migrating cells on stiff 2D substrates, can be supplanted by long MT-regulated protrusions or pseudopods when cells are in soft 3D extracellular matrix (ECM)[73,74]. Furthermore, the migration characteristics of cancer cells, such as speed, persistence, and rate of protrusion formation, can be distinctively regulated in 2D vs. 3D cultures[75–77]. Treatment of cancer cells with both MT stabilizing (e.g., paclitaxel) and destabilizing (e.g., nocodazole) drugs results in loss of protrusions required for migration in 3D collagen gels. However, in stiff 2D cultures, these drugs can have minimal impact of cellular migration[78–80]. Similar results have also been observed in mesenchymal cells such as fibroblasts and endothelial cells[74]. Despite improvements in 3D culture systems, the complexity of *in vivo* tumor microenvironments may not ever be fully reproduced, thus begging the

question: if MT dynamics and cell migration occur so distinctly in various tissue culture models, how do MTs actually behave *in vivo*? Traditionally, it has been difficult to directly measure individual MTs *in situ* and in real-time using live animal models of disease or normal tissues.

To address these issues, we developed an integrated computational and imaging pipeline that combines *in vivo* confocal (intravital) microscopy[81], automated plus-end tip tracking of individual MTs[82], and multivariate statistical analysis to study MT dynamics in live xenograft models of cancer. We analyzed MTs in a quantitative and spatially-unbiased manner using the MT end binding protein, EB3, fused with a fluorescent protein. Automated detection of fluorescent EB3 from *in vivo* time-lapse microscopy images supported quantitation of MT growth rates and over a dozen other intrinsic MT track features at high accuracy for thousands of tracks across populations of individual cells. This approach revealed that *in vivo*, MT growth in cancer cells was especially aligned along the cell major axis and coherently with each other in the same cell, compared to the same cells grown *in vitro* on 2D tissue culture plastic or in 3D collagen gels. Coherent MT dynamics *in vivo* correlated with elongated cell morphology, formation of MT-rich pseudopod like structures and cell migration. Overall, here we present a platform for quantitatively examining the *in situ* dynamics of MTs in live xenograft models of cancer, revealing microenvironment-dependent behaviors critical to multicellular organization, cell-cell communication, and disease processes.

2.2 Results

2.2.1 Experimental setup for imaging, detecting, and tracking in vivo EB3-mApple comets.

To visualize plus-end MT dynamics in cancer cells, we generated stable transfectants of the fusion protein EB3-mApple, using mApple as a photostability-optimized variant of mOrange[83] that was previously found to be ideal for intravital microscopy (IVM) [81]. Fluorescent fusion proteins of EB3, also known as MT associated protein RP/EB family member 3 (MAPRE3), are widely used as tools to visualize MT dynamics in live cells[84]. They are relatively non-perturbing of endogenous dynamics, and can faithfully report on the activity of MT-targeting drugs in cancer cells [85,86]. As a model system, we used HT1080 human fibrosarcoma cells, since they have been extensively characterized by IVM and in the literature for their migratory and invasive behavior, responsiveness to MT-targeting therapies, and distinct cytoskeletal characteristics in 2D vs. 3D tissue culture environments[85–91]. Xenografts of HT1080-EB3-mApple cells were generated via subcutaneous injection, and dorsal window chambers were surgically implanted over tumors to enable stable and longitudinal imaging at subcellular resolution. To aid in distinguishing cells from each other *in vivo*, only a fraction of tumor cells expressed EB3-mApple. Upon formation of vascularized tumors at roughly 2 weeks post-inoculation, IVM was performed by anesthetizing subjects on a heated stage and immobilizing the window chamber for stable time-lapse imaging.

In this model, IVM revealed comet-like EB3-mApple behaviors that were consistent with previous EB3-based studies of MT dynamics[82,84]. Automated

computational analysis accurately detected and linked comet-like structures to form time-lapse trajectories of individual MTs. We used the linking algorithm plusTipTracker to identify nearby comets in consecutive frames with similar properties, which also accommodated for transitory gaps between track segments arising from variable signal-to-noise, focus, and EB3-binding (**Figure B-1**). We manually examined the accuracy of 200 computationally derived tracks from tumor cells either in 2D culture or *in vivo*, and found a false positive rate of <5% **(Figure B-2)**. Time-lapse images show track distributions throughout each cell. Therefore, employing this computational tracking pipeline allowed us to quantify a large number of tracks under various stimuli in a spatially and temporally unbiased manner.
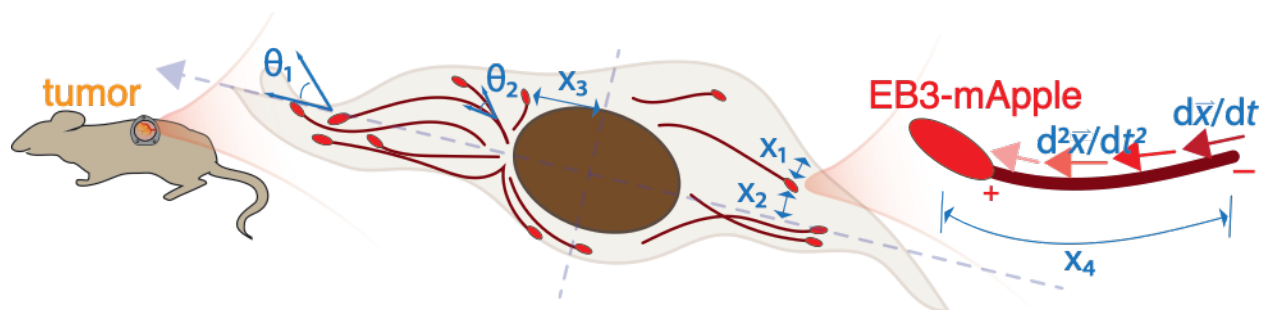
Figure 2-1. *In vivo* MT imaging and analysis. MT features (blue) and others were quantified from IVM of EB3-mApple comet trajectories (red).

In our pipeline, we computed 14 unique track features to measure MT behavior and dynamics, including MT growth speed (average, minimum, maximum, and standard deviation), cellular location (distance to nearest cell edge, major axis, and minor axis, shown as x_1, x_2, and x_3 respectively in **Figure 2-1**), orientation (θ_1 in **Figure 2-1**), persistence, curvature, displacement, and path length (x_4 in **Figure 2-1**). We also

computed track coherence, a measure of how similar a track's direction is to other tracks (related to θ_2, **Figure 2-1**), at both local (within a 20 μm radius) and whole-cell levels. For instance, a cellular coherence value of 1.0 means all MT tracks move in the same direction and suggests asymmetric polarization, while symmetrically radiating MT tracks from the cell center would have a cellular coherence of 0.0. Because EB3 binds to only growing MT ends, we did not capture MT shrinkage and pausing[92]. All features were normalized to be independent of cell size.

To gauge the impact of EB3-mApple itself on observed MT dynamics, we measured cell-by-cell correlations with EB3-mApple expression, finding no significance for the majority of track features (12/14). As exceptions, displacement and path length somewhat correlated ($R^2 < 0.25$), explainable by the technical ability to image brighter MT tracks over longer time periods, and no correlation was found after correcting for track duration (**Figure B-3)**. Genomic alterations of *MAPRE3* (encoding EB3) and its expression by RNA-seq did not correlate with overall survival outcomes of cancer patients across The Cancer Genome Atlas (TCGA; **Figure 2-2**), suggesting that EB3 itself is not a major driver of disease progression. These analyses thus support the use of EB3 as a relatively non-perturbative tool for MT imaging.
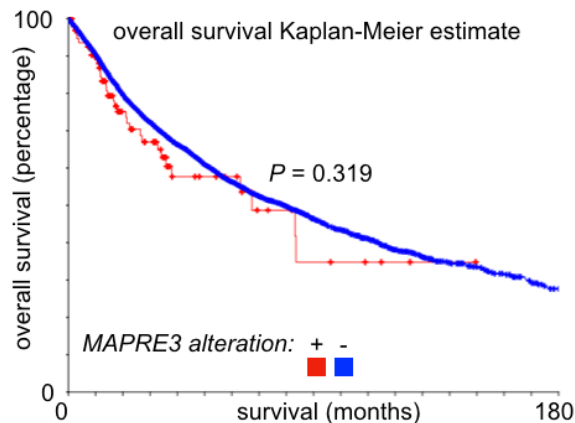
MAPRE3 alteration status	Total Cases	Deceased Cases	Median Survival
+	99	34	67 mo.
-	10703	3480	79 mo.

Figure 2-2. Kaplan-Meier analysis of overall survival across The Cancer Genome Atlas (TCGA) as a function of EB3 alteration (copy number amplification and mutation; P-value was calculating using using a two-sided log-rank test; cBioPortal.org).

2.2.2 Systematic profiling of MT dynamics identifies enhanced coherence among cells growing *in vivo* compared to *in vitro*.

We quantified MT differences between cells growing *in vivo* compared to *in vitro* by performing matched analysis of the same HT1080 EB3-mApple cell line cultured on standard 2D tissue culture plastic (**Figure 2-3**). We also examined the ES2 human ovarian cancer (OVCA) cell line as a second model (**Figure 2-3, B-5, B-6**). In HT1080, the average MT growth rate of *in vitro* tracks (0.35 µm s^{-1} ± 0.15 µm s^{-1} s.d.) and *in vivo* tracks (0.38 µm s^{-1} ± 0.18 µm s^{-1} s.d.) were relatively consistent with prior studies in other cell types *in vitro* (pig kidney LLC-PK1 cells: 0.30±0.13 µm s^{-1}, chinese hamster ovary CHO cells: 0.27±0.11 µm s^{-1}, and human keratinocyte HaCaT cells: 0.31±0.12 µm s^{-1})[82,93]. There was no consistent difference in relative intracellular location of pre-filtered MT tracks in HT1080: distances from the cell edge, major axis, and minor axis

revealed that the majority of MTs were closer to the cell center both *in vivo* and *in vitro*. However, in ES2, *in vivo* tracks were somewhat faster and further from the cell edge (**Figure 2-B**). These observations are consistent with known MT origination from microtubule organizing centers adjacent to the cell nucleus, and less stable and slower moving MTs at the cell periphery[94].

A *in vivo*

HT1080-EB3-mApple   MT tracking   merge

B *in vitro*

HT1080-EB3-mApple   MT tracking   merge

C

higher in vitro ← → *higher in vivo*

MT Feature		
cellular coherence (θ_2)		* $P=0.001$
orientation (θ_1)		* $P=0.007$
path length (x_4)		
displacement		
max speed		
speed SD		
average speed		
curvature		
min speed		
distance to edge (x_1)		
dist. to minor axis (x_3)		
dist. to major axis (x_2)		
local coherence (θ_2)		
persistence		

HT1080
ES2

-0.4   -0.2   0.0   0.2   0.4   0.6

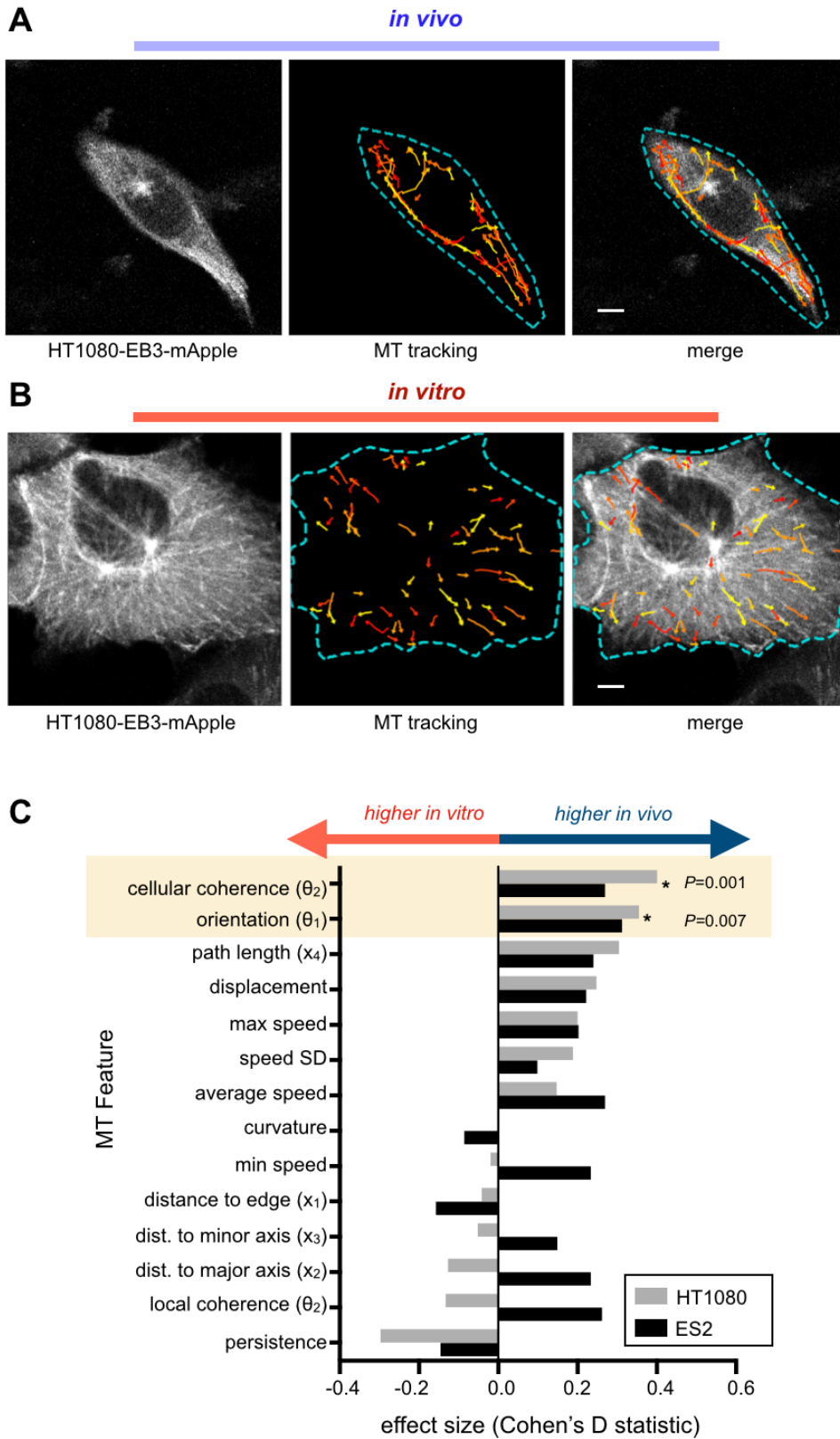effect size (Cohen's D statistic)

Figure 2-3. (*Continues on next page*).
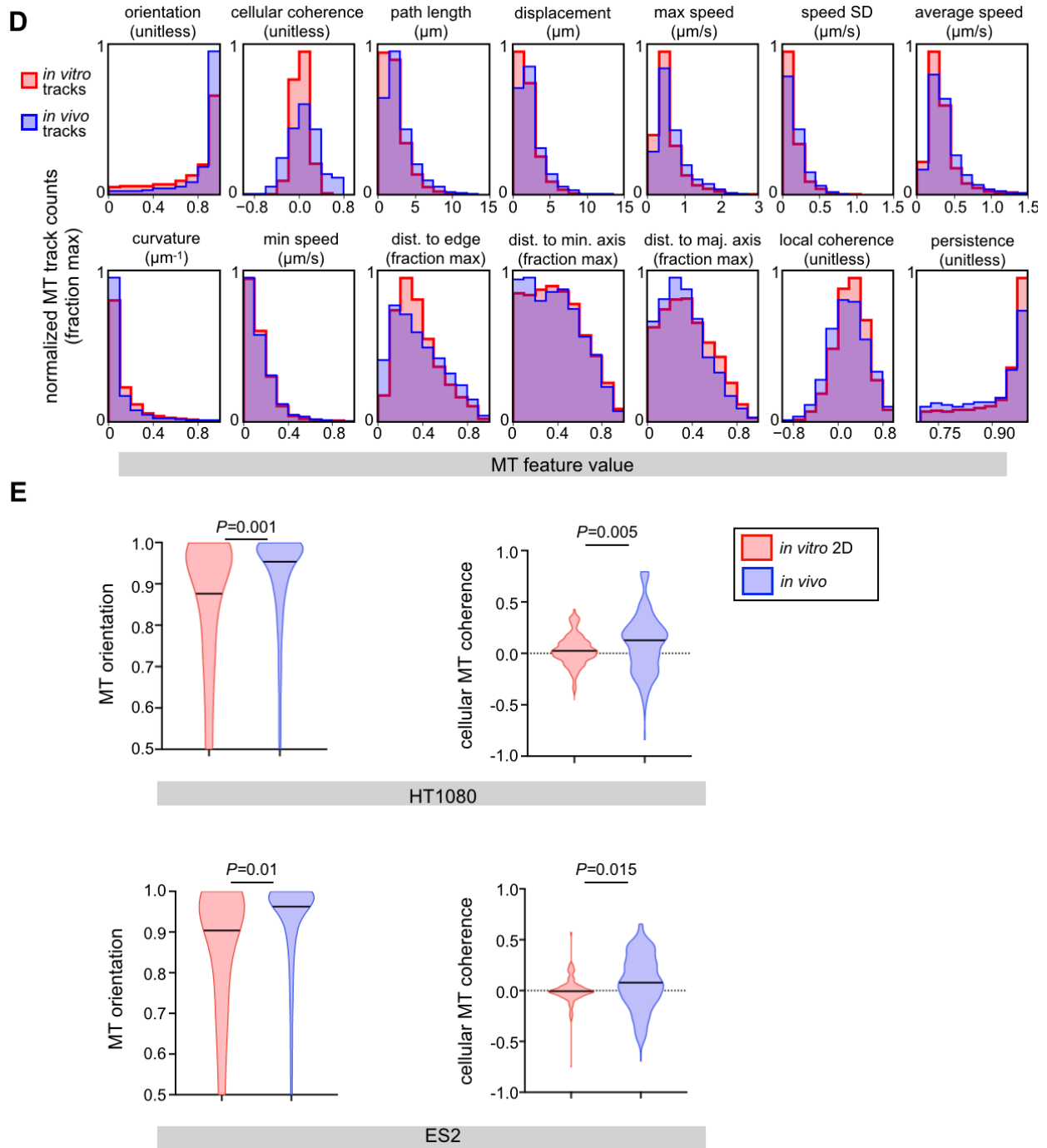
Figure 2-3 Cont.

D

E

Figure 2-3. Microtubule dynamics in live xenograft tumor models. (A) Representative time-lapse IVM of cancer cells growing in a dorsal window chamber from nu/nu host (left). MTs were tracked (center) and randomly pseudo-colored for visualization. (B) Representative in vitro time-

lapse images were obtained from 2D culture using the same imaging system (left) and tracking

software (center). (C-D) For each MT track, the (C) effect size was compared between in vivo

and in vitro conditions along with (D) the corresponding distribution plot for HT1080 MT tracks

(C: *two-tailed permutation test with Benjamini-Hochberg correction). (E) Distributions of MT

features showing in vivo vs. in vitro differences shared for both HT1080 and ES2 xenograft

models, using the same IVM setups (*two-tailed permutation test; bar denotes median). For

HT1080, a total of n=8,126 tracks across 73 cells and 4 tumors were analyzed (A-E). For ES2 a

total of n=2,857 tracks across 42 cells and 5 tumors were analyzed (C,E). Scale bar = 5µm

(B,C).

Compared to all other features, the orientation and coherence of MT tracks

showed the greatest consistent increase for cells grown *in vivo* vs. *in vitro.* Orientation

was computed from the angle between the directional vector of the MT track, and the

directional vector of the corresponding cell major axis (**Figure 2-1**, θ_1). A cosine

transformation caused tracks parallel to the cell major axis to have high orientation.

Nearly twice as many HT1080 MT tracks were angled off of the cell's major axis by >45°

(orientation <0.71) *in vitro* compared to *in vivo* (32.6% +/- 0.60% vs. 16.7% +/- 0.79%

s.e.m., respectively), meaning MT tracks were more aligned with the cell's major axis

when cells were grown *in vivo*. As a related measurement, the MT coherence quantified

how similarly a MT track was oriented to nearby tracks within a specified distance. A

positive coherence value indicated that the track was traveling parallel to nearby tracks,

while a large negative value indicated that the track was traveling antiparallel.

Coherence was measured for each track at the local (within 20 µm from the track) and

cellular level (across all tracks of a cell). Locally, *in vivo* and *in vitro* MT tracks displayed

comparable levels of MT coherence. However, when analyzing all tracks across the whole cell, MT tracks were more aligned and coherent *in vivo*. *In vivo* HT1080 MT tracks exhibited a 3.2-fold increase in mean cellular coherence compared to tracks from cells growing *in vitro* (0.10 ± 0.006 vs. 0.03 ± 0.002 s.e.m., respectively). Cells were on average more elongated *in vivo,* which can impact MT behaviors. However, even when comparing similarly-shaped *in vivo* vs. *in vitro* cells, MT orientation and coherence were still enhanced *in vivo* (**Table 2-1**).

two-way ANOVA table (*P*-values)

Dependent Variable:	MT coherence	MT orientation	MT coherence	MT orientation
Independent variable: *in vivo* vs *in vitro*	0.014	0.036	0.004	0.006
Independent variable: Cell shape	0.72	0.057	0.63	0.035
	cell circularity		cell eccentricity	

Table 2-1. Measuring MT dynamics independent of cell shape. Statistical significance between conditions (row interactions) and cell shape (column interactions) were calculated using a two way ANOVA (n=69 cells). ANOVA interaction terms between the independent variables were not significant.

Differences between in vivo vs. in vitro conditions are a function of biological changes and technical biases. In subsequent imaging, we focused on the former and minimized the latter through comparisons across matched conditions. We tested (a) whether image quality could impact conclusions by creating artificially noisy images

(Figure 2-4), (b) if tracking parameters were sensitive to image differences by recomputing statistics on different parameter combinations (**Figure B-7**), and (c) whether individual cells were driving differences by permuting cell labels to compute significance (**Figure B-8**). (d) Excluded cells capturing <80% of a cell body within the field of view were also excluded from the main analyses, and we further evaluated if their inclusion altered results (**Figure B-7**). Overall, cells consistently exhibited greater MT alignment in vivo compared to 2D tissue culture plastic, in a manner robust to cell-to-cell batch effects, variation in image quality, and variation in tracking parameters.
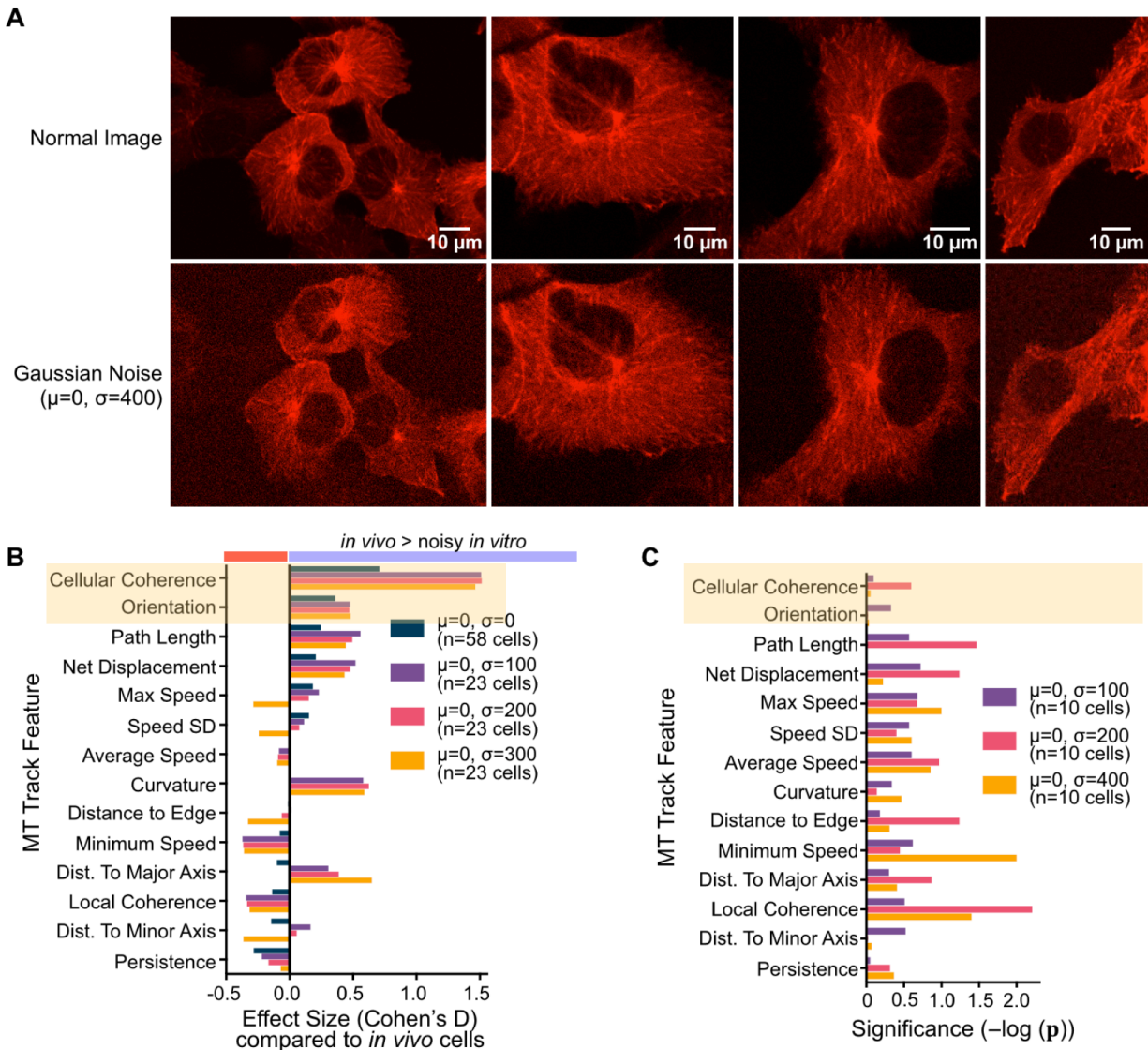
Figure 2-4. The effect of artificial image noise on MT track statistics.

(A) Various levels of gaussian noise (μ=0, σ=100, 200, and 400 pixels) were added to images of

HT1080 EB3-mApple cells grown in 2D culture. (B) The effect size between MT tracks from

noisy *in vitro* images shown in A and HT1080 EB3-mApple *in vivo* images was measured using

Cohen's D statistic (n=23 cells). These data show that relatively greater MT cellular coherence

and orientation seen *in vivo* are robust to added noise in the *in vitro* images. (C) 14 MT track

features were statistically compared between noisy *in vitro* images and the original, clean (μ=0,

σ=0) *in vitro* images (2-tailed permutation test, n=10 cells), again suggesting that MT cellular coherence and orientation observations are robust to added noise in the imaging.

2.2.3 3D collagen gel cell cultures display distinct MT dynamics

MT dynamics can differ in cells growing in 3D hydrogel materials rather than on stiff 2D surfaces. We thus examined if the MT dynamics of HT1080 tumor cells observed *in vivo* could be recapitulated in soft 3D cultures. HT1080-EB3-mApple cells were grown in 3D collagen I hydrogel, since collagen I is a major TME structural component[33] shown to influence cell migration and metastasis[87,95]. We used the same imaging pipeline to track MTs within the 3D cultured cells (**Figures 2-5, 2-6, B-9, B-10, B-11**).
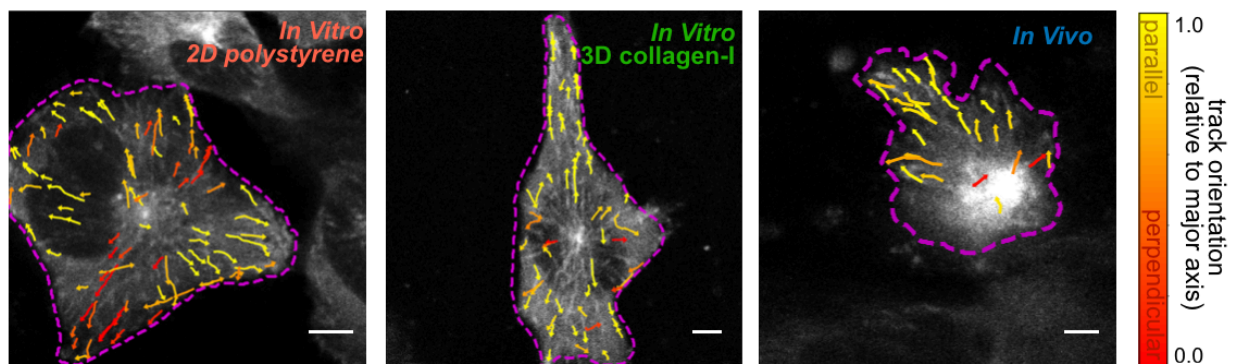
Figure 2-5. Representative confocal images of HT1080 EB3-mApple cells grown as indicated, with tracks pseudo-colored according to MT orientation along the major length axis of the cell (scale bar = 5μm; n=85 cells across n≥2 in vitro replicates and n=4 tumors).
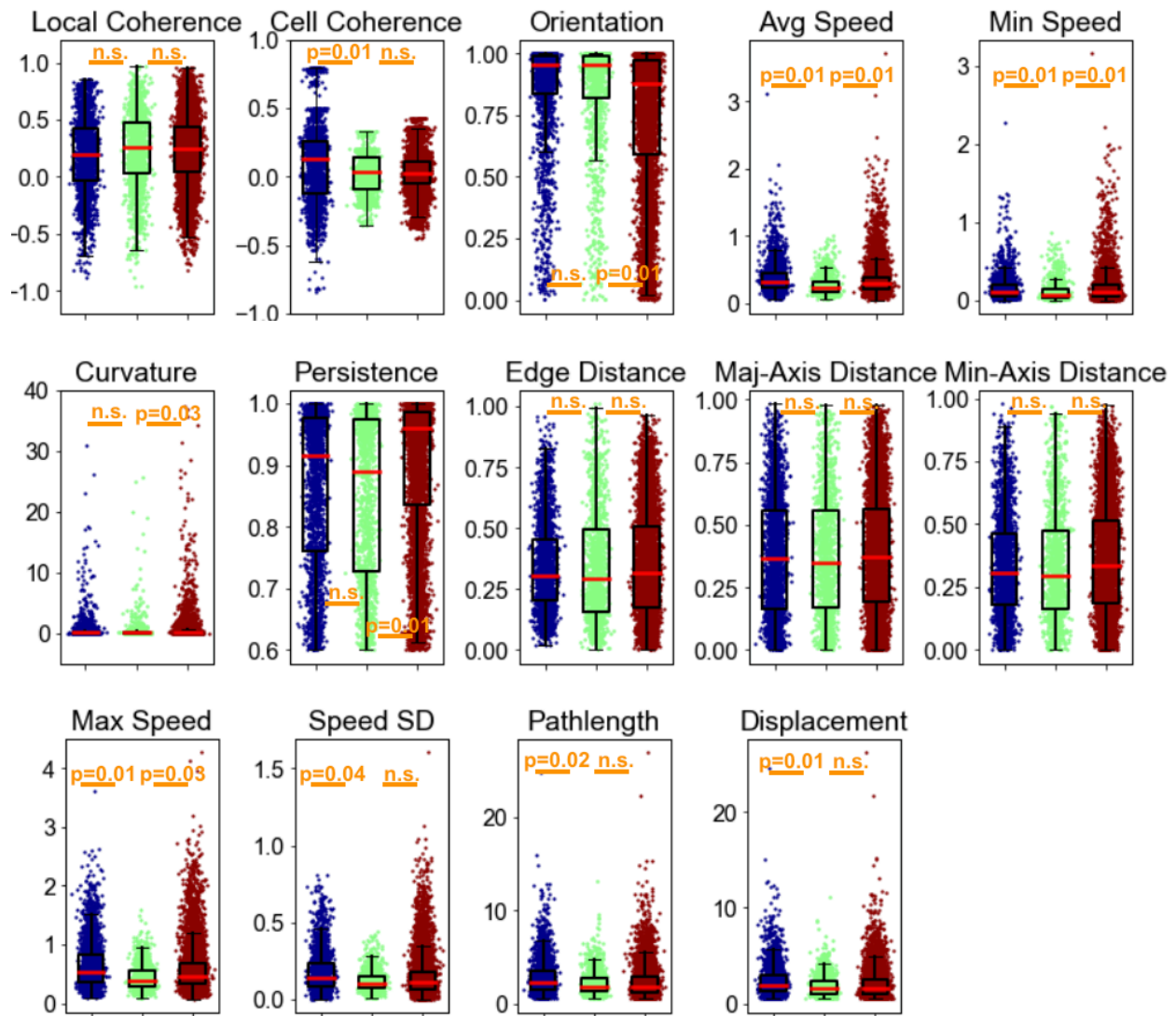
Figure 2-6 Individual track distributions of MT features.

Box plots show all MT tracks for each of the 14 track features. Each point corresponds to an individual MT track from an HT1080 EB3-mApple cell *in vitro* (red), *in vitro* 3D (green), or *in vivo* (blue) (total n=9,451 tracks; *two-tailed permutation test). The red line denotes the median of all MT tracks under the indicated condition.The red bar denotes the median of the cell medians (total n=85 cells). For all, box plot defined as Q1/25%tile, median, Q3/75%tile with outliers falling outside Q3/Q1±1.5*IQR.

We used principal components analysis (PCA) as a dimensionality reduction method to systematically compare how the pattern of co-correlated MT features changed under 2D and 3D culture conditions relative to *in vivo* phenotypes. The PCA scores and loadings plot indicates where experimental conditions (scores) and MT features (variable loadings) fall within the primary axes of covariation, the principal components (PCs; **Figure 2-6A**). 3D cultured cells behaved distinctly from cells grown *in vivo*, indicated by divergent PCA scores from the centrally positioned 2D culture (**Figure 2-7A**). Although MT orientation increased in 3D culture (**Figure 2-7B**), and therefore phenocopied *in vivo* dynamics, 5/14 features did not match *in vivo* behavior (**Figures 2-6, B-11**), including cellular MT coherence (**Figure 2-7B**). Thus, the *in vitro* 3D track distribution failed to fully mimic the *in vivo* phenotype.

We next examined whether increased *in vivo* MT coherence could be explained by more elongated *in vivo* cell shape. We again performed PCA, but using features of gross cytoskeletal shape as variables (**Figure 2-7C**). The first and second principal components (PC1, PC2) broadly captured cell elongation and cell size, respectively. Although more detailed and/or volumetric analysis could reveal higher-order distinctions, both *in vivo* and 3D-cultured cells exhibited a positive PC1 shift compared to 2D-cultured cells, characterized by decreasing cell circularity and increased elongation (**Figure 2-7D**). Thus distinct *in vivo* MT dynamics could not be entirely explained by differences in cell elongation.
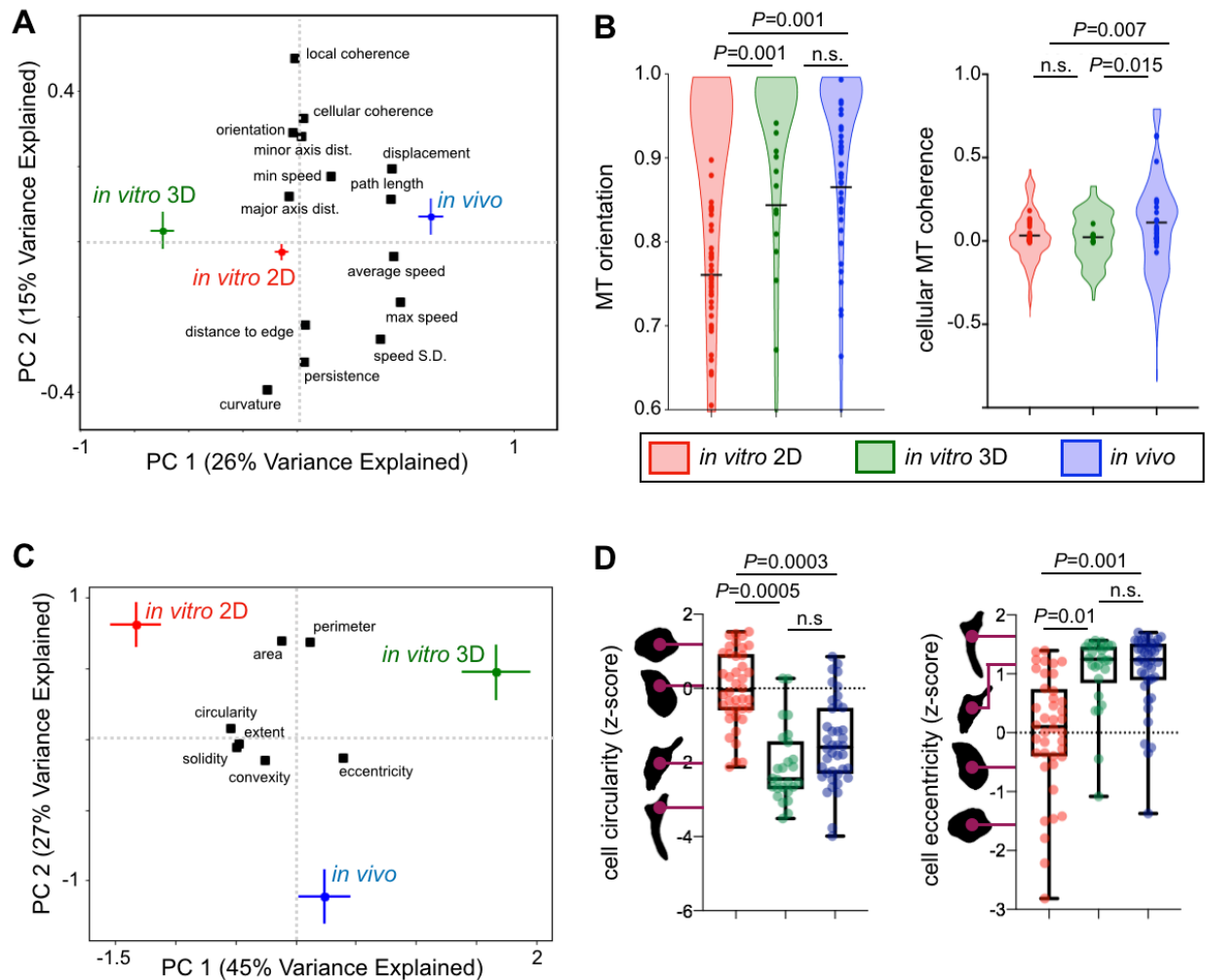
Figure 2-7. Coherent in vivo MT dynamics are not fully reproduced by 3D collagen in vitro cultures. (A) MT features were analyzed by principal components analysis (PCA), shown according to average condition score (± s.e.m.) and variable loadings (black squares; n=5794 tracks, middle 95% for all features). (B) Violin plots show single-track distributions for orientation and cellular coherence (bar denotes median, cell averages overlaid as individual data points; *two-tailed permutation test; n=9,448 total tracks from 85 cells). (C) PCA captures covariation between cellular shape features (loadings, black) across imaging conditions (scores ± s.e.m.; n=106 cells). (D) Single-cell distributions of shape features, matching C (*two-tailed t-test;

n=106 cells; box plot bars represent the minimum, 25%tile, median, 75%tile, and maximum

values). Source data are provided as a source data file.

2.3 Discussion

Here we use multichannel confocal IVM coupled with computational image analysis to directly monitor the behavior of MT dynamics in a live xenograft mouse model of cancer. As a core cytoskeletal component, MTs participate in diverse cellular processes and are tightly regulated in a spatially dynamic, coordinated, and quantitative rather than binary manner. Furthermore, the dynamics of individual MTs within and between cells is highly heterogeneous, as are the impacts of MT-targeting drugs operating through distinct mechanisms. Therefore, simply counting MT tracks or measuring individual features such as speed can fail to capture higher-level patterns in co-regulated MT behaviors. To address this issue, in this work we examined a wide spectrum of MT dynamic features across thousands of individual MTs, including speed and persistence in MT growth, and applied multivariate statistical methods to interpret patterns in MT behavior across experimental conditions. Our studies in multiple cancer cell models revealed that the cellular coherence and alignment of MT dynamics were among the most significantly altered properties that changed with microenvironmental context.

In this work, we correlated MT alignment with cellular elongation and migration as components of cancer metastasis, yet the importance of MT alignment broadly extends to other biological processes involving directional signaling, protein trafficking and cellular migration. For instance, aligned MTs coupled with the endoplasmic reticulum facilitate directional fluid flow of intracellular cytoplasmic contents [96]. Plus-end MT tip-tracking has repeatedly revealed MT coherence as important for directional cell migration. For example, MTs persistently grow at the cell leading edge, and

depolymerize at the trailing edge, during cellular elongation and directional migration in angiogenesis and wound healing[97]. In organismal development, coherent MT dynamics guide formation of the dorsal axis in Xenopus oocytes, as bundles of parallel MTs orient towards the dorsal end of cells prior to cortical rotation[98].

A majority of previous studies tracking MT end-binding proteins have relied primarily on *in vitro* models and non-mammalian model organisms. However, MT dynamics have more recently been examined in the central and peripheral nervous systems of mammals by imaging YFP-EB3 in mice, and key findings from this work examined MT orientation and anterograde directionality along the nuerite major axis [99]. Polarized MT dynamics are essential for the elongation of neurites to form axons or dendrites as well as neurite remodeling after injury or neurodegeneration [100,101]. Despite the increasing appreciation for aligned MT dynamics in orchestrating behaviors in tissue microenvironments, it has been difficult to directly study these behaviors in live animal models of cancer, and especially in a quantitative, systematic, and automated fashion. We anticipate that the imaging platform presented here, will lead to new directions in examining subcellular-scale signaling and regulatory processes, as well as MT-targeting drug action.

2.4 Material and Methods

2.4.1 Materials

HT1080 and ES2 cells were originally from ATCC, and were cultured according to provider guidelines using DMEM (for HT1080) or McCoy's 5a (ES2) medium, and 10% FBS (Atlanta Biologicals), 100 IU mL^{-1} penicillin,100 µg mL^{-1} streptomycin (Invitrogen), with incubation at 37℃ and 5% CO2. Cells were routinely evaluated for mycoplasma contamination. HT1080-mem-mApple, HT1080-EB3-mApple, ES2-EB3-mApple, and ES2-mClover cells were all generated by lentiviral transduction. The construct mApple-EB3-7 was a gift from Michael Davidson (Addgene plasmid # 54892), and mClover expression construct (pLentiCMV Puro DEST ERKKTRClover) was a gift from Markus Covert (Addgene plasmid # 59150; http://n2t.net/addgene:59150; RRID:Addgene_59150)[57]. Cell lines were tested for mycoplasma contamination using Lonza MycoAlert. Negative test results were obtained for cell lines used in the study.

2.4.2 Intravital microscopy

Confocal microscopy was performed using an Olympus FV1000 multiphoton imaging system. Animals were used in accordance with guidelines from the Institutional Subcommittee on Research Animal Care and under approval from the Institutional Animal Care and Use Committee (IACUC) at Massachusetts General Hospital. Animals were housed in a light-dark cycle, climate (temperature and humidity) controlled vivarium and kept under ad libitum food and water diet supplied by the MGH Center of Comparative Medicine staff. 2 million parental HT1080, HT1080-EB3-mApple, HT1080-memApple, and/or ES2-EB3-mApple cells were suspended in 50µl PBS, injected under

the fascia 30 min after surgical dorsal window chamber implantation, in female 4-8 week old nu/nu mice (Cox7, MGH), and imaged approximately 2 weeks later with visible tumor formation. Static and time series images were collected using a XLUMPLFLN 60x or 20x water immersion objective (NA 1.0; Olympus America) and up to 10x digital zoom. Images were scanned sequentially using 405-nm, 473-nm, 559-nm and 633-nm diode lasers in combination with a DM405/488/559/635-nm dichroic beam splitter. Emitted light was then separated and collected using appropriate combinations of beam splitters (SDM473, SDM560 and SDM 640) and emission filters BA430-455, BA490-540, BA575-620, and BA655-755 (all Olympus America). For EB3 imaging, to minimize photobleaching and potential artifact from translational drifting, we captured brief snapshots of MT dynamics for a given cell: movies were acquired for 40-130 sec in duration with a frame rate of between 0.8 to 2.7 seconds per frame, a relatively short dwell time (8 μs pixel^{-1}), low laser power (λ_{ex} 559 nm, 2% power), and at a single plane of focus.

2.4.3 Study Design

Sample sizes were determined by counting the number of MT tracks, cells, tumors, or mice depending on the analysis. For track based analyses sample sizes were not predetermined as all the tracks computationally determined were used for downstream analyses. Sample sizes for cells, tumors, or mice were chosen based on estimated effect sizes from prior studies with this xenograft model and *in vitro* cell culture experiments[11,85,86,89,91]. All experiments were performed with ≥ 3 independent replicates as described in the figure captions. Assignment of animals into treatment

groups, as with the IL10R or *in vivo* vs *in vitro* experiments, was performed randomly. For both *in vivo* and *in vitro* experiments, samples that underwent different treatments (Chapter 3 - drug treatment, co-culture conditions, MΦ polarization, etc.) were placed into different groups. For all MT track and shape experiments, results were obtained via unbiased computational scripts, and image acquisition was performed with unbiased parameters constant across treatment groups.

2.4.4 3D Monoculture

Three-dimensional cultures of cancer cells were performed according to previously described protocol[102]. Briefly, HT-1080 EB3-mApple cells were suspended in a 2.5 mg mL^{-1} collagen I gel extracted from rat tail (Corning) at the density of 1 million cells mL^{-1}. The collagen gel containing the cells was deposited onto a MatTek dish (MatTek Corp.), and allowed to polymerize at 37°C and pH 8 for 30 min. in a humidified chamber. Following the polymerization, fresh growth media was introduced into the MatTek dish. The cells were imaged with confocal microscopy for MT dynamics following overnight incubation (24 hr.) in a humidified incubator.

2.4.5 MT tracking and feature extraction

EB3 comets were detected and linked to form MT tracks using the U-track software (http://www.utsouthwestern.edu/labs/danuser/software/)[92]. Cell boundaries, in the form of a mask, were constructed using ImageJ. In order for a MT track to be successfully called, it must pass a strict set of filters: (1) be present in a marked cell, (2) comets must be detected in at least three frames, (3) only a maximum of one gap is present, (3) must

travel at least 0.5 µm, and (4) comet persistence must be >0.60. Persistence was

measured on a scale of 0 to 1, where 1 indicated a straight track. These constraints

were enforced either directly using the U-track software or a custom script implemented

in Python (Python3.6) that required a track CSV file, cell mask, and image metadata

containing the image frame rate and resolution as input. The following U-track

parameters and the defined ranges were used to achieve accurate tracking: Low-pass

gaussian st.dev (1-3 pixels); high-pass gaussian st.dev (4-5 pixels); watershed

segmentation minimum threshold (2-3 st. dev); minimum track length after first frame (2-

4); minimum number of gaps (0-1). The remaining parameters were set to the default

settings. After obtaining a resolved set of MT tracks, fourteen features for each track

were calculated:

(1) Average speed (µm s^{-1}), whereby the distance traversed between each frame was

calculated via the python numpy library gradient function, and averaged across the

entire time-lapse for a given track; (2) minimum speed, (3) maximum speed, and (4)

speed standard deviation for a given track across frames; (5) net displacement (µm),

calculated as |track end coordinate - track start coordinate|; (6) path length (µm),

calculated as the total distance traversed by a track; (7) persistence, defined by (net

displacement) x (path length)$^{-1}$; (8) curvature, calculated as a third degree polynomial fit

to the MT track using the numpy python library polyfit function. From this fitted

polynomial, the curvature between frames was computed using equation 1.

$$(1) \quad \kappa = \frac{|\frac{dx}{dt}(\frac{dy}{dt})^2 - \frac{dy}{dt}(\frac{dx}{dt})^2|}{((\frac{dx}{dt})^2 + (\frac{dy}{dt})^2)^{\frac{3}{2}}}$$

x and y are the coordinates of the MT comet at each frame. Curvature was computed at each x-y coordinate and all values were averaged, resulting in one curvature value per track; (9) distance to cell edge, defined by a distance transform image (DT) created from the inverse of the cell mask. The pixel value in the DT image corresponds to the distance from the cell edge. This measurement was normalized to be independent of absolute cell size by dividing the sum of all pixel values that fall within the cell boundaries from the DT image by the total number of pixels inside the cell. Min-max normalization was lastly performed to scale measurements between 0 and 1; (10) distance to the cell major axis was calculated using the regionprops function from the sklearn python package, via the orientation, major_axis_length, and centroid parameters. From these parameters, points on the cell major axis were identified. Distances were normalized by the farthest point from the major axis along the cell boundary, such that all track distance measurements fell between 0 to 1; (11) distance to the cell minor axis was computed and normalized similar to the above, with the minor axis defined as perpendicular to the major axis; (12) local track coherence, calculated by the cosine of the angle between a query track and tracks within 20 µm radius within the same cell, and averaged across all such pairs of tracks; (13) cellular track coherence, calculated similarly to the local track coherence but for all tracks of a given cell rather than within a given radius; (14) track orientation, calculated as the cosine of the angle between the query track and the cell major axis. All features were calculated using python scripts. Track visualizations were constructed using either python scripts or GraphPad Prism (Prism 8) software.

To test statistical robustness against unevenly distributed MT track behaviors from cell to cell, a permutation test was performed such that cell labels were shuffled between the different groups. A naïve wilcoxon rank sum test between pairs of cell populations was applied to determine the permutation p-value, for each MT feature. To determine the final p-value for each feature, the number of permutations with a p-value less than the p-value of the true distribution was divided by the total number of permutations. Without any permutations, the reported p-value obtained from a naïve wilcoxon rank sum test was $< 10^{-40}$ in some cases. A maximum of 1000 permutations were run for each experiment. If there were no permutations that had a lower p-value than the naive rank sum test, then the final p-value is reported as p=0.001.

Effect size calculations between two different MT populations (i.e. in vivo, in vitro 2D, etc.) was determined using Cohen's D statistic, measured by equation 2. SD_{pooled} is measured by equation 3.

$$(2)\ Cohen'sD = \frac{\mu_1 - \mu_2}{SD_{pooled}}$$

$$(3)\ SD_{pooled} = \frac{\sqrt{Var_1 + Var_2}}{2}$$

The means of population 1 and 2 are represented by μ_1 and μ_2, and the variances are represented by Var_1 and Var_2, respectively.

Additional tests were conducted to determine the robustness of the analysis. The first test ensured that incompletely imaged cells *in vivo* did not effect the significance

tests. Cells that were more than 20% outside the field of view were omitted during this test and a two-tailed permutation comparing *in vivo* and *in vitro* HT-1080-EB3-mApple cell populations was conducted as described above (**Figure B-8**). The second test ensured that significance between *in vivo* and *in vitro* populations was not the result of noise differences or image quality. Artificial noise was added to a batch of *in vitro* cells (Gaussian noise with 0 mean and 100, 200, and 400 SD in pixels) using the ImageJ add specified noise function. The effect size between the noisy cell populations and the *in vivo* cell populations was measured. Significance was also measured between the artificially noisy and *in vitro* cells with no artificial noise added (**Figure 2-4**).

2.4.6 Principal Component Analysis of MTs

PCA of MT dynamics from the in vivo, in vitro 3D, and in vivo cell populations was performed using the python scikit-learn package on all 14 of the MT features. Outlier tracks, or tracks where any of the feature values were not within 5 and 95 percentile were removed prior the PCA. Furthermore, the naive distribution of several features were not normal and highly skewed. Therefore, several transformations were used depending on the feature type. For features with a right skewed distribution, a log transformation (curvature, displacement, path length, average speed, minimum speed, maximum speed, and speed SD) or sqrt transformation (major axis distance and minor axis distance) was used. For features with a left skewed distribution, sqrt(1-x) transformation (MT orientation and persistence) was used. For the remaining features, no transformations were performed. The transformed dataset consisting of approximately gaussian distributed features were normalized (mean=0, SD=1).

2.4.7 Cell Shape Analysis

Cell contact and shape analyses were implemented using MATLAB
(MATLAB_R2016B) and/or Python. Masks of tumor cells and/or MΦ were obtained via
manual curation or using a custom Cellprofiler pipeline. From the tumor cell masks, the
computed cell circularity was determined using the following equation: $4\pi AP^{-2}$, where A
is the area of tumor cell and P is the perimeter of the tumor cell. To standardize cell
circularity measurements, cell circularities for cells grown under the control conditions
were normalized (0 mean, 1 SD), while cell circularities for cells grown in other
conditions were transformed according the pre-normalized circularity measurements
from the control condition. In addition to circularity, cell eccentricity was also calculated
from the MATLAB or python skimage regionprops function.

Chapter 3 *In vivo* microscopy reveals macrophage polarization locally promotes coherent microtubule dynamics in migrating cancer cells.

The material in the chapter has been published in Luthria et al., Nature Communications (2020).

Abstract

Among analyzed microtubule features in chapter 2, cancer cells *in vivo* displayed higher coherent orientation of MT dynamics along their cell major axes compared with 2D *in vitro* cultures, and distinctly from 3D collagen gel cultures. This *vivo* MT phenotype was reproduced *in vitro* when cells were co-cultured with IL4-polarized MΦ. Furthermore, MΦ depletion, MT disruption, targeted kinase inhibition, and altered MΦ polarization via IL10R blockade all reduced MT coherence and/or tumor cell elongation. We also show that MT coherence is a defining feature for *in vivo* tumor cell dynamics and migration, and is modulated by local signaling from pro-tumor macrophages.

3.1 Introduction

Based on in vivo results presented in chapter 2, MTs establish directional cell polarity and juxtacrine signaling with neighboring cells[67–69]. We hypothesized that local intercellular interactions could contribute to the observed coherence of MTs *in vivo*. In addition to cancer cells, the TME is typically rich in other cell populations, including Tumor Associated Macrophages (TAMs). TAMs are among the most abundant leukocytes in the HT1080 xenograft model[103] and in a large fraction of patient tumors[104]. TAM accumulation has been associated with disease progression, angiogenesis, and metastasis[105,106]. Using the same tumor xenograft model, our group has observed by histology, flow-cytometry, and IVM an overall ratio of roughly 1:4 in the relative content of TAMs:HT1080 tumor cells, although this varies across tumor regions[91,107]. These observations motivated us to ask whether TAMs could be contributing to the coherent MT behavior of tumor cells found *in vivo*.

To address these questions we applied the imaging and computational pipeline developed in chapter two to measure how MT dynamics change while interacting with TAMs. We measured MT dynamical features in for *in vitro and* in vivo systems in two different cancer models. Analyses presented in chapter 2 revealed that *in vivo*, MT growth in cancer cells was aligned along the cell major axis and coherently with each other in the same cell, which correlated with elongated cell morphology. Intriguingly, these properties were especially enriched in cancer cells that neighbored tumor associated macrophages (TAMs). Coherent MT dynamics induced by neighboring MΦ were disrupted by drugs targeting epidermal growth factor receptor (EGFR) on tumor cells, and MΦ polarization via interleukin 10 receptor, IL10R. Acute disruption in

signaling and MT dynamics, via targeting of phosphoinositide 3-kinase (PI3K), preceded

subsequent changes in gross cell shape, and MT-destabilizing vinblastine confirmed

cellular elongation *in vivo* was MT-dependent. Overall, we present a platform for

examining the *in situ* dynamics of MTs in live xenograft models of cancer, revealing MT

coherence as a defining feature of *in vivo* tumor cell motility, and that pro-tumor MΦ

signaling can produce such MT coherence in neighboring tumor cells.

3.2 Results

3.2.1 TAMs regulate MT alignment in neighboring tumor cells

Multicolor IVM co-imaged MT tracks and neighboring TAMs using a genetically engineered reporter mouse model with knock-in expression of GFP in place of one functional copy of Mertk (*NOD.SCID Mertk*[GFP/+]), which has been validated by imaging and flow cytometry experiments for its high and selective expression in TAMs in this xenograft model[107,108]. Mertk heterozygosity exerts minor[109] and in some cases undetectable[110] impacts on disease progression compared to *Mertk*^{-/-} phenotypes. IVM revealed that TAMs frequently neighbored or even wrapped around MT-rich tumor cell protrusions, including near vessels and fibers of collagen-rich extracellular matrix (**Figure 3-1**).

To test whether TAMs influence MT coherence, we analyzed EB3 MT tracks in HT1080 and ES2 cells grown ± MΦ co-culture (**Figure 3-2C,D**). Bone-marrow derived MΦ were differentiated by macrophage colony-stimulating factor (MCSF) and polarized with interleukin-4 to produce M2-like MΦ (referred to here as IL4-MΦ), resembling tumor-promoting TAM phenotypes[106]. After IL4-MΦ co-culturing, we imaged tumor cells in contact with MΦ and quantified their EB3 tracks. Only two MT features showed consistent changes in co-culture vs. monoculture, across both cell lines: MT coherence and orientation (**Figure 3-2C,D; Figure C-1,C-2,C-3**), which also differed in the *in vivo* vs. *in vitro* comparison (**Figure 2-3**). This generalized to IL4-MΦ derived from the RAW264.7 MΦ cell line (HT1080 in **Figure 3-2D**), thus showing MΦ influence on tumor cell MT dynamics in 2 cancer cell lines and 2 MΦ models.
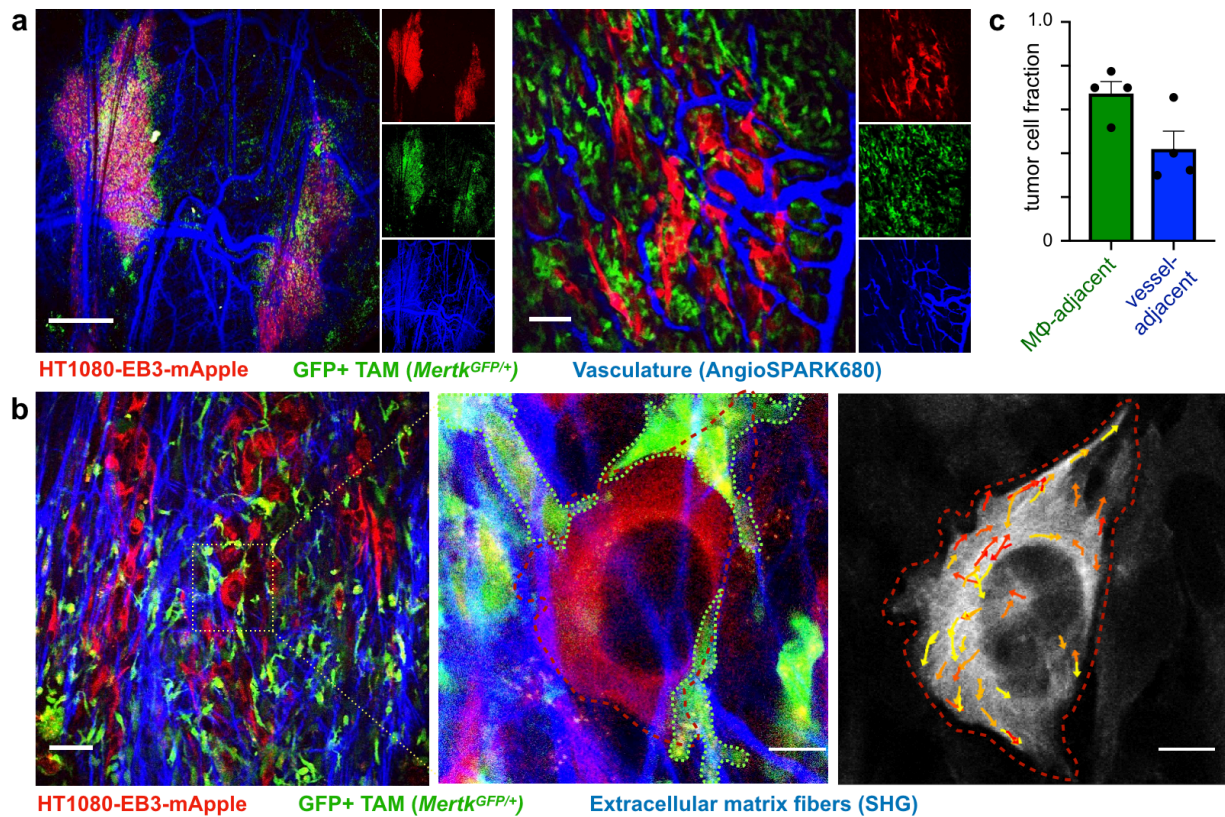
HT1080-EB3-mApple   **GFP+ TAM (*Mertk^GFP/+*)**   **Vasculature (AngioSPARK680)**

HT1080-EB3-mApple   **GFP+ TAM (*Mertk^GFP/+*)**   **Extracellular matrix fibers (SHG)**

Figure 3-1. TAMs frequently neighbor tumor cells near vasculature and fibrillar extracellular matrix. (A-B) Representative IVM of HT1080 tumors grown subcutaneously in the dorsal window chamber of MertkGFP/+ NOD.SCID mice at low (left) and high (right) magnifications. (A) A long-circulating fluorescent NP, angiospark-680, and (B) 2-photon microscopy of second harmonic generation, SHG show tumor vasculature and fibrillar extracellular matrix, respectively. At bottom right, EB3 tracks are shown randomly pseudocolored for visualization. Scale bars are 1mm (A, right), 50μm (A-B, left), and 10μm (B, right). (C) Corresponding to images as in A, tumor cells were scored based on nearest proximity (<5μm) to GFP+ TAMs or AngioSPARK+ vasculature (data are means ± s.e.m.). For all, n=80 total cells and n=4 tumors overlaid as individual data points in C. Source data are provided as a source data file.

3.2.2 MΦ polarization impacts MT dynamics of adjacent tumor cells.

.   Although TAMs frequently exhibit tumor-promoting phenotypes, in reality they

can exist across a spectrum of MΦ polarization states. We therefore examined the

effect of MΦ polarization on MT dynamics in co-cultured tumor cells. MCSF-

differentiated MΦ modeled what past literature has described as a M0-like phenotype,

referred to here as simply MΦ [111]. We further polarized MΦ either with IL-4 (described

above) or with lipopolysaccharide and interferon gamma to produce M1-like MΦ[112],

referred to here as LPS/IFNγ-MΦ. We imaged MΦ-adjacent tumor cells in each co-

culture and quantified the MT features (**Figure C-4**), ultimately focusing on MT

coherence and orientation based on above results. Since these two features relate to

one another, yet are highly variable, we used PCA and a single principal component

(PC) to capture distributions of both features simultaneously. The comparison in PC

distributions revealed that only *in vivo* and IL4-MΦ co-culture tracks displayed higher

MT coherence and orientation compared to monoculture (**Figure 3-3A**). Pairwise

differences in PC distributions (**Figure C-2**) and statistical effect size (**Figure 3-3B**)

indicated IL4-MΦ co-culture tracks were most similar among all conditions to the *in vivo*

tracks. These data suggest that TAM effects on MT dynamics depend on the underlying
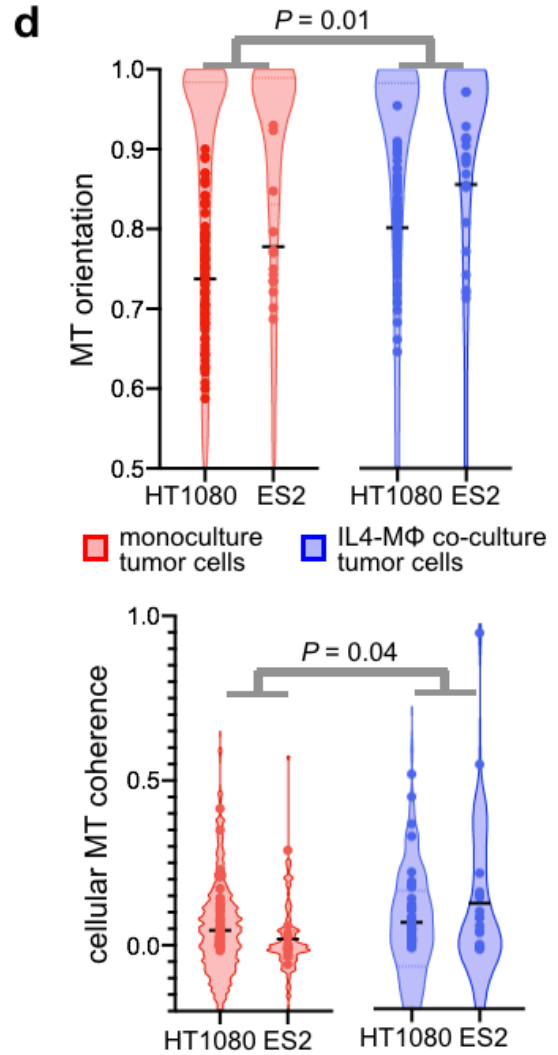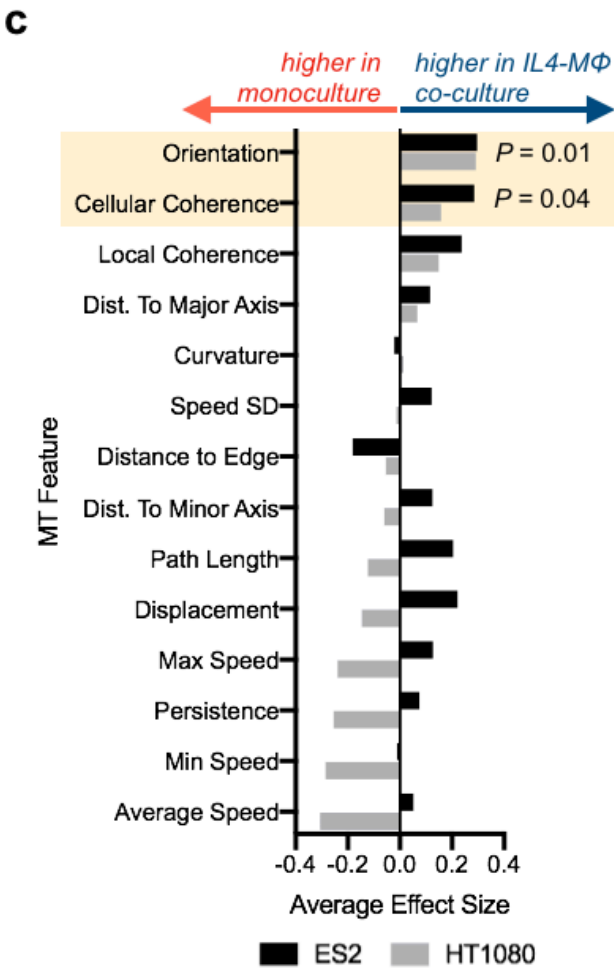
TAM polarization state.

a ES2-EB3-mApple
IL4-MΦ (VT680 - NP+)

b HT1080-EB3-mApple
GFP+ IL4-MΦ (*Mertk^{GFP/+}*)

c

higher in monoculture ← → *higher in IL4-MΦ co-culture*

MT Feature (top to bottom):
- Orientation — *P* = 0.01
- Cellular Coherence — *P* = 0.04
- Local Coherence
- Dist. To Major Axis
- Curvature
- Speed SD
- Distance to Edge
- Dist. To Minor Axis
- Path Length
- Displacement
- Max Speed
- Persistence
- Min Speed
- Average Speed

Average Effect Size: -0.4, -0.2, 0.0, 0.2, 0.4

■ ES2   ■ HT1080

d

P = 0.01

MT orientation (HT1080, ES2 / HT1080, ES2)

□ monoculture tumor cells   □ IL4-MΦ co-culture tumor cells

P = 0.04

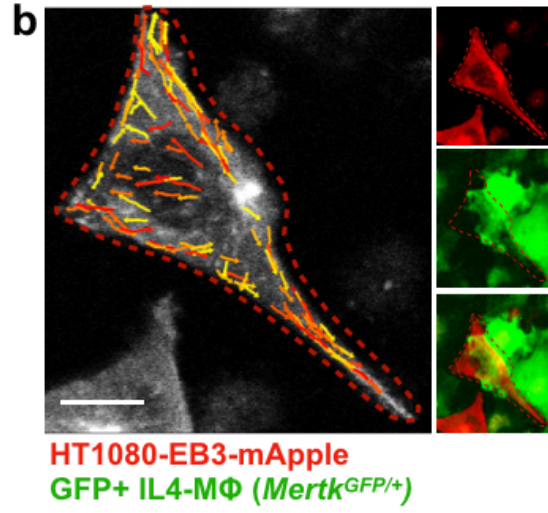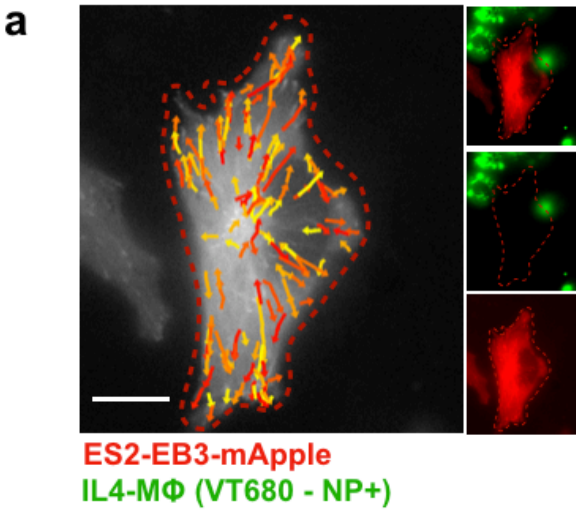cellular MT coherence (HT1080, ES2 / HT1080, ES2)

57

Figure 3-2. IL4-polarized MΦ promote coherent MT alignment in neighboring tumor cells.

(A-B) Representative fluorescence microscopy after 24 hrs of IL4-MΦ co-culture with EB3 tracks randomly pseudo-colored for visualization (scale bar = 10 μm). (C) Corresponding to A-B, the effect size for imaged MT features was compared between monoculture and 24 hr MΦ co-culture (average of Cohen's D effect size between batches). (D) From C, track distributions for the top two increased MT features, altered in both cell lines with co-culture, are shown with cell averages overlaid as individual data points (bar denotes median). All p-values were computed using a two-tailed permutation test with BH correction. For HT1080 cells, n=22,371 tracks across n=164 total cells were analyzed, and for ES2 cells n=1,424 tracks across n=33 total cells were analyzed. Source data are provided as a source data file.

3.2.3 Kinase signaling disruption blocks MΦ-mediated MT coherence

TAMs and tumor cells signal bidirectionally through multiple pathways. For instance, reports show TAM-produced ligands such as epidermal growth factor (EGF) signal to EGFR on cancer cells to promote cell migration[113,114]. In turn, tumor cell-produced ligands such as colony stimulating factor 1 (CSF1) signal to CSF1R on TAMs to promote recruitment and M2-like polarization[113,115]. Downstream PI3K signaling is implicated in such signaling and MT dynamics[116,117], and in TAMs, reports show PI3K inhibition (particularly of isoform p110γ) reprograms cells toward M1-like polarization[118].
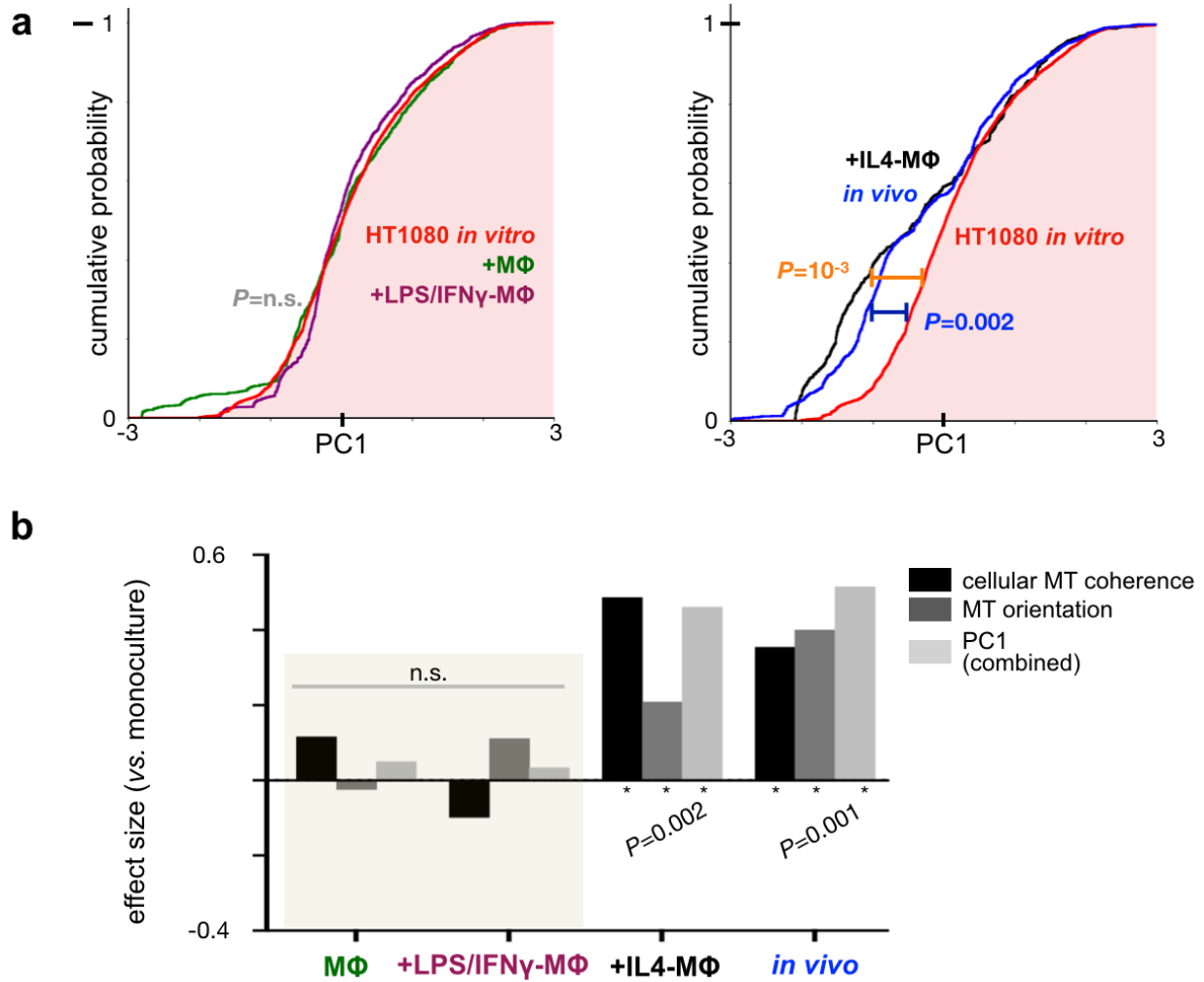
Figure 3-3. MΦ polarization results in increased MT coherence. (A) HT1080 MT cellular coherence and orientation were combined into a principal component (PC) for each MT track, and the cumulative distribution function of PC scores was calculated (*two-tailed permutation test; total n=10,968 tracks from n=118 total cells). (B) Effect sizes were calculated from results shown in A (*two-tailed permutation test using PC scores).

Given this evidence, we hypothesized that receptors and PI3K govern MΦ-mediated MT polarization in tumor cells. We tested drugs and antibodies targeting (1) tumor-expressed receptors, including the RTKs EGFR and AXL, and integrin β1 (heterodimerizing with α-integrins to bind ECM); (2) TAM-expressed receptors influencing TAM polarization, including toll-like receptor 7/8 (TLR7/8) and the RTKs MERTK and CSF1R; (3) PI3K isoforms including leukocyte selective p110δ and p110γ; and (4) Rho associated protein kinase (ROCK) as a representative effector of Rho-family GTPases. ES2 co-cultured with IL4-MΦ were treated for 2-4 hr., and imaged MT features revealed that all treatments qualitatively decreased MT coherence and orientation, although only treatment with inhibitors targeting ROCK, PI3Kγ, and EGFR elicited significant effects (**Figures 3-4; C-5**). In support, analogous experiments in HT1080 also showed effects from targeting EGFR and PI3Kγ, under IL4-MΦ but not other co-culture or monoculture conditions (**Figure 3-5; C-6**). These data thus suggest that coherent MT dynamics depend on context-dependent signaling activity in both MΦ and cancer cells.
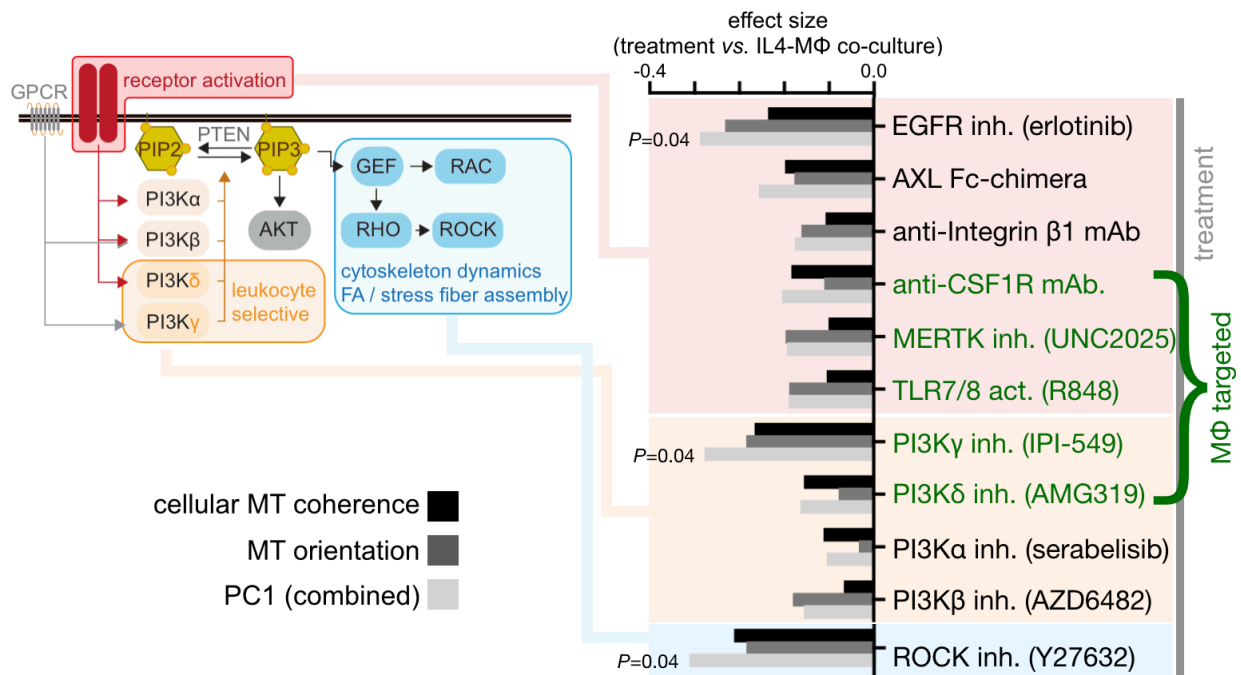
Figure 3-4. Overview of MΦ-induced MT disruption screen.

ES2 MT dynamics were imaged after 24 hr co-culture followed by 2-4 hr of drug treatment, and effect sizes were calculated as in B, however here in comparison to IL4-MΦ co-culture (*two-tailed permutation test on PC scores with BH multiple hypothesis correction, fdr=0.05; n=29,591 tracks from n=151 total cells).

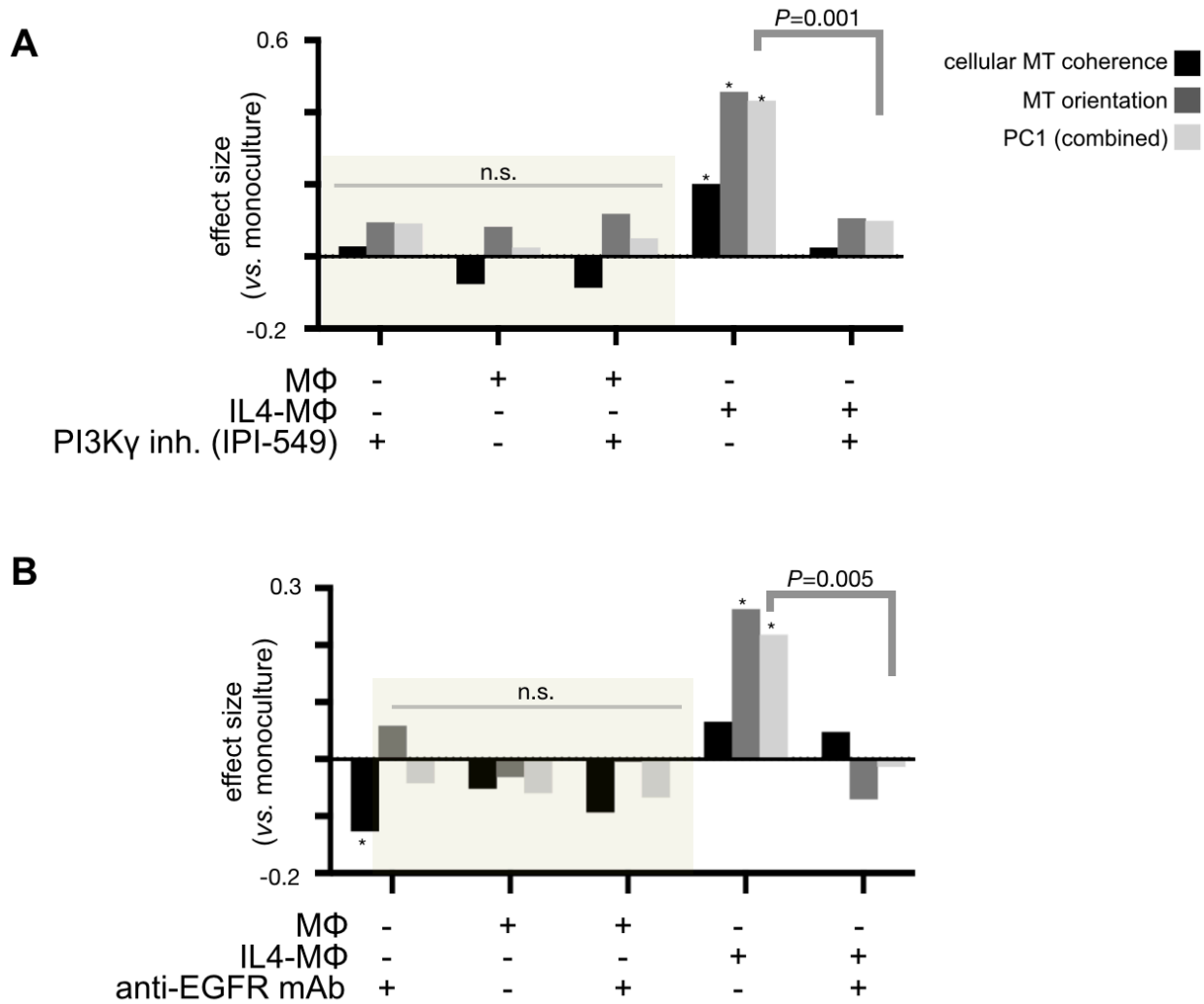**Figure 3-5. Disruption of MΦ-induced MT coherence by targeted inhibition of cell signaling.** (A-B) HT1080 MT dynamics were imaged after 24 hr co-culture followed by 2-4 hr. of drug treatment, and effect sizes were calculated as in Figure 3-2 (*two-tailed permutation test on PC scores; IPI-549(A): n=13,380 tracks from n=80 total cells; anti-EGFR(B) mAb: n=16,427 tracks from n=112 total cells).

3.2.4 MΦ contact promotes pseudopod-like extensions in tumor cells

Although MT dynamics may outpace the kinetics of bulk change in cell shape and migration (discussed further below), under more equilibrated conditions MT structure and cell shape can correlate with one another[72]. Because IL4-MΦ enhanced MT orientation in tumor cells, we hypothesized that co-cultured IL4-MΦ would also influence tumor cell shape. To determine whether such impacts depended on spatial MΦ / tumor cell proximity, HT1080 were also grown in conditioned media that had been incubated with IL4-MΦ for 24 hr. and then transferred to HT1080 for 18 hr. We used PCA to interpret coordinated changes in shape features (rather than MT dynamics as above). HT1080 co-cultured directly with IL4-MΦ shifted toward elongated, less circular shapes, and conditioned media elicited lower magnitude effects (**Figure 3-6A**). The circularity shape feature exhibited the most negative loading on the first PC (**Figure 3-6A**), substantially decreased with co-culture (**Figure 3-6B**), and therefore was used as a representative metric in subsequent analyses. Overall, MΦ-enhanced MT coherence in tumor cells was matched with correspondingly decreased tumor cell circularity.
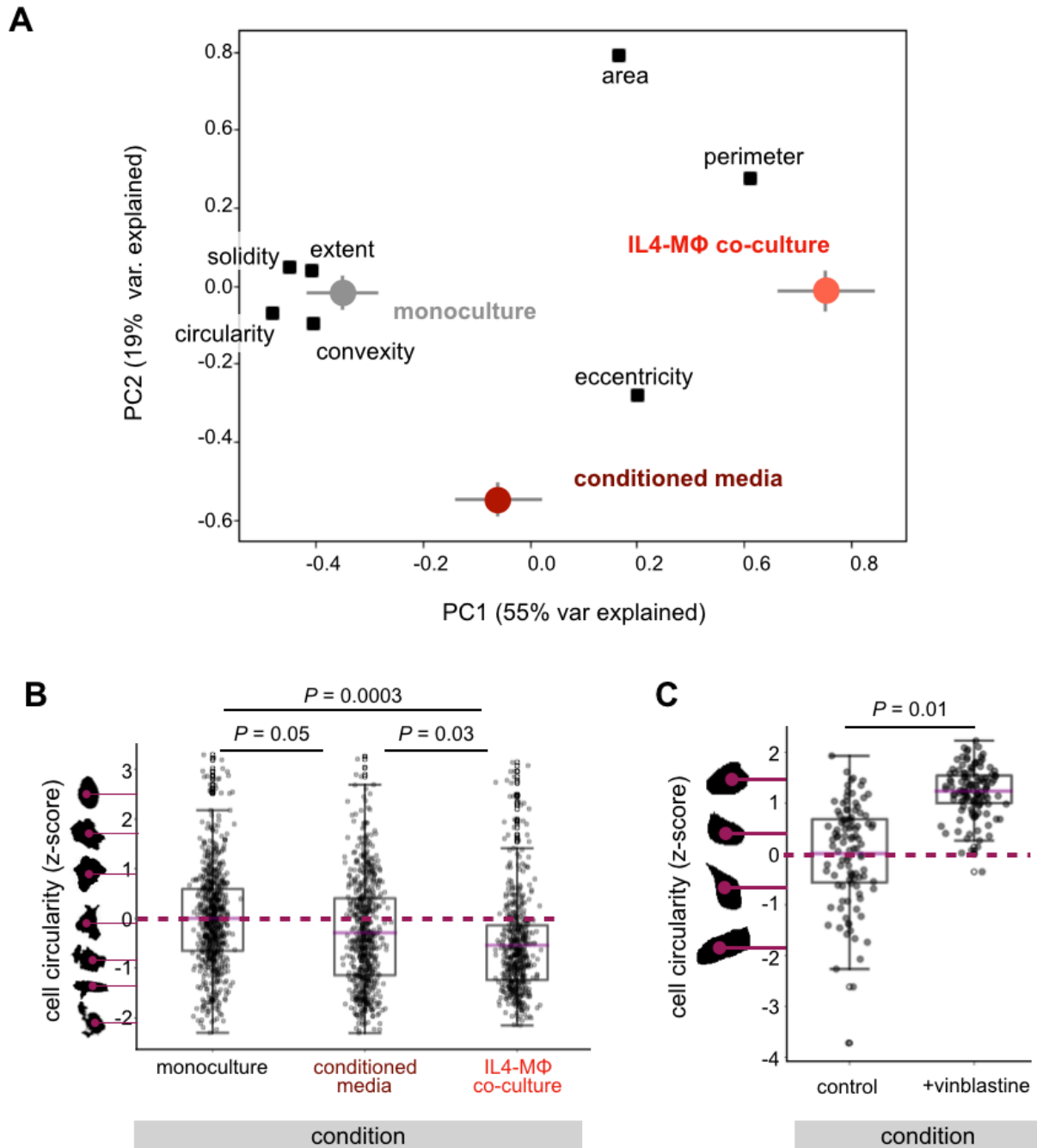
Figure 3-6. (A,B) HT1080-mem-mApple cells were imaged after being cultured for 24 hrs in three different conditions. (A) PCA captures cell shape feature loadings (black) and scores for cells under these conditions (mean PC score ± s.e.m). (B) Single-cell circularity measurements, which exhibited the most negative PC1 loading in A, were directly compared (*two-tailed t-test; n=1,906 total cells across 23 replicate images; box plot as 25%tile, median, 75%tile with outliers

outside 1.5*IQR). (C) HT1080-mem-mApple tumor-bearing nu/nu mice were treated with 6 mg

kg-1 vinblastine or vehicle, and confocally imaged 24 hr later (*two-tailed Mann-Whitney U test;

n=225 total cells, n=4 tumors per group; box plots as in B).
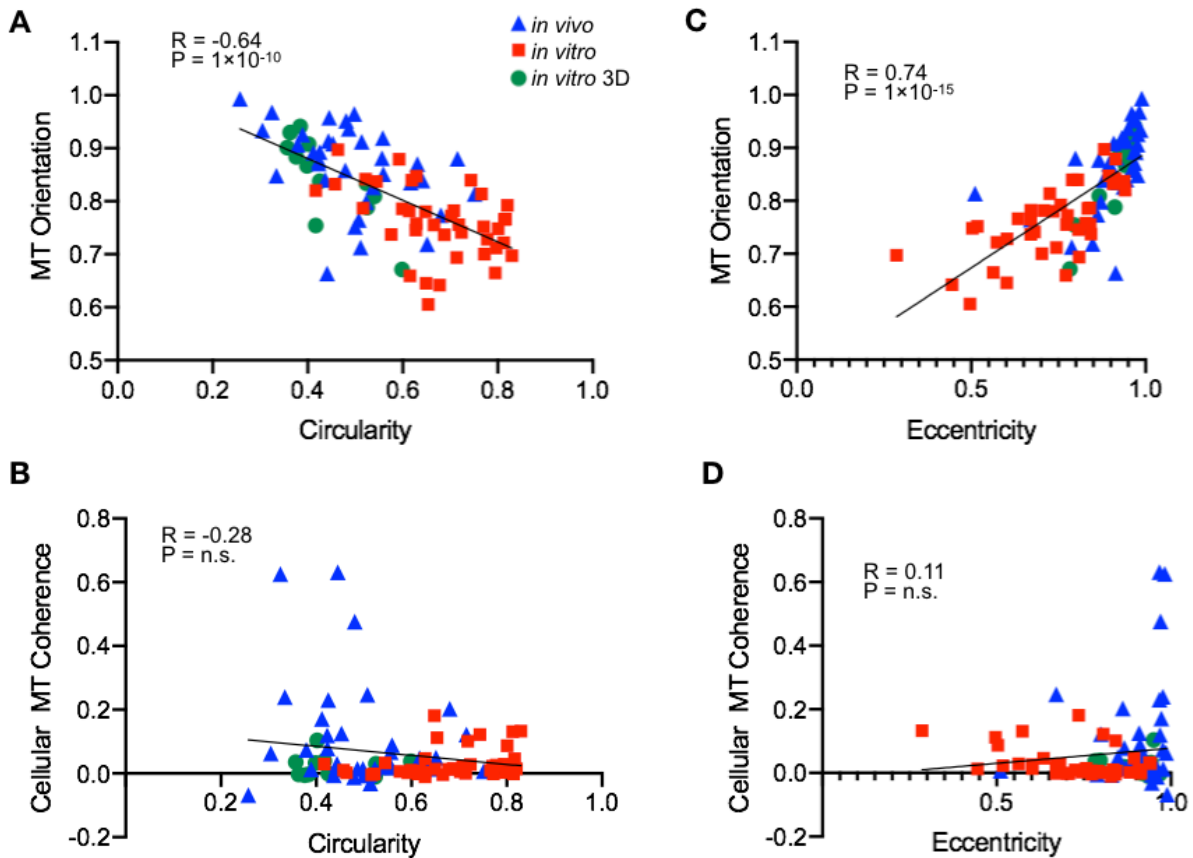
Figure 3-7. Correlations between cell shape and MT behaviors.

(A) Cellular circularity was correlated with average MT orientation across individual HT1080

EB3-mApple cells grown under the indicated conditions (data points denote individual cells;

*two-tailed exact test). (B-D) Similar to A, (B) cellular circularity was correlated to MT cellular

coherence, cellular eccentricity was correlated to (C) MT orientation and (D) MT cellular

coherence across individual HT1080 cells (A-D: *two-tailed F-test; n=85 cells from three

different experimental conditions).

Although care must be taken in interpreting shape from confocal images with narrow focal planes, we nonetheless found correlation between cell shape and MT dynamics, even within heterogeneous populations of cells imaged under the same *in vitro* or *in vivo* conditions (**Figure 3-7**). To directly test the dependence of elongated cell shape on MT structure, we treated mice bearing HT1080 tumors with 6 mg kg^{-1} MT destabilizing drug vinblastine[119]. 24 hr following treatment, tumors were confocally imaged to quantify cell shape from a membrane-tagged fluorescent protein (mem-mApple). Cells with intact non-fragmented nuclear morphology in vinblastine-treated tumors exhibited increased circularity (**Figure 3-6C**) compared to cells from untreated tumors. Taken together, MT dynamics correlated with elongated cell shape, and MT polymerization was required for such elongation *in vivo*.

We next analyzed the spatial dependence by which MΦ could impact tumor cell shape. Although HT1080 and IL4-MΦ co-cultures were well-mixed, stochastic distributions created diversity in the distance between tumor cells and their closest neighboring MΦ (**Figure 3-8A**). We therefore asked whether spatial MΦ proximity correlated with tumor cell circularity on a cell-by-cell basis, using an automated nearest-neighbor analysis. Segmented tumor cell circularity was computed and algorithmically binned into one of three groups (low, medium, and high; see representative cell masks in **Figure 3-8B**). Next, we queried the proportion of cells in each group in contact (<5 μm), nearby (6-30 μm), or far (>30 μm) from the nearest MΦ. This revealed enrichment in cell elongation among cells in close proximity with IL4-MΦ: tumor cells with low circularity were 5 times more likely to be in contact with, rather than far from MΦ, while tumor cells with high circularity showed no such bias (**Figure 3-8B**).

Given the *in vitro* evidence showing local effects of MΦ on tumor cells, we used an orthotopic mouse model of disseminated OVCA to study whether similar spatially-dependent interactions could be observed in a relevant *in vivo* model of disease. We imaged disseminated tumors that formed roughly 1 week following intraperitoneal (i.p.) injection of ES2 cells. Upon terminal dissection of tumor-bearing organs (omentum, liver, ovary, and peritoneal wall), ES2 cells expressing cytoplasmic GFP were confocally imaged).

In this experiment, MΦ were imaged using a fluorescent polyglucose-based nanoparticle (NP) recently demonstrated to accumulate with >90% selectivity in MΦ in multiple mouse models of cancer[120] (**Figure 3-9A**). ES2 cells growing in intraperitoneal metastases were on average more circular than HT1080 growing on tissue culture plastic and ES2 cells growing in subcutaneous xenografts (**Figure 3-10**). Shape-based stratification binning was correspondingly adjusted. For each circularity bin, we queried the proportion of cells that were within 2 μm of the nearest NP+ MΦ. Similar to the *in vitro* HT1080 experiment, elongated tumor cells exhibited a clear bias for spatial proximity to MΦ in ES2 tumors (**Figure 3-9B**). Thus, analyses across two distinct models demonstrated that cancer cells nearby MΦ displayed a relatively more elongated shape.

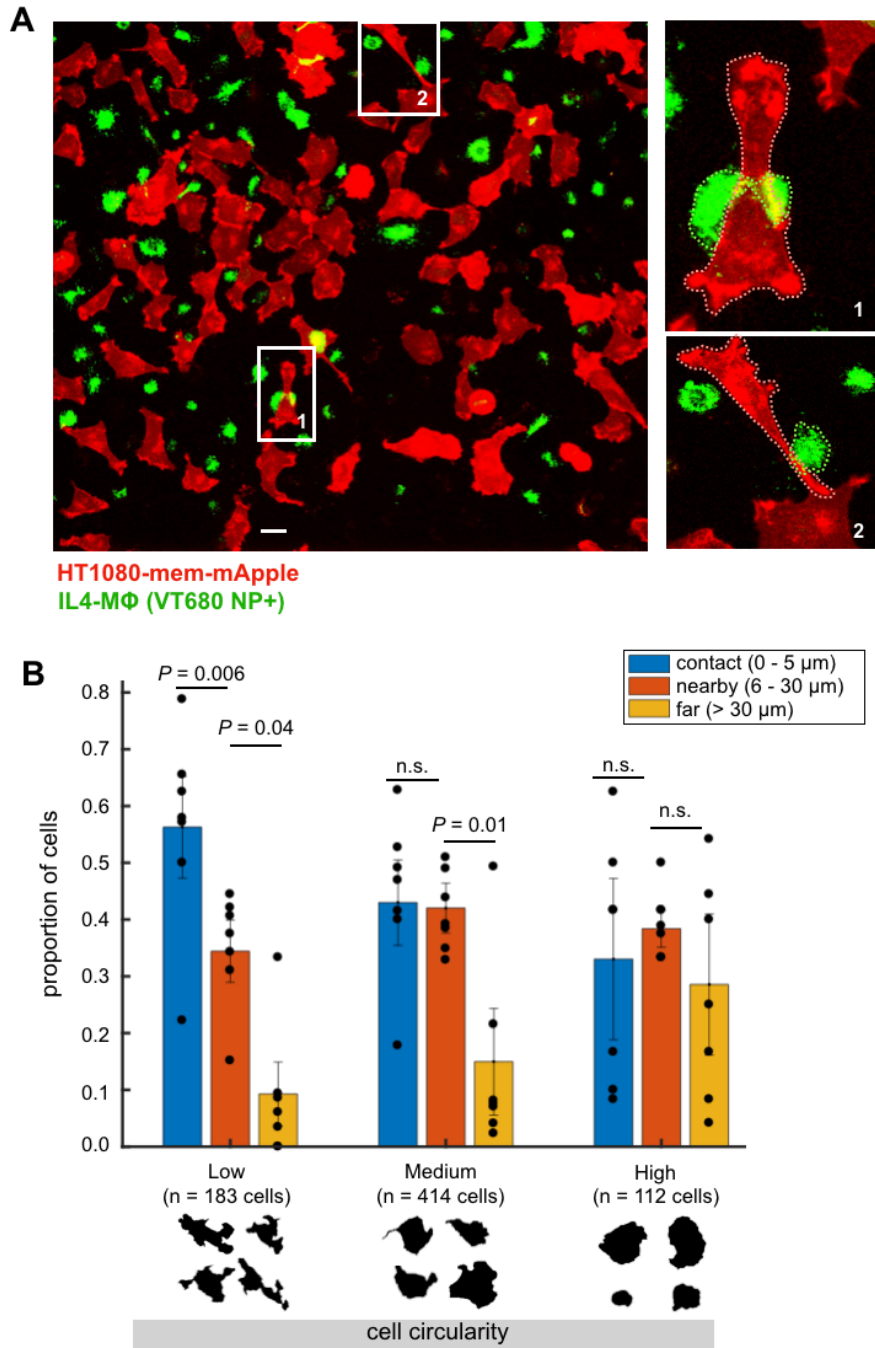**Figure 3-8. MΦ promote pseudopod-like extensions in neighboring HT1080 tumor cells *in vitro*.** (A) Representative co-culture imaging, highlighting instances at right of co-localized MΦ and tumor cell protrusion (scale bar = 50μm). (B) Cancer cell circularity from D was measured according to MΦ proximity (*chi-squared test; n=709 total cells across n=7 image replicates denoted by points; mean ± s.e.m.).

To more directly test the impact of MΦ on tumor cell shape, we depleted MΦ within intraperitoneal ES2 tumors using i.p. administration of clodronate liposomes (clod-lip)[121] (**Figure 3-10B**), and found increased ES2 circularity (**Figure 3-9C**). These results confirm that TAMs promote elongation in neighboring tumor cells, and furthermore show that TAMs can be manipulated to impact tumor cell morphology.

3.2.5 MΦ associate with protrusions in migrating tumor cells

We next examined whether MΦ-induced changes in MT coherence and cellular elongation corresponded to enhanced cancer cell migration. Because of known morphological differences between motile and non-motile cells[72], we hypothesized that tumor cells with a more circular morphology had slower migration rates than elongated cells. We used roughly 2 hr time-lapse IVM (as in **Figure 2-3**; see ref. XX) of HT1080 xenografts to measure cell migration by tracking individual cell centroid movements. The migration rate for all cells was 0.15 +/- 0.14 µm min^{-1} (mean +/- s.d.). As predicted, cell circularity correlated negatively with cell migration, and all cells with migration >0.25 µm min^{-1} had circularity ≤ 0.4 (**Figure 3-11A**).
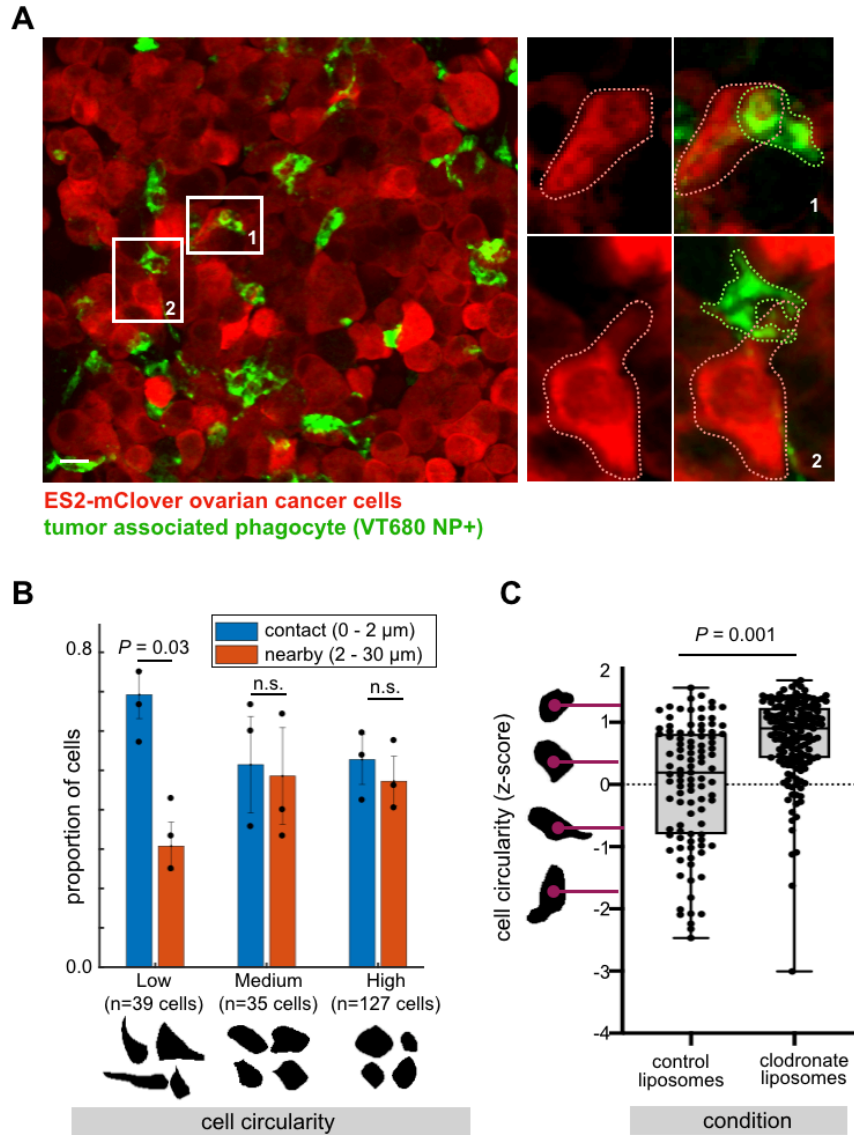
A

ES2-mClover ovarian cancer cells
tumor associated phagocyte (VT680 NP+)

B

contact (0 - 2 μm)
nearby (2 - 30 μm)

P = 0.03   n.s.   n.s.

proportion of cells

Low
(n=39 cells)   Medium
(n=35 cells)   High
(n=127 cells)

cell circularity

C

P = 0.001

cell circularity (z-score)

control
liposomes   clodronate
liposomes

condition

Figure 3-9. MΦ promote pseudopod-like extensions in neighboring ES2 tumor cells *in*

vivo. (A) Representative confocal microscopy of disseminated intraperitoneal tumors,

highlighting TAM-adjacent elongated tumor cells on right (scale bar = 20μm). (B) As in F, ES2

circularity was measured as a function of TAM proximity (*chi-squared test; n=201 total cells

across n=3 tumors denoted by points; mean ± s.e.m.). (C) Excised ES2 tumors were confocally

imaged for cell circularity, following treatment with PBS or clodronate liposomes (*two-tailed t-

test; n=261 cells across n=13 tumors per group; box plot as minimum, 25%tile, median, 75%tile,
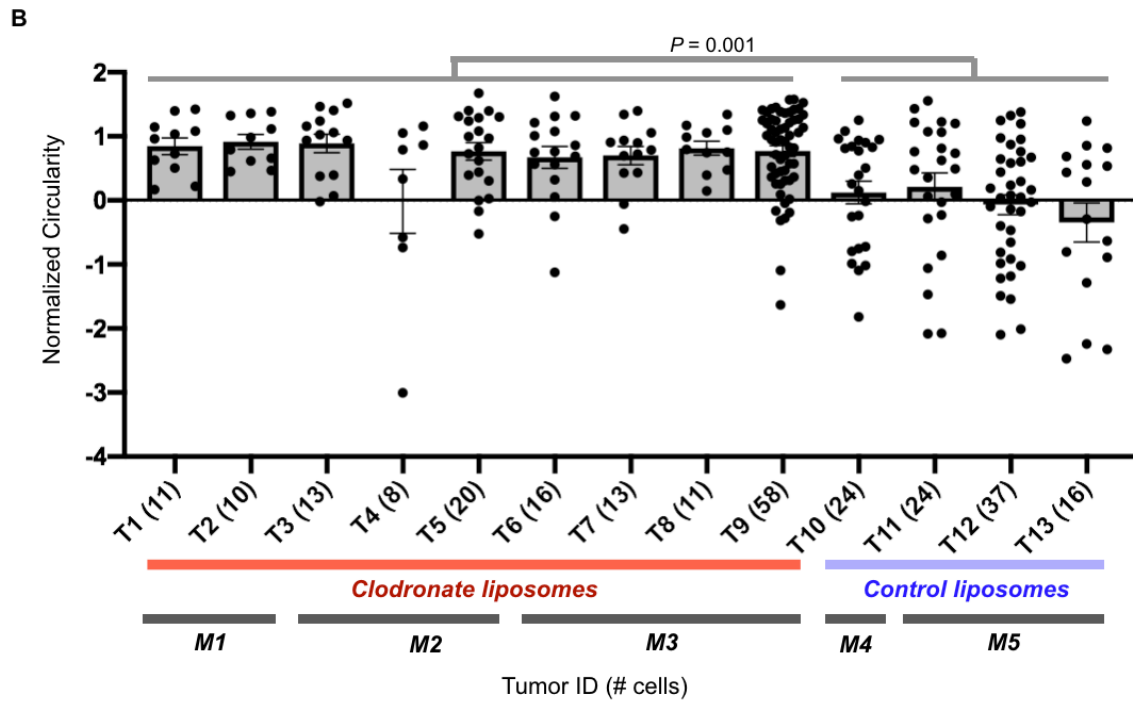
and maximum).

A

Control (PBS) liposomes
60μm
20μm

Clodronate liposomes
60μm
20μm

ES2-mClover ovarian cancer cells
tumor associated phagocyte (VT680 NP+)

C

20μm
20μm

ES2-EB3-mApple cells
tumor associated phagocyte (VT680 NP+)

B

P = 0.001

Normalized Circularity

T1 (11) T2 (10) T3 (13) T4 (8) T5 (20) T6 (16) T7 (13) T8 (11) T9 (58) T10 (24) T11 (24) T12 (37) T13 (16)

Clodronate liposomes   *Control liposomes*

M1   *M2*   *M3*   *M4*   *M5*
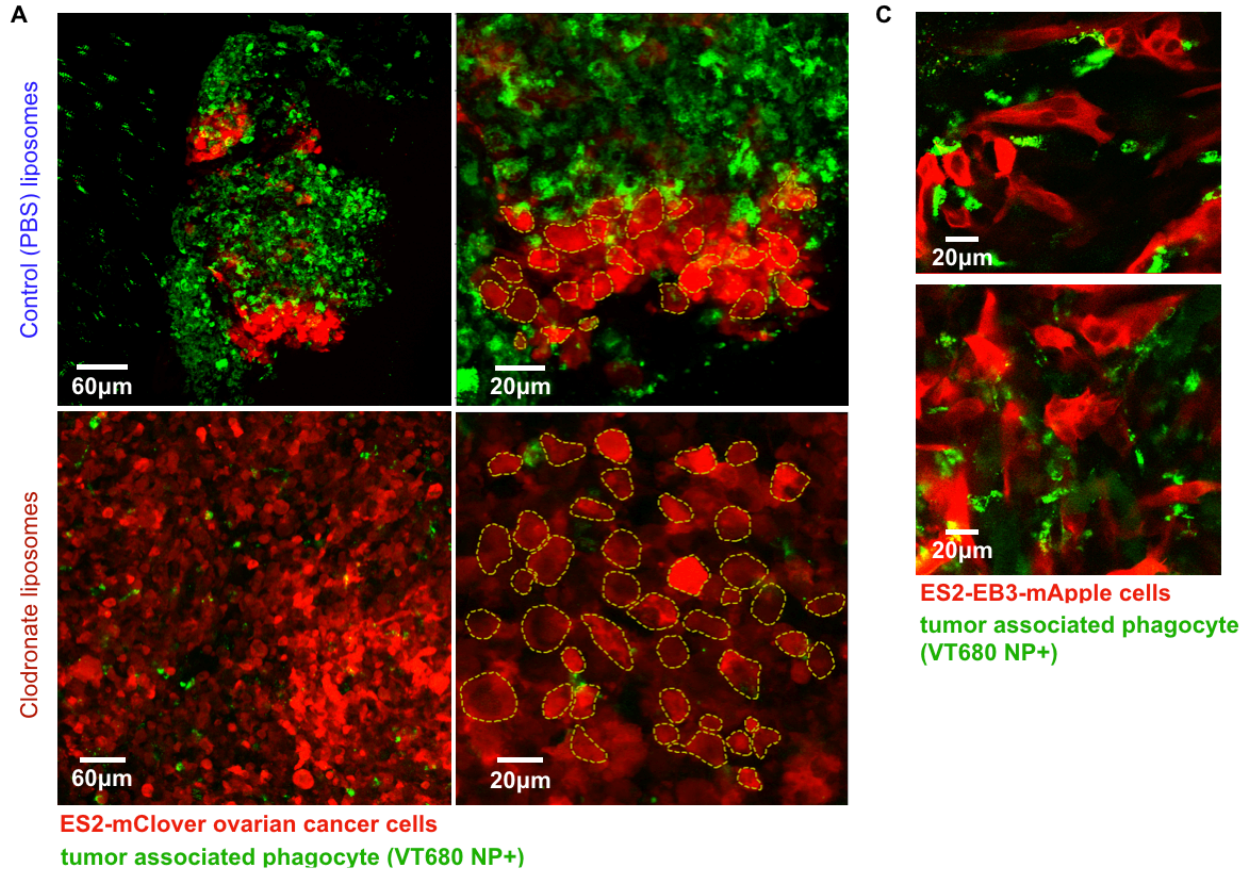
Tumor ID (# cells)

Figure 3-10. Quantifying tumor cell shape in response to clodronate liposome treatment.
Corresponding to Figure 3-9, ES2 tumors via intraperitoneal injectection were treated with liposomes containing either clodronate or PBS as a vehicle control, and imaged confocally for cell shape. (A) Representative images and (B) quantification of single-cell circularities across tumors within the cohorts are shown (*two-tailed t-test, n=261 cells across n=13 tumors; error bars denote mean±s.e.m. for each group). (C) ES2 tumor cells were also implanted subcutaneously and imaged using a dorsal window chamber.

Additionally, we tracked tumor phagocytes including TAMs by simultaneously imaging a fluorescently tagged NP (**Figure 3-11B**)[91]. Examples show phagocytic myeloid cells associating with and wrapping around protrusions of migrating cancer cells (**Figure 3-11B, 3-11C**), which correlated with greater cellular elongation and more rapid migration compared to non-TAM associated cancer cells within the same tumor (**Figure 3-11**). These data (**Figure 3-11B**) show that TAMs do not always co-migrate with tumor cells. Relatedly, MT dynamics were only mildly correlated with subcellular TAM positions relative to tumor cells (**Figure C-11**), such that TAMs were not always located at the leading tip of elongated tumor cells. These high-resolution data suggest that TAMs may not directly lead, but nonetheless interact with and likely guide cancer cells in a localized manner.
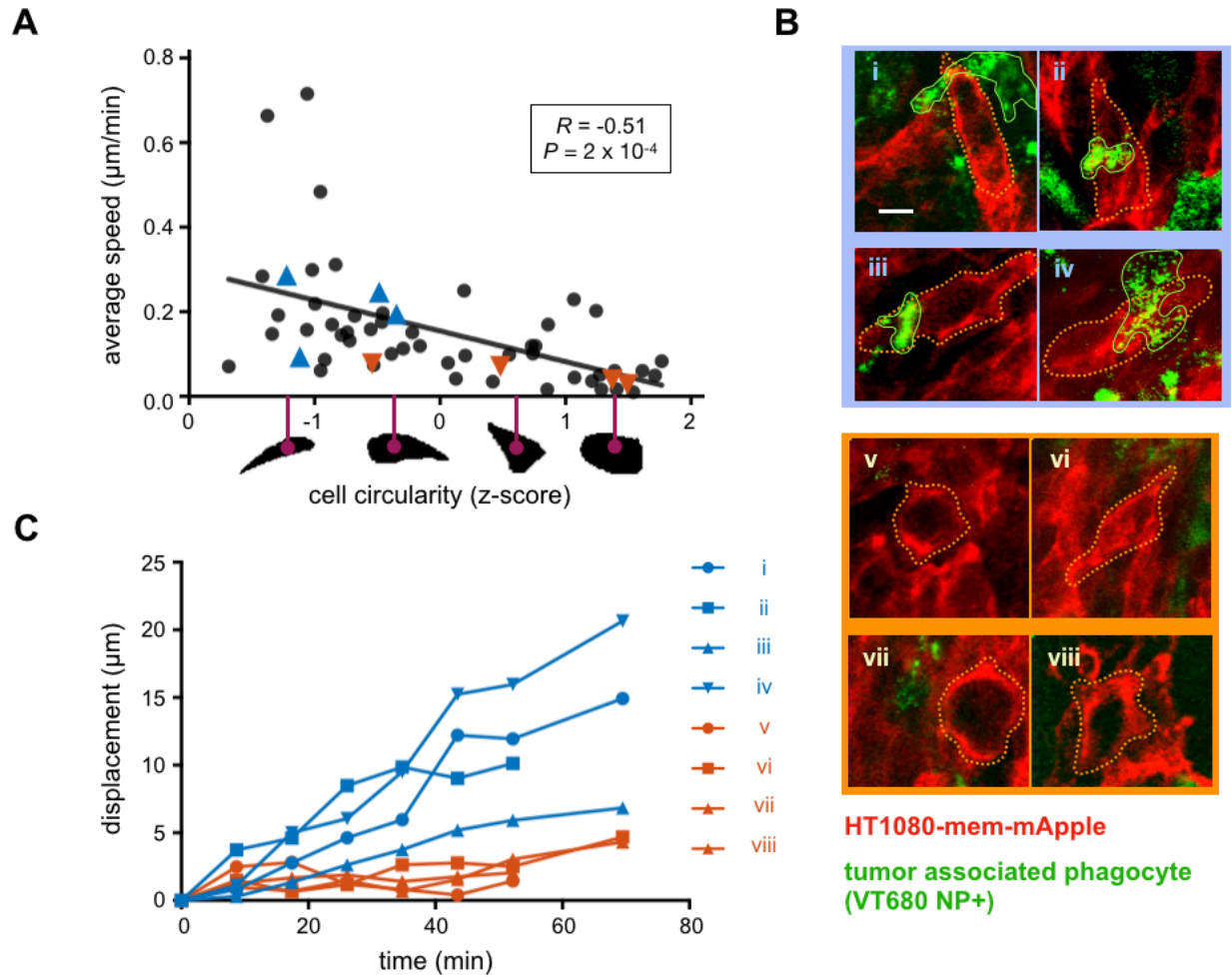
Figure 3-11. TAMs associate with pseudopod-like protrusions in migrating cancer cells.

Time-lapse IVM tracked migration of individual HT1080-mem-mApple cells in tumors within the dorsal window chamber model. (A) Migration speed was correlated with cell circularity (data points are n=50 individual cells across n=4 tumors; *two-tailed f-test on cell level data). Blue and red correspond to cancer cells associated with TAMs or not, respectively, in B-C. (B-C) Representative tumor cells associated with TAMs (i-iv) or not (v-viii) are shown (B; scale bar = 10μm) with corresponding migration (C).

A

HT1080-mem-mApple
tumor associated phagocyte (VT680 NP+)
vasculature (BODIPY NP+)

B

t = 0 min   9 min   17 min

26 min   35 min   44 min

C

$R = -0.31$
$P = 0.03$

avg. speed (µm/min)

distance to TAM (µm)

$P = 0.005$

avg. speed (µm/min)
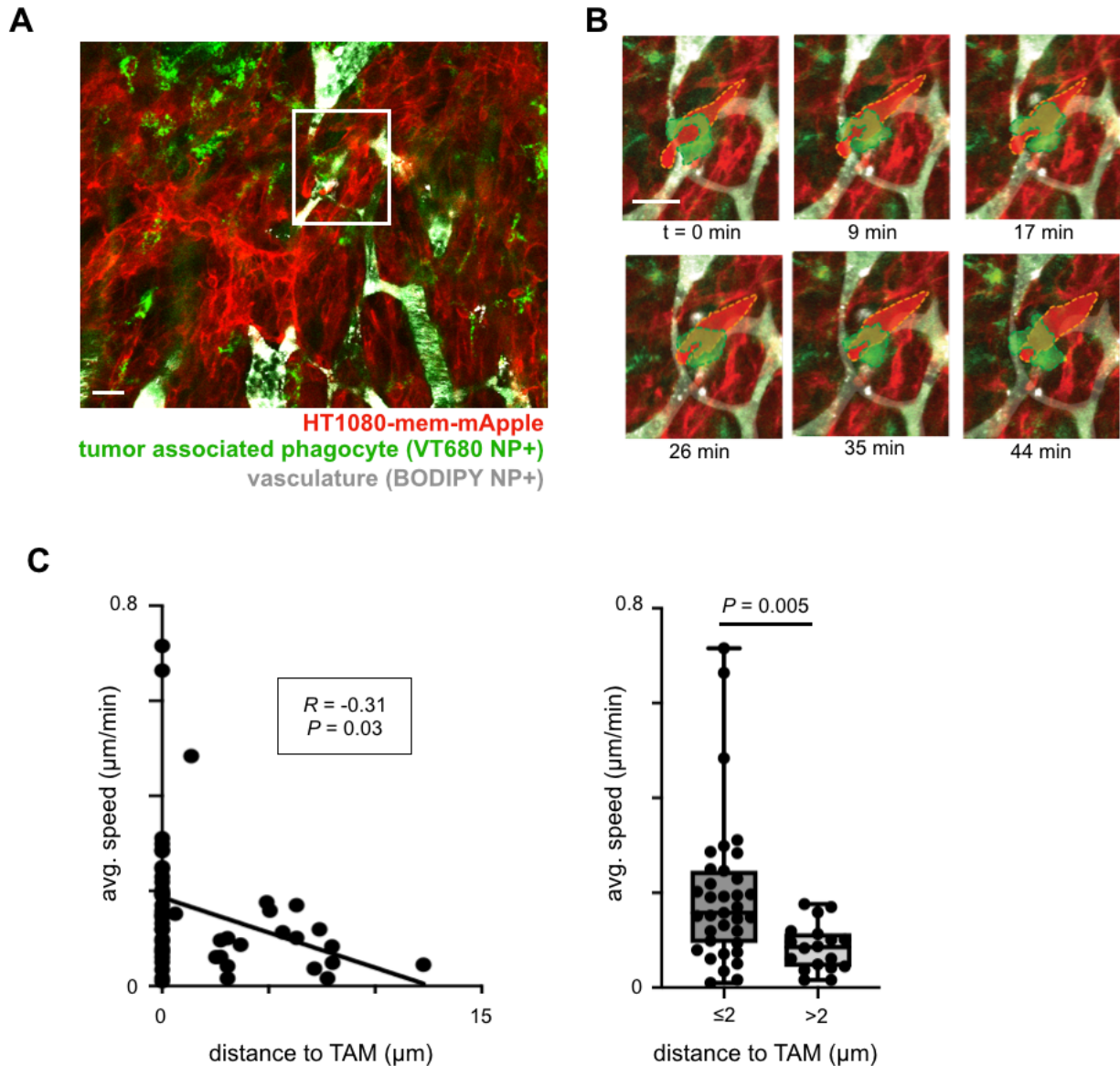
≤2   >2

distance to TAM (µm)

Figure 3-12: Measuring migration rata of HT1080 cells *in vivo*

(A-B) Example TAM-associated, migrating HT1080 cell is highlighted from a 20x field of view (A; scale bar = 20µm) and corresponding time-lapse (B; scale bar = 20µm). Cells have been shaded for visualization. (C) Migration speeds of individual HT1080 cells were compared with their nearest distance to TAMs, shown fit to a regression (left; Pearson's coefficient and two-tailed t-test) and binned by distance (right; *two-tailed t-test on cell level data; box plot as min, 25%tile, median, 75%tile, and max; E-F: n=55 cells across n=4 tumors).

3.2.6 Acute changes in MT dynamics precede cell shape changes.

Given their correlation under relatively equilibrated conditions, are MT dynamics simply a reflection of cell shape? We hypothesized that acute (<2 hr) changes in MT coherence would precede or predict subsequent changes in overall cell shape. As a proof-of-principle, we broadly targeted signaling using the first PI3K inhibitor to enter clinical trials, dactolisib (BEZ-235), which dually inhibits mTOR and pan-class PI3K signaling. EB3 dynamics were immediately imaged beginning 5 min post-treatment using HT1080 co-cultures. Dactolisib largely reversed the coherent MT phenotype induced by IL4-MΦ co-culture (**Figure 3-13A,B**). At early imaged time-points there was no visual evidence for cell death or apoptosis, nor did cellular circularity substantially change (**Figure 3-13C**). However, 24 hr post-treatment, co-cultured cells increased circularity (**Figure 3-13D**). This suggests that MΦ-enhanced MT coherence depends on mTOR/PI3K signaling pathways in a manner acutely decoupled from broader changes in cell shape, but in a more interrelated manner at longer timescales. To test effects of a selective perturbation, we used PCA to assess cell shape under co-culture conditions ± 24 hr anti-EGFR mAb treatment. IL4-MΦ co-culture elicited the strongest phenotype, reflected by a shift towards a positive PC1 score (**Figure 3-14A**) and correspondingly reduced cell circularity (**Figure 3-14A**), which was largely reversed upon EGFR inhibition. These results mirror the short term impact of anti-EGFR on MT dynamics (**Figure 3-5**), and further suggest linkage between acute MT dynamics and subsequent cell shape.
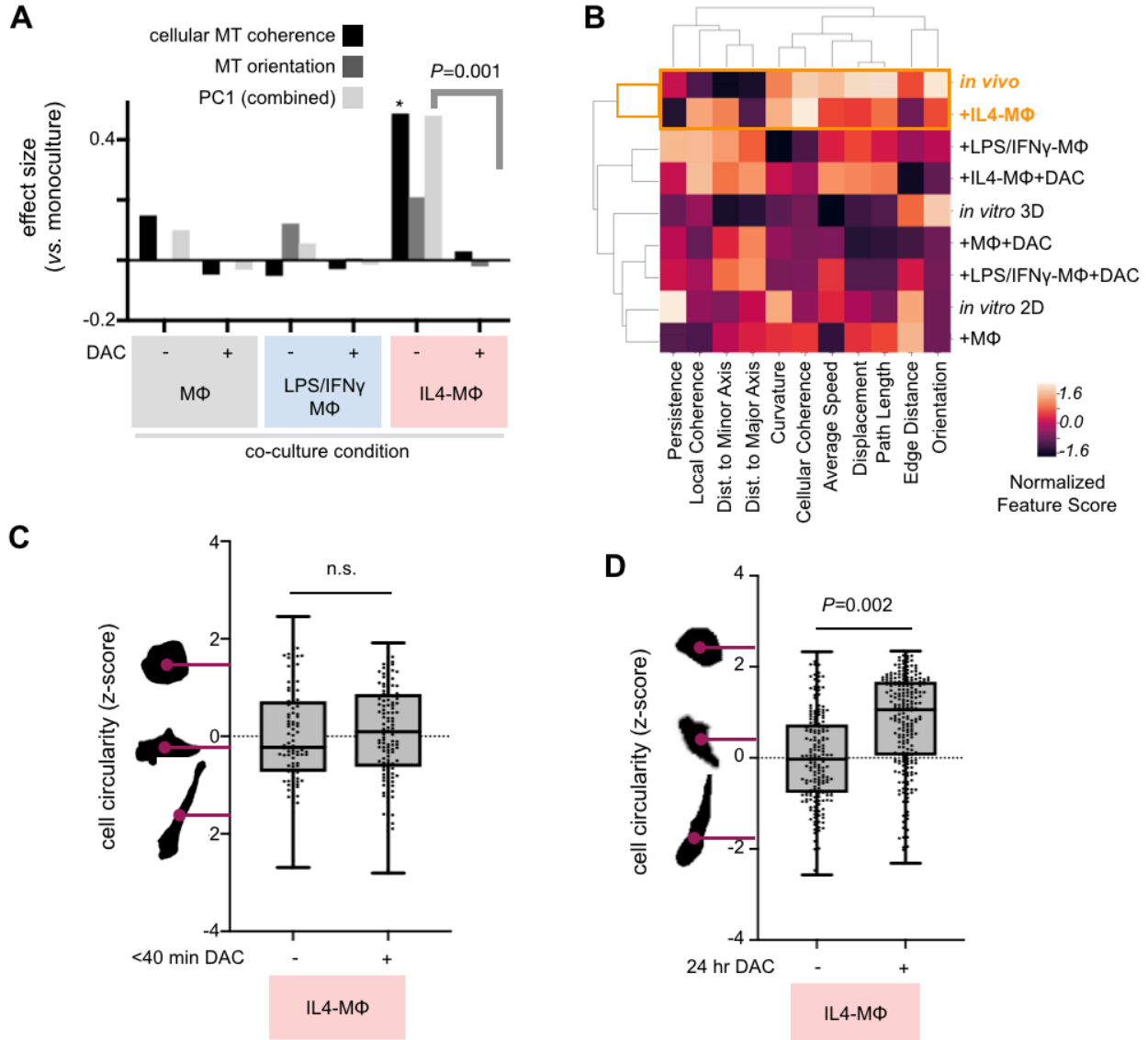
Figure 3-13. Drug-induced changes in MT dynamics precede changes in overall cell shape. (A) After 24 hr co-culture, HT1080 MT dynamics were imaged from 5 - 40 min following 10μM mTOR/pan-PI3K inhibitor dactolisib (DAC), and effect sizes were calculated as in Figure 3-3, comparing to untreated monoculture (*two-tailed permutation test; n=12,524 tracks from n=109 total cells). (B-D) Corresponding to A, MT tracks were clustered according to average values (B), and tumor cell shape quantified following DAC at < 40 min (C) or 24 hr (D) post-treatment (*two-tailed Mann-Whitney U test; C: n=223 cells, D: n=413 cells)
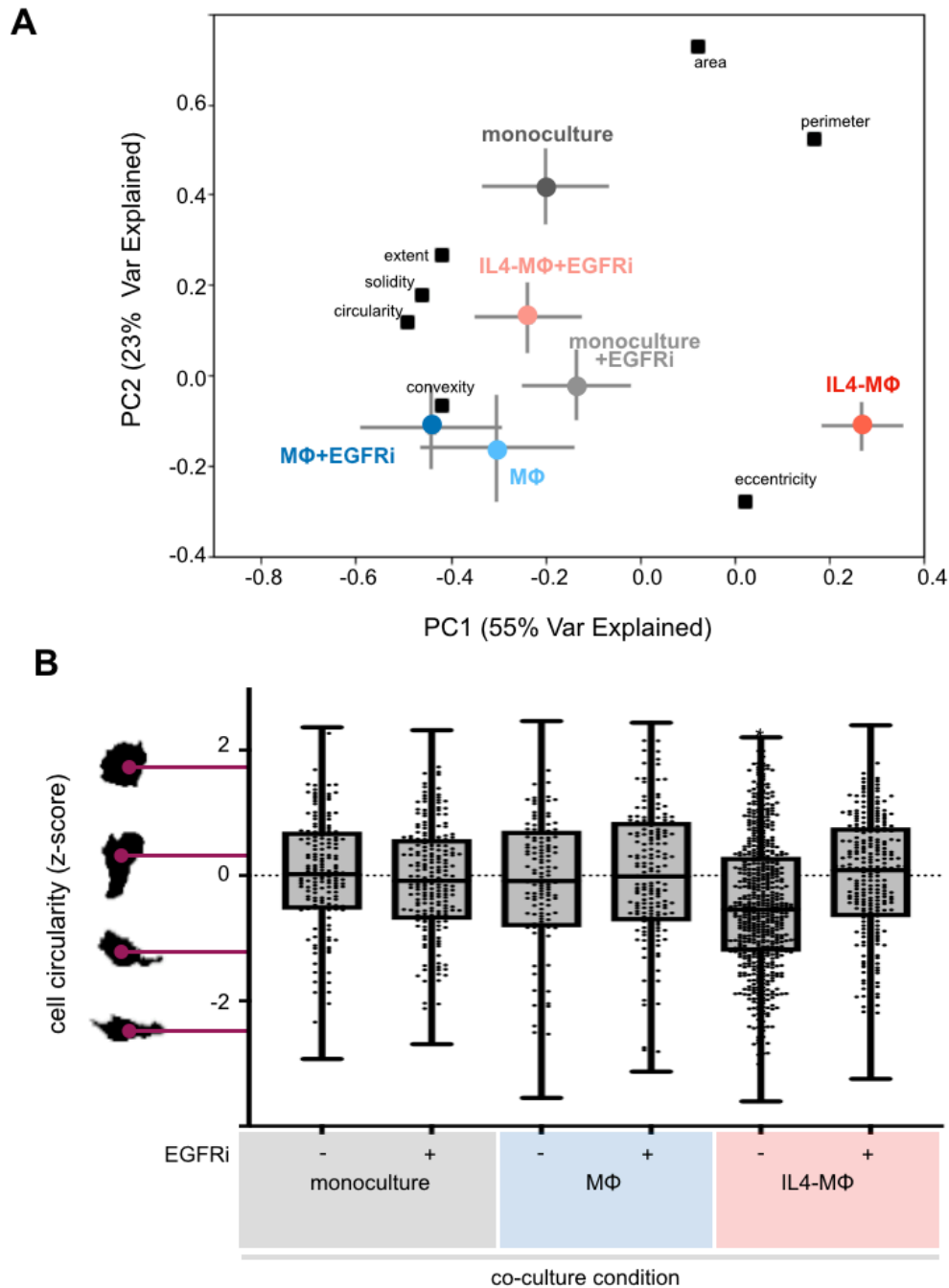
Figure 3-14. EGFR inhibitor treatment of MT dynamics and cell shape. HT1080 were

treated for 24-hr with anti-EGFR mAb (EGFRi), quantified for cell shape, and analyzed by PCA

(E; n=1,594 total cells; mean ± s.e.m.) and for cell circularity (*two-tailed t-test; n=1,678 cells;

bar denotes median). All box plots are min, 25%tile, median, 75%tile, and max

3.2.7 Targeting of IL10R regulates MΦ polarization and MT coherence

We hypothesized that *in vivo* MT coherence depended on the polarization state

of neighboring TAMs, and therefore imaged MT dynamics in tumor-bearing subjects

systemically treated with either an antibody blocking murine IL10R ligand engagement

(anti-IL10R mAb, referred to as aIL10R) or an isotype control. Reports implicate

autocrine IL10 in M2-like MΦ polarization[122,123], and indicate that PI3Kγ inhibition, which

elicited effects *in vitro* (**Figure 3-5**), reduces IL10 production in TAMs[118]. Furthermore,

we analyzed single-cell RNA sequencing data (scRNAseq) from patient biopsies in

multiple cancer-types (OVCA, melanoma, head and neck squamous cell carcinoma,

HNSCC), and found that IL10 signaling may occur at especially high levels in myeloid

cells including TAMs expressing both IL10 and its receptor components IL10RA (**Figure

3-15**) and IL10RB (see Methods).
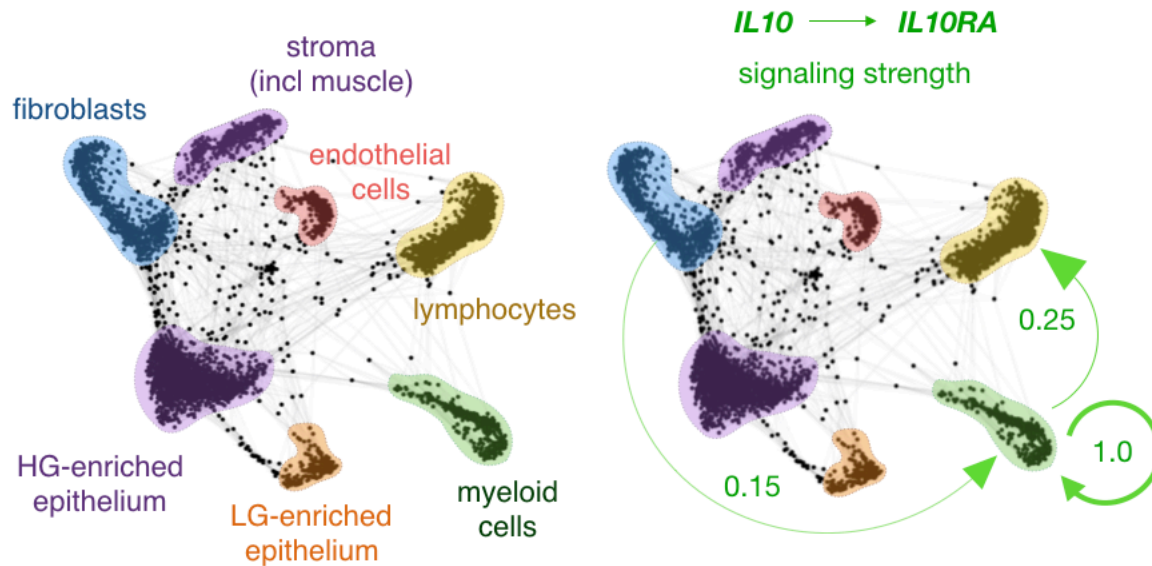
Rank	IL10 to IL10RA signaling (scRNAseq)		
	OVCA (n=9)	melanoma (n=19)	HNSCC (n=18)
1	**MΦ -> MΦ (1.0)**	**MΦ -> MΦ (1.0)**	MΦ -> DC (1.0)
2	MΦ -> lymph (0.2)	T-cell -> MΦ (0.7)	**MΦ -> MΦ (0.7)**
3	fibroblast -> MΦ (0.1)	MΦ -> T-cell (0.5)	T-cell -> DC (0.4)
4	MΦ -> tumor (0.01)	B-cell -> MΦ (0.5)	MΦ -> B-cell (0.4)

Figure 3-15. Infering IL10-IL10R interaction from scRNA-seq. (A) SPRING visualizes scRNAseq data by cell-type from 9 patient biopsies, most either high-grade (HG) or low-grade (LG) serous OVCA (n>2,900 total cells). Arrows and table report top values for ^{IL10xIL10RA} (fraction max) from published patient cohorts[124–126].
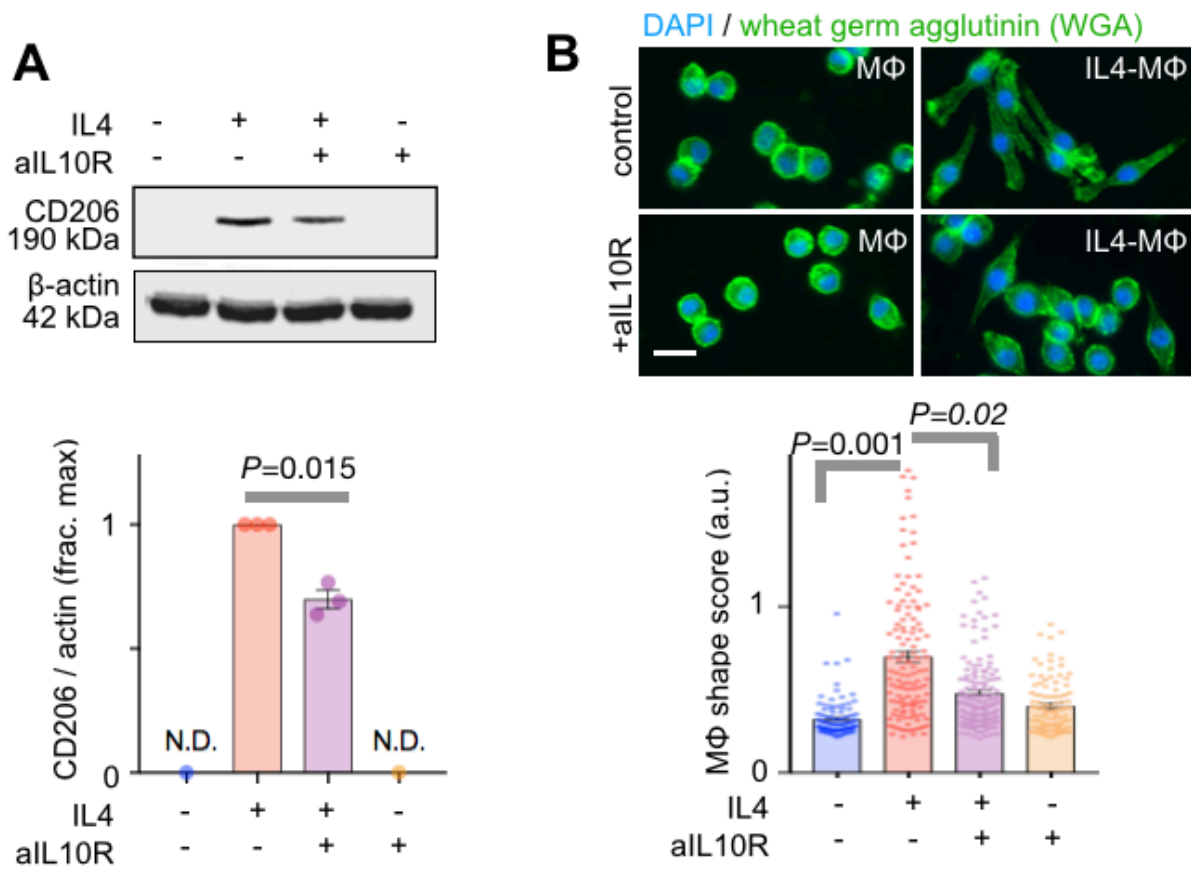
Figure 3-16. CD206 western blot and densitometry 24 hr following aIL10R in RAW264.7 (*two-tailed t-test; n=3; mean ± s.e.m.). (C) IL4-induced elongation in MΦ shape (calculated from combined shape features; scale bar = 10μm), was monitored 24 hr post-aIL10R (*two-tailed t-test; n=100 RAW264.7 cells per group with 4 groups; means ± s.e.m.).

Although IL10 is reported to promote M2-like MΦ polarization, we confirmed

aIL10R effects through two assays. We used the mannose receptor CD206/MRC1 as a

marker of M2-like MΦ polarization, and confirmed that aIL10R reduced its expression in

IL4-MΦ (**Figure 3-16A,C-9**). We also quantified MΦ cellular morphology to assess MΦ

polarization without relying on any single molecular marker (as similarly described[112]).

Consistent with past studies[112], round naïve MΦ became elongated upon IL4 treatment,

which partially reversed upon aIL10R treatment (**Figure 3-16B**), thus suggesting

aIL10R shifted MΦ polarization away from the M2-like phenotype.

In vitro, aIL10R blocked the effects of IL4-MΦ on MT coherence and orientation,

as reflected by a shift in the principal component describing the two features (**Figure 3-**

17A, calculated as in **Figure 3-4, C-8**), and also reversed the effects of IL4-MΦ on

tumor cell circularity (**Figure 3-17B**). Encouragingly, similar impacts of aIL10R on MT

dynamics and cell shape were also observed *in vivo* by IVM (**Figure 3-17C**;**3-18**

measured as in **Figure 3-3**). Overall, these data show how TAM polarization via IL10

locally shapes neighboring tumor cells to promote behaviors that distinguish *in vivo* MT

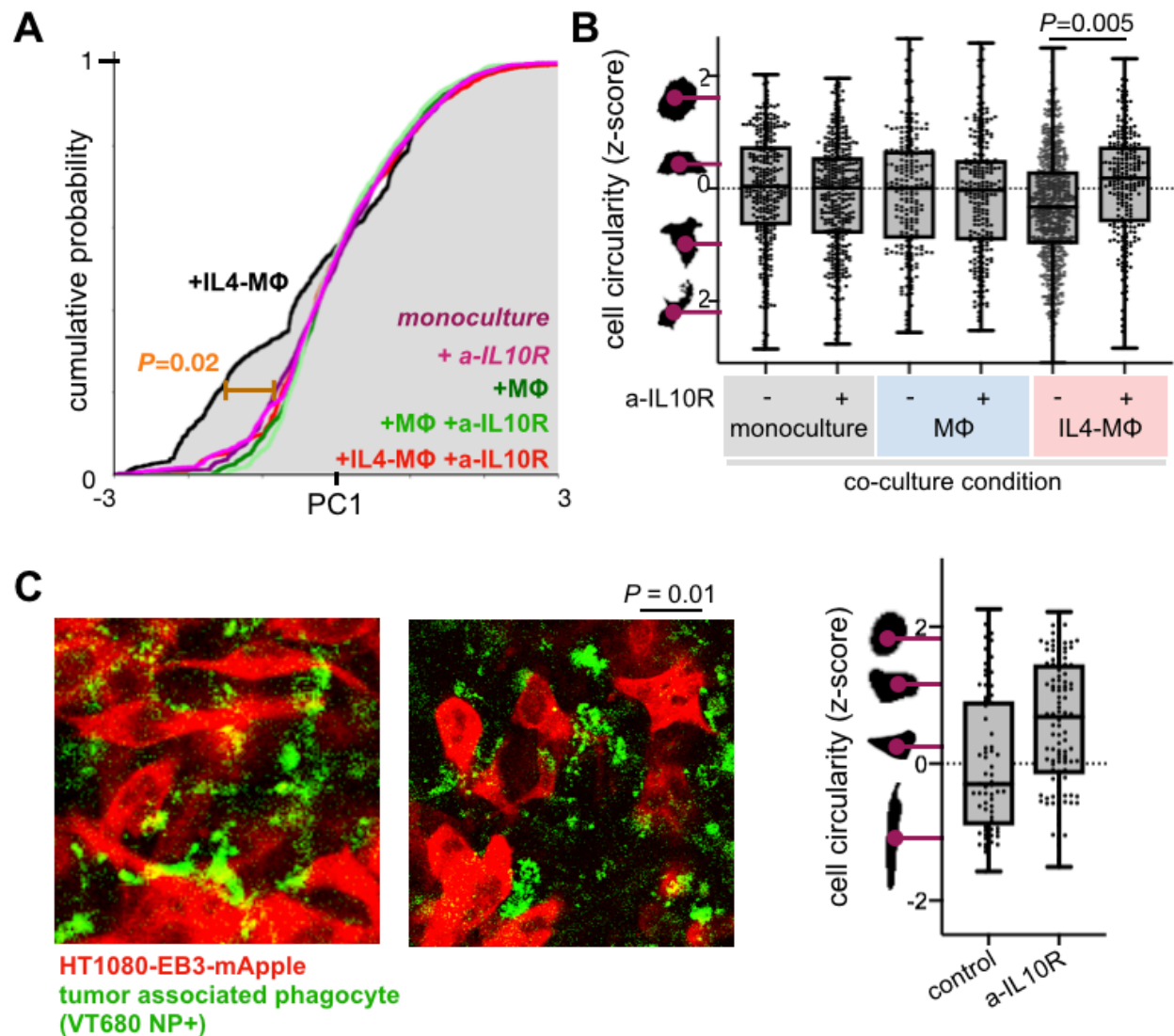dynamics from their *in vitro* counterparts (**Figure 3-19**).

Figure 3-17. Figure 9. Anti-IL10R antibody shifts MΦ polarization and reduces tumor cell MT coherence *in vitro and* in vivo.

(A-B) HT1080 MT dynamics (A) and cell circularity (B) were quantified as in Figure 3-3, 4 hr following treatment with aIL10R (A: *two-tailed permutation test; n=21,218 tracks from 99 total cells; B: *two-tailed t-test; n=1,964 total cells). (C) Representative IVM of TAM-proximal HT1080 following 48 hr treatment with aIL10R or the isotype control, in dorsal window chamber of nu/nu subjects (left), and corresponding HT1080 circularity (right; *two-tailed t-test on cell data; n=177 total cells; scale bar = 25μm).
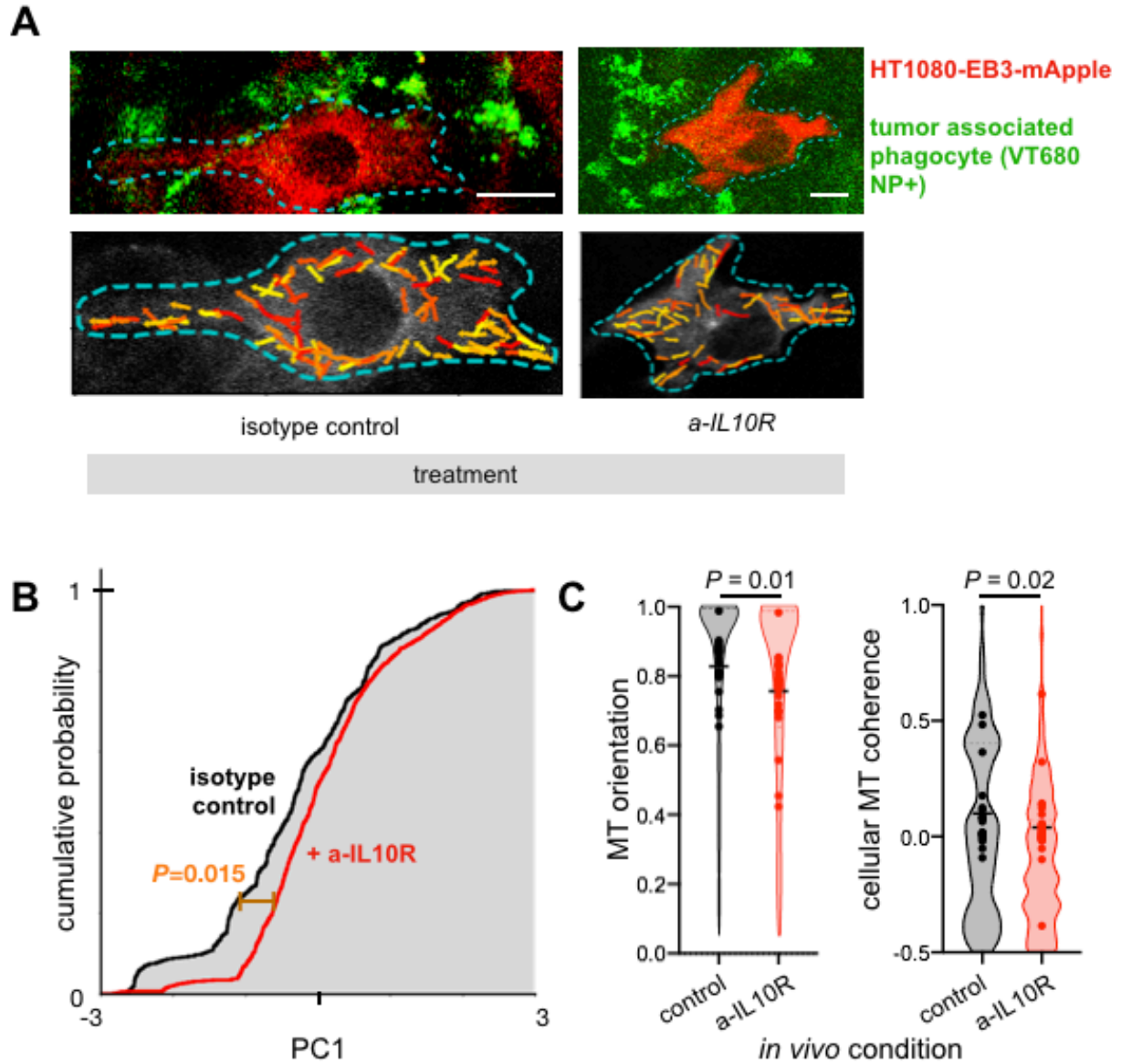
Figure 3-18. Analyzing effect of a-IL10R on MT dynamics in vivo. (A-C) MT dynamics were captured from Figure 3-17 and analyzed as in Figure 3-17A (*two-tailed permutation test; n=2,454 tracks and 51 total cells across n=8 tumors; bars denote mean; scale bar, 10µm). All box plots are min, 25%tile, median, 75%tile, and max.

3.3 Discussion

How do TAMs shape tumor MT dynamics? Our data implicate MΦ polarization influenced by IL4, aIL10R, and PI3Kγ-targeted IPI-549, which in turn likely affects MT dynamics through interdependent processes, including i) local signaling; ii) guidance through contact and spatial confinement; and iii) alignment through matrix remodeling and force generation. Altered transcription, cytoskeletal shape, and post-translational activities in polarized MΦ all affect these processes. Our *in vitro* data suggests contributions from the latter (MT dynamics decouple from gross cell shape changes within minutes in **Figure 3-13**), and broadly establishes a role for TAM polarization. Experiments with erlotinib (Tarceva) and the human EGFR-neutralizing mAb225 (non-humanized C225, cetuximab/Erbitux) suggest ligand-dependent EGFR signaling on cancer cells is required. EGFR ligands including heparin binding EGF (HB-EGF) are produced by both TAMs and cancer cells[113,127]. However, impacts of TAM polarization on ligand production are complex, and tumor EGFR signaling may likewise influence TAM polarization[128]. Thus, future work is needed to dissect EGFR-mediated tumor-TAM feedbacks, and more broadly, which other mechanisms are most important.
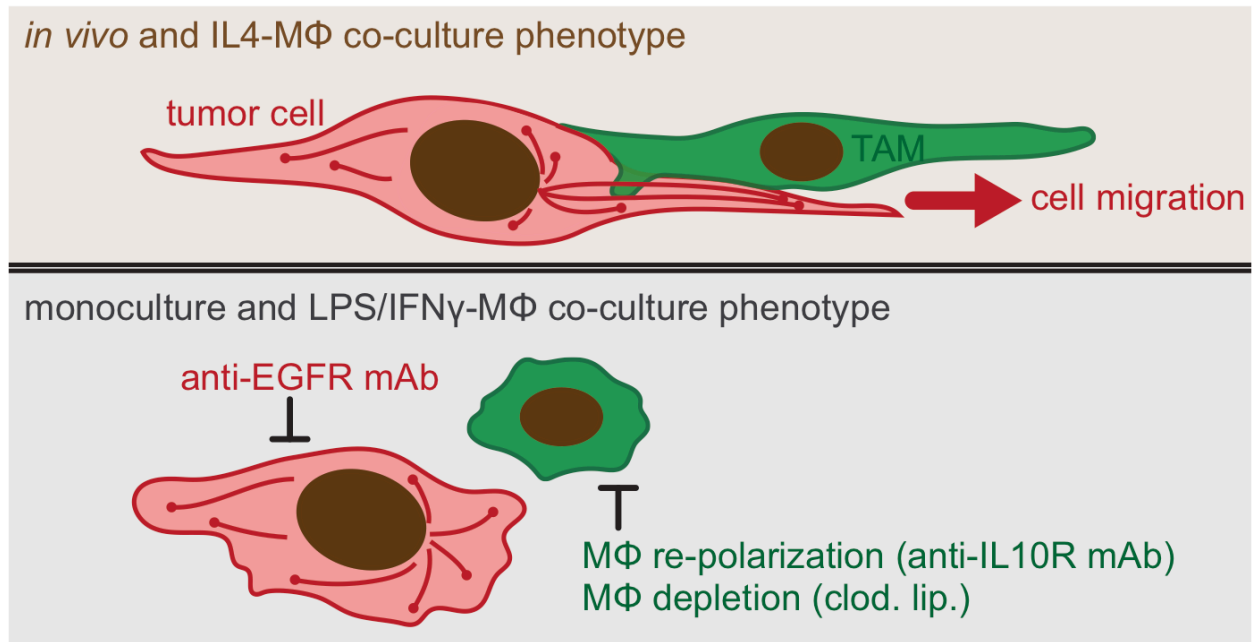
Figure 3-19 Summary schematic of TAM-dependent MT dynamics in cancer cells. (Top) Tumor cells in vivo exhibit high MT coherence and orientation along the major length axis of elongated, migrating cells. In vitro, cancer cells display this phenotype upon co-culture with M2-like IL4-MΦ. (Bottom) The IL4-MΦ co-culture phenotype depends on cell signaling pathways in both tumor cells and MΦ, including EGFR on tumor cells, and pathways known to influence MΦ polarization including PI3Kγ and IL10R. In vivo, treatment with an IL10R-neutralizing antibody reduces MT coherence and orientation in neighboring cancer cells.

Intriguingly, microglia and astrocytes bearing some relationship to TAMs (e.g. with respect to phagocytic activity) have been implicated in outgrowth and guidance of MT-rich axons [129]. Our results suggest that the polarization state of such cells — for instance as mediated by IL10R — could impact axon guidance, and IL10R signaling within astrocytes and microglia has been reported[130,131].

Technical limitations of our approach must be appropriately weighed. Variable MT density within individual cells makes it difficult to uniformly capture all MT dynamics, and therefore, our analysis was focused on a subpopulation of more centrally located MTs. Comets transiting in and out of the focal plane may not form continuous tracks. This occurs in cells grown in 2D and especially in 3D environments, and similar challenges arise in cell shape analysis. Strict tracking supports low false positive rates, but may decrease abilities to detect smaller and slower comets resulting in higher false negative rates, and different imaging conditions may bias the subpopulations of MTs being tracked (**Figure B-3**). We addressed many such issues through control experiments (for instance using synthetic imaging noise). Most importantly, this was addressed by testing hypotheses, including that TAM-repolarization via aIL10R may impact MT dynamics, through a comparison with matched control tumors or cells imaged under otherwise identical conditions. In this example, limitations and caveats of *in vivo* analysis applied equally across treatment groups, and MT dynamics still were observed to change in a manner consistent with the *in vitro* co-culture data.

Here we demonstrate how local microenvironmental signaling with TAMs can be as much of a distinguishing factor as the 3D extracellular matrix environment in affecting MT behavior *in vivo* compared to *in vitro*s. In fact, MΦ polarization is likely playing a

substantial role in shaping the extracellular matrix[132]. Our findings may be especially important for prodrug formulations of MT-targeted therapies based on nanoparticles (e.g. Genexol PM, used clinically in Korea) and antibody-drug conjugation (e.g. trastuzumab emtansine / Kadcyla), as these can accumulate in TAMs[91,133]. Future studies examining MTs and MT-targeted drugs *in vitro* might evaluate their action in the context of relevant populations including TAMs to better gauge true *in vivo* effects.

3.4 Methods and Materials

Materials (i.e., cell lines, cell culture equipment, etc) and methods (i.e., statistical analyses, imaging setup, etc) described in chapter 2 still apply for relevant experiments and computational analyses presented in this chapter. Additional material and methods are presented below.

3.4.1 Materials

Raw264.7 (Raw-MΦ) were originally from ATCC, and were cultured according to provider guidelines using DMEM Raw-MΦ and 10% HI FBS (Atlanta Biologicals), 100 IU mL^{-1} penicillin,100 µg mL^{-1} streptomycin (Invitrogen), with incubation at 37℃ and 5% CO2. Cells were routinely evaluated for mycoplasma contamination. Fluorescent-conjugated nanomaterials were synthesized [5]using PacificBlue ($\lambda_{ex}/\lambda_{em}$ = 401nm/452nm) or VT680XL ($\lambda_{ex}/\lambda_{em}$ = 665nm/688nm) as labeling fluorophores using previously described protocols[91,120]. Briefly, carboxymethylated polyglucose (550 mg, 2.3 mmol COOH) was dissolved in 6.2mL of MES buffer (50 mM), followed by addition of EDC (2.4 g, 12.5 mmol) and NHS (457.2 mg, 4.0 mmol). After 10 minutes at room temperature (RT), L-lysine (401.8 mg, 3.5 mmol) dissolved in 0.7 mL MES buffer (50 mM) was mixed with the solution for 5 hours at RT. The mixture was then slowly added to ethanol (30mL). After centrifugation (2500 × g) for three minutes, a white pellet formed. This pellet was then dissolved in Milli-Q H20, filtered using a 0.22 µm nylon syringe filter (Thermo Fisher), filtered again with a centrifugal filer (MWCO 8–10 kDa, Amicon Ultra), and finally lyophilized resulting in solid particles (Macrin-NP). The Macrin-NP (20 mg) was then conjugated to VT680XL by dissolving it in MES buffer (200

μL, 50 mM) followed by triethylamine (2 μL, 14.4 μmol) and VT680XL-NHS (0.5 mg in 215.5 μL DMF, 0.27 μmol). The solution was shaken at RT for 3h, purified using PD-10 columns with water, and filtered using centrifugal filters. This new solution was further diluted with MES buffer (200 μL, 50 mM, pH 6.0) and treated with Et3N (2 μL) and succinic anhydride (100 μL, stored in 750 mM in DMSO). After shaking this mixture overnight, VT680XL-Macrin was purified using PD-10 columns and centrifugal filters (MWCO 10 kDa, Amicon Ultra). Fluorescently labeled Macrin was analyzed and confirmed by a SEC, a Varian Cary 100 UV/vis spectrophotometer, and a Varian Cary Eclipse fluorescence spectrometer. Poly(D,L-lactic-co-glycolic acid) PLGA-BODIPY encapsulated Poly(D,L-lactic-co-glycolic acid)-b-poly(ethylene glycol) PLGA-PEG polymeric micelles and angioSPARK-680 were used as long-circulating vascular labeling agents. [91]).

The following antibodies and drugs (listed as target; source; calatog/clone#; concentration) were used for *in vitro* experiments only: Y-27632 (ROCK inhibitor; Tocris; Cat # 1254; 10μM); serabelisib (PI3Kα inhibitor; Selleck Chemicals; Cat # S8581; 0.5μM), AZD6482 (PI3kβ inhibitor; Select Chemicals; Cat # S1462; 0.5μM), AMG319 (PI3Kδ inhibitor; Selleck Chemicals; Cat # S7813; 0.5μM), IPI-549 (PI3Kγ inhibitor; Selleck Chemicals; Cat # S8330; 0.5μM), erlotinib (EGFR inhibitor; Selleck Chemicals; Cat # S7786; 5μM), UNC2025 (MERTK inhibitor; Selleck Chemicals; Cat # S7576; 100nM), R848 (TLR7/8 agonist; Selleck Chemicals; Cat # S8133; 1μM), human Integrin β1/CD29 Antibody (R&D Systems; Clone # P5D2; 10μg mL^{-1}), anti-CSF1R (BioXCell; Clone # AFS98 ;10μg mL^{-1}), and Axl Fc Chimera (R&D Systems; Cat# 154-AL-100; 10μg mL^{-1}). For measuring MT dynamics, each treatment was given 2-4 hours prior to

imaging. For measuring cell shape each treatment was given 24 hr. prior to imaging. The following antibodies were used for *in vitro* and in vivo experiments: InVivoPlus anti-mouse IL-10R (anti-IL-10R; BioXcell; Clone # 1B1.3A; 10µg mL^{-1}), InVivoMAb anti-human EGFR (anti-EGFR; BioXcell; Clone # 225; 10µg mL^{-1}), InVivoPlus rat IgG1 isotype control (IgG ctrl; BioXcell; Clone HRPN; 10µg mL^{-1}), InVivoMAb mouse IgG1 isotype control (IgG ctrl; BioXcell; Clone MOPC-21; 10µg mL^{-1}).

3.4.2 Intravital Microscopy additions

In instances (**Figure 3-18**), aIL10R or rat IgG isotope control was administered i.p. (200 µg in 100µL of PBS) to mice 5-7 days after HT1080-EB3-mApple injection and treated again after two days. Images were acquired after the first and second treatments. For visualizing TAMs, 24 hr. prior to the first day of imaging, mice were administered VT680-labelled polyglucose nanoparticles (Macrin)[120].

3.4.3 Disseminated OVCA imaging

5 million ES2 cells stably transduced to express the GFP-variant, mClover, were suspended in 200 µl PBS and i.p. injected into female nu/nu mice of 6-10 weeks age to establish a model of disseminated OVCA. Beginning 3 days after tumor inoculation, mice were treated i.p. with 150 µl clod-lip (5 mg mL^{-1}) or PBS control liposomes (Liposoma BV). 3 and 6 days after, 50 µl clod-lip or PBS-lip were again used. The following day, PacBlue-labelled polyglucose nanoparticles (Macrin) were administered i.v. and 24h later, mice were sacrificed for immediate ex vivo confocal imaging of tumor-

bearing organs. Macrin has been shown by flow cytometry and imaging to be >90%

selective for tumor associated macrophages in mice[120].

3.4.4 BMDM Culture

Murine bone marrow-derived MΦ (BMDMs) were isolated from the femurs and

tibias of 6-8 week old C57BL/6 mice. Marrow was flushed from the bones using 10mL

cold PBS flush via 21-gauge needle, cells were centrifuged for 5 min. at 300 x g, and

resuspended with PBS. Ammonium chloride (0.8%, NH_4Cl, StemCell Technologies) was

added at 4℃ for 5 minutes to lyse red blood cells. The mixture was centrifuged again for

4 min. at 300 x g. Cells were then plated on a 24 well plate with Iscove's Modified

Dulbecco's Medium (IMDM), 10% PBS + P/S, and 10ng mL^{-1} MCSF (Peprotech). The

medium was replaced every 2 days for 6 days. On day 7, MΦ were cultured in fresh

IMDM (MCSF-MΦ) or further polarized by replacing MCSF with 100 ng mL^{-1}

lipopolysaccharide and 50ng mL^{-1} interferon-gamma (LPS/IFNγ-MΦ), or 10 ng mL^{-1}

interleukin-4 (IL4-MΦ; Peprotech). After 24 hr. media was replaced with fresh IMDM,

10% PBS + P/S for 12 hr., MΦ treated 8 hr. with 10 nmol Alexa647-labeled Macrin, and

then treated with fresh IMDM.

3.4.5 BMDM and Tumor Cell co-culture

Immediately following the steps outlined aboveen, approximately 6,500 HT1080-

mApple cells or 10,000 ES2-EB3-mApple cells were seeded into wells already

containing polarized MΦ, where they were then co-cultured for approximately 48 hours

in a 96-well plate (Ibidi). The co-cultures and matched monocultures were all grown in

IMDM, and then fixed using a 4% PFA + PBS for 20 min. and imaged. For conditioned

media experiments, approximately 6,500 tumor cells were seeded per well into a

separate 96-well plate. The media from the MΦ culture was transferred into the

separate well plate containing newly seeded tumor cells. Tumor cells were grown for 48

hr., followed by fixing and imaging as above. *In vitro* images for cell shape quantification

and ES2 EB3 imaging were acquired using a modified Olympus BX63 inverted

microscopy system with environmental chamber and robotic stage.

3.4.6 RAW264.7 and Tumor Cell Culture

Approximately 500 RAW264.7 were seeded in a 96 well plate and treated

with/without 20 ng mL^{-1} IL-4 (24 hr.), followed by VT-680 labelled Macrin (24 hr.). On

day 3, approximately 1000 HT1080-EB3-mApple cells or ES2-EB3-mApple cells were

seeded onto the plate. Cells were co-cultured for 24 hr. followed by drug treatment

lasting 2-4 hours or 24 hr. (except aIL10R, which was treated for 48 hours prior to

imaging; **Figure 3-17**). For ES2-EB3 MT dynamics drug screen, RAW264.7 were

polarized and labelled with Macrin prior to seeded on a 10mL petri dish, and were

seeded simultaneously with tumor cells.

3.4.7 Western Blot for studying MΦ Polarization

RAW264.7 were cultured in 6-well plates and treated with +/- 20ng mL^{-1} IL-4, +/-

10µg mL^{-1} aIL10R, and/or +/- 10µg mL^{-1} Rat IgG isotope control, resulting in a total 4

conditions (+IL-4 +aIL10R, +IL-4 +IgG ,+aIL10R, +IgG). Cell lysates were extracted

from each well with RIPA buffer containing protease inhibitor and PMSF. 30 µg of total

protein was resolved on 4–12% NuPAGE electrophoresis gels (Invitrogen) and then transferred onto nitrocellulose membranes (Invitrogen). The membranes were incubated with the following antibodies at the corresponding dilution factors: rabbit anti-CD206 antibody (Abcam, polyclonal) at 1:1000 or mouse anti-β actin antibody (Cell Signaling Technology, clone#8H10D10) at 1:2000. This was followed by incubation with the appropriate secondary antibodies conjugated to horseradish peroxidase (Cell Signaling Technology). The immunoreactive bands were detected with ECL Chemiluminescent substrates (Thermo). To quantify western blot images, densitometry analysis was performed using ImageJ, and the densitometry value for each protein was normalized to β-actin before further being normalized.

3.4.8 PCA analysis of select MT features, Clustergram, and K-L Divergence

PCA was performed using the python scikit-learn package. Two features, track orientation and track cellular coherence, were used, such that PC1 is a linear combination of the track orientation and cellular coherence features. To examine the differences between two track features: cellular coherence and orientation, across all nine HT1080 cell populations or conditions, K-L divergence was computed between the PC1 distributions of each condition (**Figure C-2**). Clustergram analysis involved finding the average MT track feature value for each HT1080 tumor cell population. This was accomplished by first removing all MT tracks that had feature values greater than three SD's away for any of the plotted features of interest, followed by averaging track feature values for each cell population/condition. All columns were normalized (0 mean, 1 SD).

The average values were then clustered using hierarchal clustering (method=complete, metric=euclidean) via the clustergram function available in the python seaborn package.

3.4.9 Contact Analysis (Figure 3-20)

From the MΦ mask, a distance transform image (where each pixel value is the distance to the nearest MΦ) was constructed. The minimum distance between tumor cell and MΦ was computed using the the distance transform and the tumor cell mask. Tumor cells were binned according to low, medium, or high unnormalized circularity measures (**Figure 3-8B**: low=0,0.4), medium=0.4,0.7), high=[0.7,1), Figure 3-9B: low=[0,0.7), high=[0.7,0.8), medium=[0.8,1)). Computing significance scores over individual cells resulting in extremely low significance values, and therefore, significance was calculated using cell averages from image replicates for in vitro cells and tumors for vivo cells in all cell shape analyses unless explicitly stated otherwise. To calculate p-values, averages across batches were calculated and outlier less $Q1-1.5*IQR$(inter quartile range) or greater than $Q3+1.5*IQR$ were excluded from the calculations. A two-sided t-test or nonparametric wilcoxon rank sum test was then applied to obtain a final p-value.
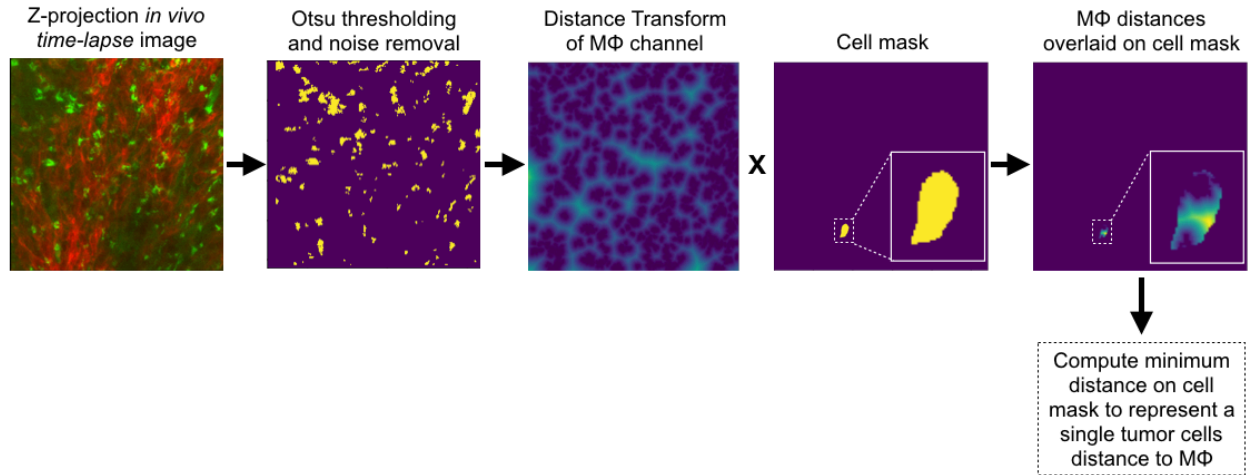
Figure 3-20. A) Image processing pipeline for how the distance of nearest macrophage was calculated for HT1080 cells (corresponding to Figure 3-8,3-9).

3.4.10 Cell Migration Analysis

HT1080-mem-mApple cells were imaged by IVM as described above with the EB3-mApple model and in a prior report[91]. Briefly, to track cell migration, confocal z-stacks were acquired roughly every 5-10 minutes at multiple tumor locations for approximately 2 hr as reported[91]. Tumor associated phagocytes and microvasculature were labeled by co-administration of a dextran-coated nanoparticle known to be highly phagocytosed by perivascular macrophages (ferumoxytol-VT680XL), along with a more slowly extravasating PLGA-PEG polymeric nanoparticle[91]l. Ferumoxytol-VT680XL was intravenously co-administered (750µg [44]) with PLGA-PEG nanoparticle (100nM [BODIPY]) immediately prior to time-lapse imaging. 50 cells were identified, and a cell mask was created for each cell. From the cell mask, morphological features of eccentricity and circularity were calculated using custom python scripts. To calculate migration rates for each of these 50 tumor cells, the center of the cell was approximated and traced over a minimum of 4 frames.

3.4.11 TAM and Vasculature Association Analysis

The association between HT1080-mem-mApple cells and vasculature *in vivo* (Figure 3C) was determined by first generating a mask image representing the tumor vasculature via Otsu thresholding on the original images labelled with either AngioSPARK680 or PLGA-PEG polymeric nanoparticle. Individual cell masks were manually identified. If any region of the tumor cell overlapped with the vasculature mask, then the TC is marked as contacting vasculature. The same process was applied to macrophage images to study macrophage-tumor cell association.

3.4.12 Monoculture and IL4-MΦ Coculture Effect Size/Significance Analysis

The effect sizes between HT1080-EB3-mApple and ES2-EB3-mApple cells grown in monoculture and in coculture with IL4 polarized MΦ was determined for all 14 MT features. The effect sizes were computed separately for each experiment run (2 for ES2-EB3-mApple) and (4 for HT1080-EB3-mApple) to account for potential batch effects, and pooled together. Some runs had slightly varying conditions described as follows: ES2-EB3-mApple runs 1 and 2: untreated monoculture vs IL4-polarized BMDM MΦ co-culture. For HT1080-EB3-mApple cells: (1) untreated monoculture vs IL4-polarized BMDM MΦ co-culture, (runs 2-4) monoculture and IL4-polarized Raw MΦ; both treated with either Rat IgG isotope control (run 2), mouse IgG isotope control (run 3), or DMSO control (run 4). Effect sizes for each run were calculated using Cohen's D Statistic (see Methods: MT tracking and feature extraction) and averaged across multiple runs. To generate violin plots (**Figure 3-2D**), ES2-EB3-mApple tracks were combined from both runs (top) and HT1080-EB3-mApple tracks were combined for runs

2-4 (bottom). To calculate the significance of each feature between monoculture and coculture conditions, tracks from each batch were individually normalized (mean=0, st. dev.=1). An equal number of cells was randomly sampled (33 HT1080 cells and 33 ES2 cells), and a maximum of 25 tracks from each cell was subsampled. 1000 permutations were then performed for two pooled MT track populations (+/- MΦ coculture) such that cell labels for MT tracks were shuffled between the cell populations being compared. A naïve wilcoxon rank sum test between pairs of cell populations was applied to determine the permutation p-value, for each MT feature. For each feature, the number of permutations with a p-value less than the p-value of the true distribution was divided by the total number of permutations to obtain a permutation based p-value. For multiple hypothesis testing correction (12 different features), a benjamini-hochberg correction (Q(fdr)=0.05) from the python statsmodels package was used to generate the final p-value.

3.4.13 Single-cell RNA sequencing (scRNAseq) analysis

Analysis of ligand-receptor interaction from scRNAseq data was performed based on prior methods[20]. Briefly, scRNAseq data from biopsied patients was pooled across individuals. Cell-type identities (tumor, T-cell, myeloid cell, etc.) were provided from the published data annotations, and the average expression of IL10 was multiplied by the average expression of IL10RA or IL10RB for all such cell-type populations. Values were normalized to the maximum observed product (scaled to a maximum of 1.0). SPRING software (accessed Dec 2019 - Jan 2020) was used for dimensionality reduction to visualize and categorize key cell populations[134]. For OVCA, scRNAseq data

(GSE118828 https://www.ncbi.nlm.nih.gov/geo/query/acc.cgi?acc=GSE118828) was

pooled across samples from 9 biopsied subjects, including 5 with high grade serous

OVCA, 2 with low grade serous OVCA, 1 with metastatic peritoneal disease, and 1 with

a benign lesion[126]. Other analyzed data included scRNAseq data from 19 melanoma

patients (GSE72056

https://www.ncbi.nlm.nih.gov/geo/query/acc.cgi?acc=GSE72056)[124] and 18 patients with

head and neck squamous cell carcinoma (HNSCC; GSE103322

https://www.ncbi.nlm.nih.gov/geo/query/acc.cgi?acc=GSE103322)[125]. In all three

datasets, IL10 to IL10RB signaling was highest for homotypic MΦ (MΦ to MΦ signaling)

compared to all other cell-type pairings.

Chapter 4 Inferring Ligand receptor communication dynamics and signaling patterns from single-cell RNA sequencing datasets.

The material in this chapter is unpublished and currently under preparation.

Abstract:

Biological processes such as homeostasis, development, disease progression are dynamic processes regulated by complex interactions between various cell types. Single-cell RNA sequencing has enabled the discovery of new cell types and quantification of receptors and their cognate ligands in mammalian tissues. However, it has been challenging to translate static cell-cell communication into a more comprehensive understanding of how these networks dynamically operate. To address this problem, we developed POLARIS, a single-cell RNA-seq based computational method to model how ligand and receptor interactions change during a biological process of interest. POLARIS combines ligand-receptor interaction analysis with inferred dynamical information obtained from single-cell trajectory methods. We apply POLARIS to examine two different biological processes: the epithelial to mesenchymal transition (EMT) and colorectal cancer progression. We recover important ligand-receptor mediated regulatory signaling patterns present during these biological processes.

4.1 Introduction

Cells communicate with one another to change their internal state and drive critical cellular processes such as differentiation, proliferation, and reprogramming. When cell communication is altered or dysfunctional, diseases such as cancer ensue. Cellular crosstalk mechanisms vary, from mechanical cues between neighboring cells to endocrine signaling across organs. Single-cell RNA sequencing (scRNA-seq) technologies provide a detailed view of a tissue's cellular composition in both normal and disease states. In addition to revealing new cell types and tissue heterogeneity, scRNA-seq data analysis has recently enabled the exploration of an essential class of intercellular communication, ligand-receptor (LR) interactions. In such interactions, a small protein, or ligand, is secreted from one cell and binds to a surface receptor on the same cell (autocrine) or different cell (paracrine).

Because LR interactions are targeted by numerous therapeutics, identifying potential interactions contributing to the disease progression is fundamental to improving clinical outcomes[20]. In cancer treatment, immunotherapies such as Pembrolizumab and Ipilimumab target PD1- PDL1 and CD28-CTLA interactions, respectively[135]. Screening scRNA-seq datasets for LR interactions across different cell types in a tumor has also revealed crosstalk mechanisms by which the tumor microenvironment promotes cancer progression. Such analyses have also explored other diseases and potential mediators in organ development and homeostasis[9].

As detailed in chapter 1, a typical computational pipeline for quantifying LR interactions from scRNA-seq data relies on a predefined list of validated LR pairs[9]. For each known LR pair, interaction strength is measured between different single-cell

populations based on a scoring function. The scoring function takes the ligand and receptor gene expression as inputs and outputs an interaction score. Combining the interaction scores from multiple LR pairs can result in a global communication network between cell types within a tissue sample of interest. Numerous publicly available computational tool kits, including CellPhoneDB[23,136], CellChat[24], ICELLNET[25], and RNAMagnet[15], provide a robust characterization of LR interactions from scRNA-seq and bulk RNA-seq measurements. Each method differs in the scoring function employed, significance testing, type of interaction measured, and incorporation of additional information such as downstream signaling pathways[23].

Because scRNA-seq experiments capture gene expression at a single time point, the computational approaches discussed above present only the structure of a communication network within a tissue. Understanding how cellular communication networks operate requires information on how intercellular interactions change over time. Recently developed single-cell trajectory analysis methods can infer dynamic information from scRNA-seq datasets[137–139]. Such methods arrange single-cells into trajectories based on gradual changes in gene expression, with the underlying assumption that a continuum of cell states is observed at any given time. Each cell can be assigned a pseudotime, a numerical value indicating that cell's location along a trajectory or progression for the biological process of interest. We hypothesize that modeling LR interactions over pseudotime can provide insight into important regulatory programs driving dynamic biological processes.

Here we detail a novel approach to analyze intercellular communication from scRNA-seq data, called POLARIS. Rather than identifying significant LR interactions

between cell types, POLARIS aims to understand how interactions between and within cell types change and modulate cell state, disease progression, and/or tissue homeostasis. POLARIS models intercellular communication in the form of ligand-receptor interactions as a function of pseudotime. We first identify cellular trajectories indicating the biological process of interest and assign a pseudotime value to each cell. Second, we apply a curated list of LR interactions, and model how each LR pair changes over pseudotime. And finally, clustering and significance testing reveal enriched interactions and potential regulatory circuits. Inferring changes in LR interactions along cell trajectories reveals how such interactions may be affecting cell fate.

By applying POLARIS on publicly available scRNA-seq datasets, we examine two different biological processes, the epithelial to mesenchymal transition (EMT) and colorectal cancer progression. We demonstrate that POLARIS recovers enriched LR interactions and provides insight into feedback/feedforward signaling behind these biological processes.

4.2 Results

4.2.1 Modeling Cell-Cell Communication Over Pseudotime

POLARIS relies on a series of computational steps to understand the relationship between intercellular communication and cell fate in a biological process of interest (**Figure 4-1**). First, pseudotemporal ordering of single cells is determined based on gene expression data. Numerous single-cell trajectory analysis software, including Monocle 2, STREAM, and Wishbone, are publically available to calculate the pseudotime of individual cells and detect cell lineages. The current implementation of POLARIS aims to capture how cells along different points in development signal to one another and has functionality for:

1. Single lineages (step 1A).

2. Multiple differentiated lineages arising from a common source (step 1B).

3. Independent lineages arising from different sources (step 1C).

Second, POLARIS models changes in intercellular interactions, particularly LR interactions, over pseudotime (Step 2). The analyses presented in this manuscript used a reference list of approximately 1,200 known, literature-supported, and manually curated ligand-receptor interactions, including chemokine, cytokine, cell-extracellular matrix, receptor tyrosine kinases interactions. For each LR pair, the ligand expression (pink curve) and cognate receptor expression (blue curve) are quantified along two cell lineages.

In a typical LR analysis, single cells are assigned to a discrete number of cell types and the average ligand and receptor expression is used to compute an interaction score. Because cell states are not defined along continuous lineage and scRNA-seq

datasets have a high dropout rate, sliding window was used to construct a curve

representing the proportion of cells expressing a ligand or receptor (gene count greater

0) as a function of pseudotime. After computing LR expression profiles, POLARIS then

constructs an interaction topology map for each LR pair, denoted as a LR topology.

Briefly, LR topologies are constructed via the tensor product of two functions: the ligand

expression ($l(t)$) and receptor expression ($r(t)$). Various signaling patterns display

different topologies. For example, a LR interaction involved in a positive feedback

mechanism where cells further along the lineage signal to cells earlier will generate a

different pattern then LR pairs involved in feedforward or autocrine signaling.

To decipher, quantify, and visualize these LR topologies, POLARIS utilizes

various supervised and unsupervised strategies (step 3). Unsupervised learning

methods such as PCA and clustering reveal LR pairs that demonstrate similar signaling

patterns along cell lineages of interest. Supervised learning methods employed by

POLARIS focus on predetermined or user-crafted regulatory patterns and quantifies the

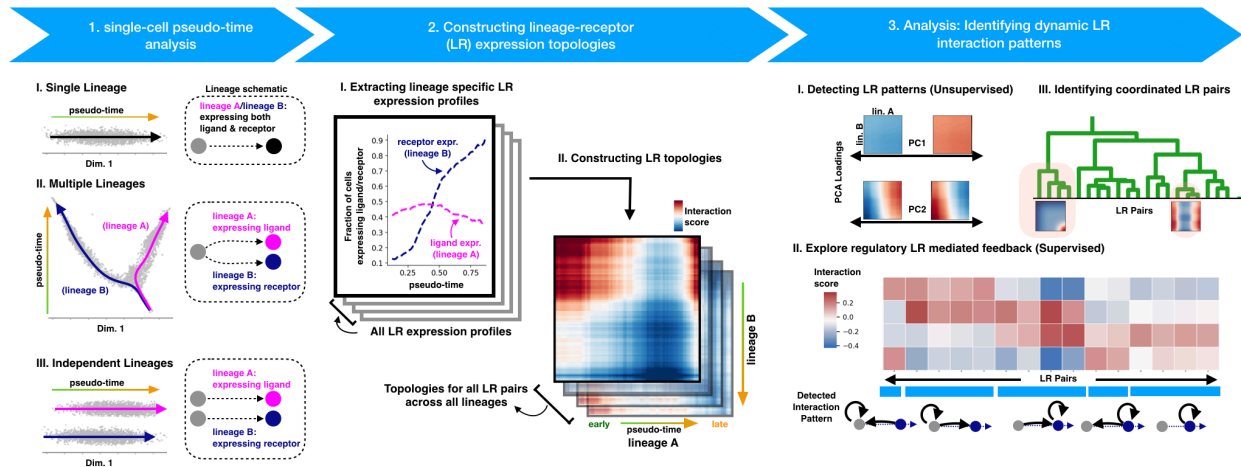contribution of these patterns to the observed LR topology.

Figure 4-1: Overview of POLARIS. (Step 1) By applying single-cell trajectory methods, pseudotime values are computed for each cell. Interactions occurring within a single lineage (top), multiple lineages (middle), or independent lineages (bottom). (Step 2) The ligand expression profile along lineage A and the receptor expression profile along lineage B represent the fraction of cells expressing a particular ligand or receptor as a function of pseudotime. An LR topology is constructed for each LR expression profile. Each LR topology capture interaction patterns between two lineages for a particular LR pair. (Step 3) Applying computational methods including PCA, clustering, and supervised clustering to the set of LR topologies can reveal unique regulatory programs or interaction patterns for a particular LR pair.

4.2.2 POLARIS captures important signaling patterns in EMT signaling

The epithelial to mesenchymal transition is fundamental to several biological processes including cancer metastasis, embryogenesis, and organ development. During this transition, epithelial cells which originally have strong cell adhesion, begin to display a mesenchymal cell phenotype consisting of strong migratory capacity, ability to

invade the extracellular matrix (ECM), and dissolution of cell-cell junctions. To demonstrate the applicability of POLARIS to study the EMT transition, we re-examined a scRNA-seq dataset of 3133 cells from *Cook et al*. (2020)[140]. This dataset was generated by treating cultured A549 human lung-cancer cells with the EMT inducing factor, TGFB1. Cells were either left untreated or treated for 8 hrs, 1 day, 3 days, and 7days before before being sequenced to construct a gene expression matrix. Each cell was computationally assigned a pseudotime by the study authors which correlated with EMT progression and used as inputs for POLARIS (**Figure 4-2A**).
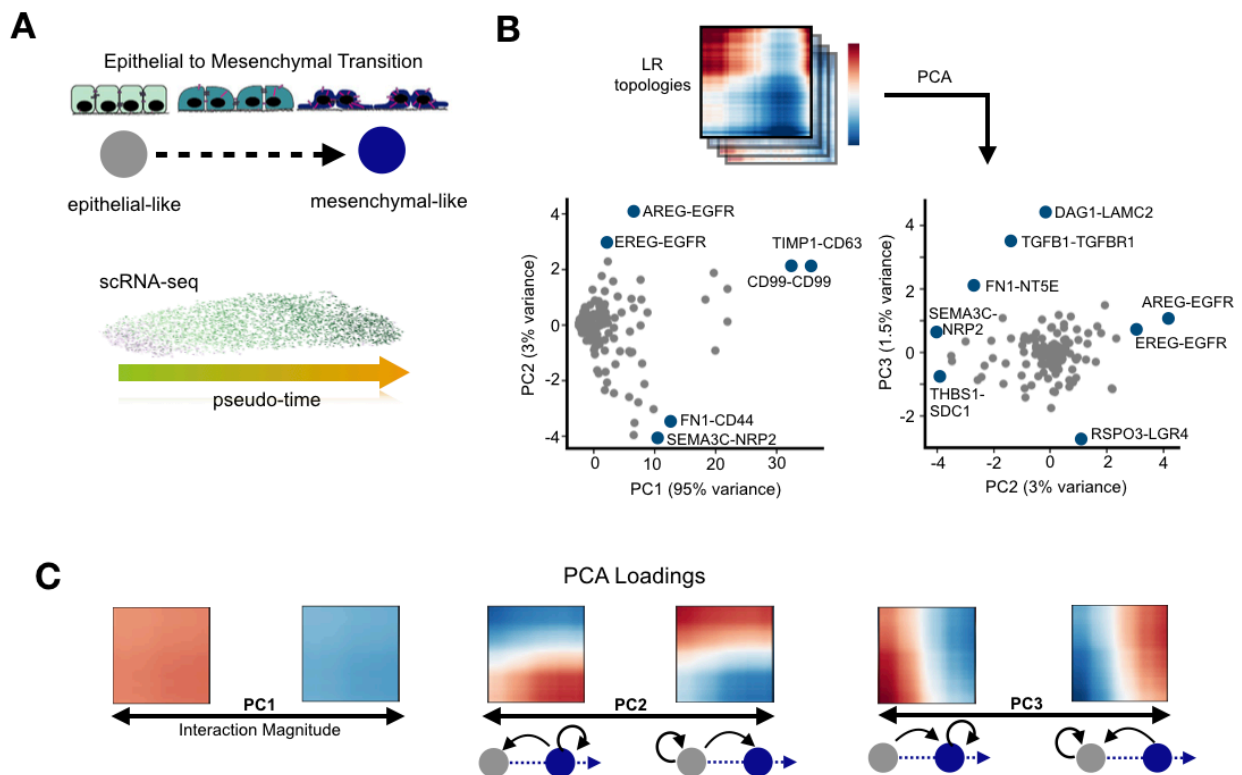

Figure 4-2: PCA analysis reveals distinct LR interaction patterns in EMT. (A) single cells are arranged by pseudotime indicating their current state along the epithelial to mesenchymal transition. (B) PCA analysis was performed on the set of LR topologies. (C) Visualization of PCA loadings for the first three principal components.

For each of the 1580 LR interactions a topology map representing the strength interaction for cells at different stages of EMT was constructed. Using POLARIS, we applied PCA to the set of computed topologies as a dimensionality reduction method to systematically identify different regulatory patterns (**Figure 4-2B**). A closer look at the PCA loadings reveal that while the first principal component (PC1) captures the overall interaction magnitude, the second (PC2) and third principal components (PC3) capture unique interaction patterns (**Figure 4-2C**). LR pairs with a negative PC2 value involve mesenchymal-like cells - further along the EMT axis - expressing genes encoding for ligands such as SEMA3C and FN1 which bind to epithelial-like cells - at the beginning of the EMT axis, suggesting a potential feedback mechanism. At the opposite end of the spectrum, cells with a higher PC2 value involve epithelial-like cells signaling to mesenchymal like cells. Positive and negative PC3 scores also indicate a separate set of interaction patterns.

While PCA can help in resolving the predominant patterns governing a biological process of interest, in this case EMT, we also wanted to explore how much specific interaction patterns contribute to the observed behavior of each LR pair. For example, how significant is an autocrine interaction between mesenchymal-like cells for a specific LR pair. To perform this analyses, we handcrafted five distinct topologies: (1) mesenchymal-like cells signaling to each other (autocrine interaction between cells later in pseudotime), (2) mesenchymal-like cells signaling to receptors on epithelial-like cells (paracrine interaction between cells later and earlier in pseudotime), (3) intermediary cells signaling to each other, (4) epithelial-like cells signaling to mesenchymal like cells

(paracrine interaction between cells later and earlier in pseudotime), and (5) epithelial-like cells signaling to each other (autocrine interaction between cells early in pseudotime)(**Figure 4-3**). POLARIS applies a convolution operation between the handcrafted topology and each experimentally determined LR topology. The results of this operation yields a quantifiable result indicating the similarity between the two topologies, and thereby the contribution of a specific signaling pattern to the observed interaction of the LR pair of interest.
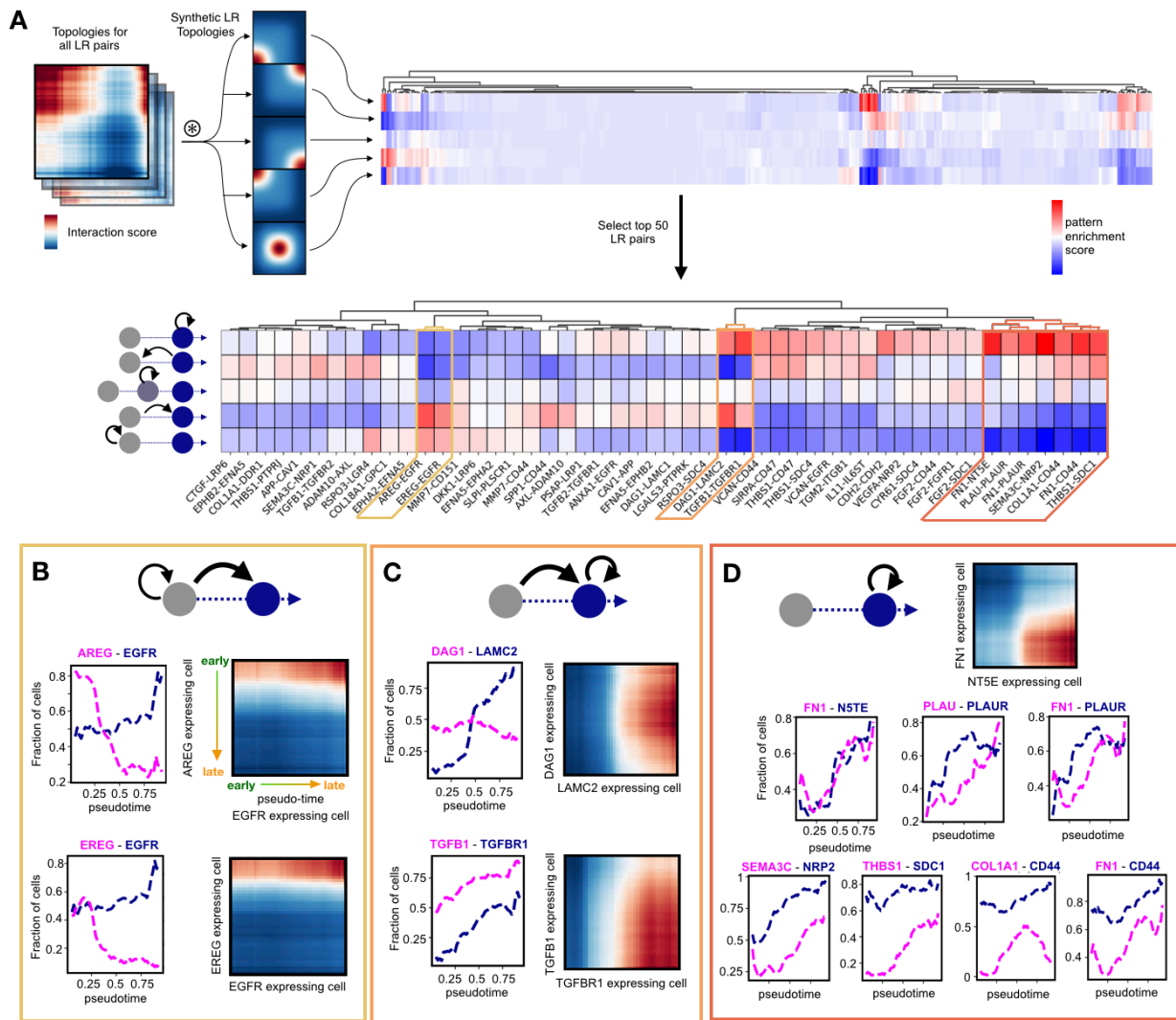
Figure 4-3: Supervised clustering of LR topologies quantifies the contribution of LR interactions. (A) Implementation of supervised clustering begins in a convolving LR topologies with a set of user-defined synthetic topologies. This operation results in a matrix where columns correspond to specific LR pairs and rows correspond to interaction patterns. (B-D) Specific interactions patterns and the matched LR expression profile and topology are highlighted.

Examining the top 50 LR pairs recaptured important hallmarks of EMT. For example, we observed an increase in a number of mesenchymal markers over pseudotime including fibronectin (Fn1) and fibrillar collagens(COL1A1)[141]. The expression profile of ligands also closely matched analyses performed on independent datasets[142]. More notably, POLARIS identifies an enrichment of cell-ECM interactions that are predominantly occurring between mesenchymal like-cells later in pseudotime. The observed autocrine signaling pattern may be suggesting a positive feedback mechanisms which continues to drive cells to become more mesenchymal-like (**Figure 4-3D**). These findings are consistent with studies on fibroblasts revealing ECM production activates a profibrotic positive feedback loop[143].

In addition to cell-ECM interactions, we also recovered other distinct interaction patterns (**Figure 4-3B,C**). For example, epidermal growth factor receptor (EGFR) occurs via a predominantly paracrine interaction between early epithelial-like cells and later mesenchymal like cells (**Figure 4-3B**).

4.2.3 POLARIS reveals regulatory patterns between independent lineages in colorectal cancer.

Many cancer treatments target components of the tumor microenvironment, including immune cells, extracellular matrix, and the tumor vasculature. Therefore, it is essential to investigate how these different components communicate to facilitate cancer progression. Recently, scRNA-seq analysis has successfully explored intratumoral heterogeneity in colorectal cancers(CRC)[144]. As an important follow-up, we evaluate how the different CRC TME cell types interact with and regulate each other. We examined a scRNA-seq dataset consisting of 7877 colorectal cancer cells, and 1239 matched normal cells from 6 patients from *Lee et al.* (2020)[145]. After pooling all the cells, each cell was assigned a pseudotime based on how far its gene expression diverged from the normal cell population (**Figure 4-4**). By applying this method, pseudotime values approximate cancer progression.

After computing pseudotime values for individual cells, we focused on three specific cell types: epithelial cells(5519 cells; 5024 tumor, 495 normal), myeloid cells (2371 cells; 1653 tumor, 718 normal), and fibroblasts (1226 cells; 1200 tumor, 26 normal). Each of these cell types was defined as its own lineage, resulting in three distinct lineages. We applied POLARIS to study the communication between and within each lineage **(Figure 4-5)**.

Similar to the analysis in section 4.3.2, there is an enrichment of cell-ECM interactions, particularly between epithelial-epithelial and epithelial-fibroblast cell populations. These results are consistent with prior studies demonstrating that EMT transition is associated with a metastatic CRC phenotype[146]. Additionally, the

directionality in signaling differs between the different cell populations. Malignant epithelial cell populations (later in pseudotime) interact with both normal and tumor-associated macrophages (**Figure 4-5B**). The trend between fibroblasts and epithelial cells is slightly different. A higher degree of signaling is observed between tumor-associated fibroblasts and normal epithelial cells (**Figure 4-5C**). These signaling patterns suggest that aberrant ECM production from tumor-associated fibroblasts interacts with epithelial cells to facilitate cancer progression. In myeloid - epithelial cell interactions, malignant tumor cells may be reprogramming myeloid cells to create a prometastatic niche. A closer inspection at LR pairs indicates several interactions with CD44 as significant. CD44 is a known stem cell marker for CRC[147], and because of the high degree of centrality, results suggest that targeting CD44 will significantly alter the observed cell-cell communication network.
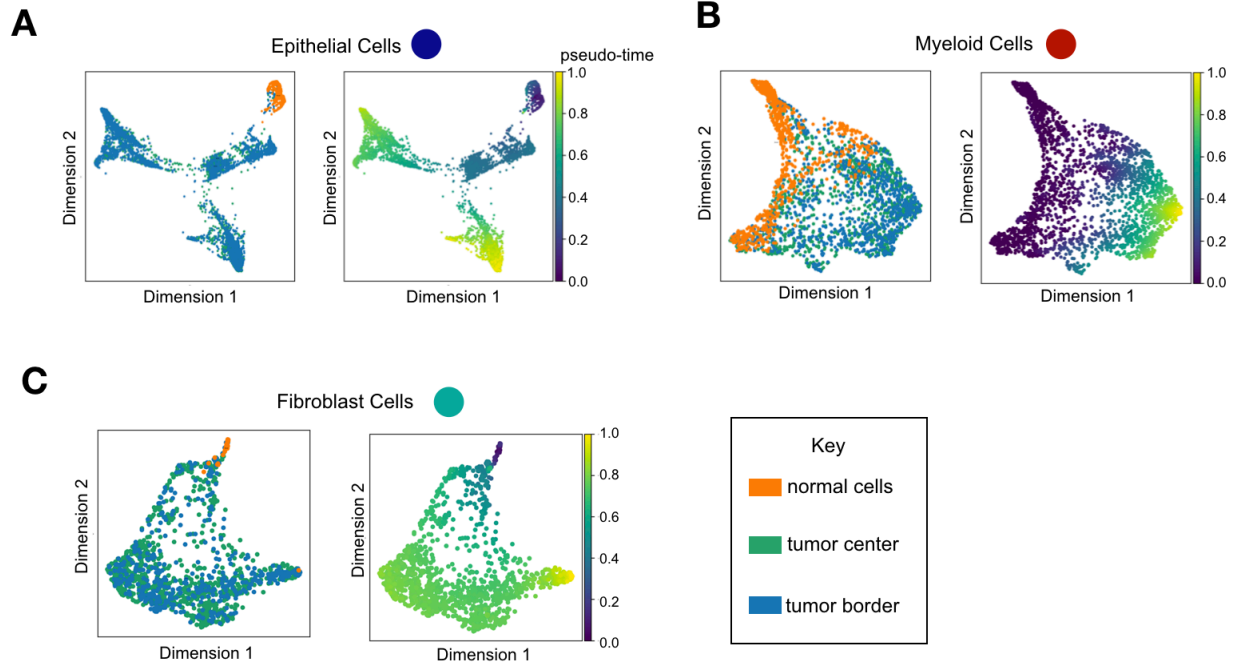
Figure 4-4: Pseudotime analysis of cell types in CRC. (A-C) Individual cells are colored based on their location within the tumor as annotated in *Lee et al.* (2020)[145] (left) or by the computed pseudotime scores (right). Epithelial cells (A), Myeloid cells (B) and Fibroblasts cells (C) were independently analyzed. ScRNA-seq data presented in this figure was obtained from *Lee et al.* (2020)[145].
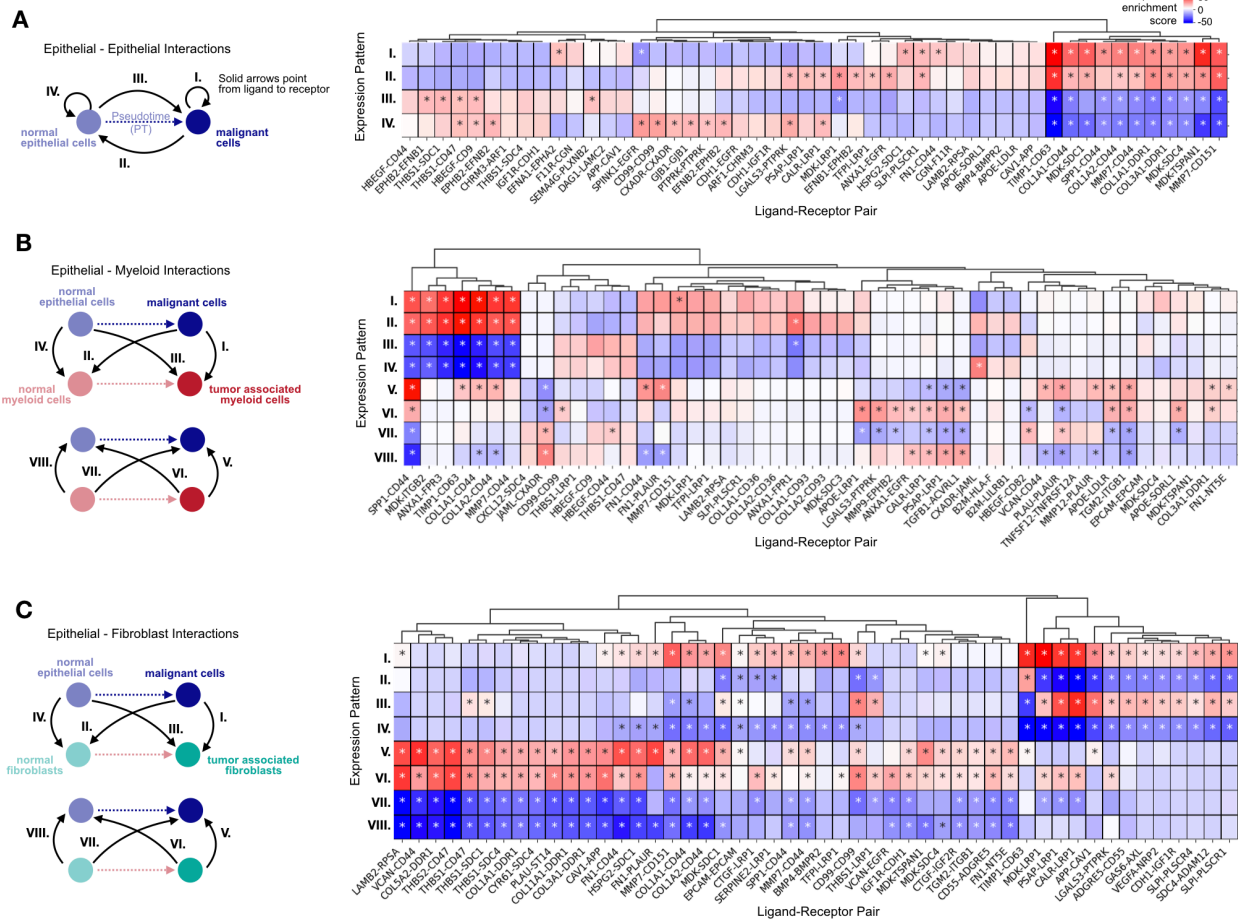
112

Figure 4-5. POLARIS evaluates intercellular communication between three independent lineages in CRC. (A-C) Signaling patterns between epithelial cells (A), epithelial and myeloid cells(B), and epithelial and fibroblasts cells (C) are highlighted. The contribution of each signaling pattern (left) is measured for each LR pair (right). The top 50 LR pairs are presented in the clustergram. For a more complete list of interactions see Figure C-1.

4.3 Discussion

      This chapter describes a new computational method, POLARIS, that

incorporates known LR interactions and single-cell trajectory inference results to identify

important LR-mediated signaling patterns that regulate a biological process of interest.

We applied this method to two independent scRNA-seq datasets. The EMT analysis

evaluated single-cells obtained from an *in vitro* study from a single lineage, while the

CRC analysis evaluated three independent lineages consisting of cells from patient

samples. We recovered several interactions and identified important signaling patterns

consistent with other reports. Cells undergoing EMT displayed several coordinated

interactions with extracellular matrix factors secreted by mesenchymal-like cells.

Furthermore, POLARIS predicted a potential feedforward signaling mechanism driving

EMT. In addition to identifying important signaling mediators in CRC progression, a

unique direction-dependent interaction pattern was observed between epithelial-myeloid

interactions and epithelial-fibroblast interactions.

      A majority of existing computational tools to quantify cellular interactions assume

that cells exist as discrete cell types and require a prerequisite cell clustering step[9].

Therefore, they do not account for a continuum of cell states. These methods aim to

understand the structure of global cell communication networks. However,

understanding how interactions within these networks affect dynamic biological

processes and vice versa requires evaluating how interactions change. A small number

of methods combine trajectory analysis with external LR datasets [24,148] as we have

here. The method presented in this chapter not only goes beyond correlating LR

interactions with pseudotime, but also sheds light on how cells at various points in

pseudotime regulate each other. As a result, we can uncover new regulatory patterns

between and within different cell types (**Figure 4-5**). Despite this, there are still several

improvements that can increase the accuracy of detecting potential regulatory patterns.

We can incorporate data from multi-subunit LR complexes and downstream signaling

patterns. Furthermore, combining results from other known LR methods can limit the

number of significant hits and enable more practical functional validation experiments.

With an increasing number of available scRNA-seq datasets, we hope computational

methods such as POLARIS become important hypothesis generation tools. LR

communication represents an important class of drug targets and inferring which LR

pairs regulate disease progression can help in improving the drug discovery pipeline.

4.4 Methods

4.4.1 Extracting LR expression profiles

For each LR pair and corresponding interacting lineages, two curves were fitted as a function of pseudotime. *l(t)* models the fraction of cells expressing the ligand over the course lineage 1, and *r(t)* models the fraction of cells expressing the receptor over the course of lineage 2. In the special case of studying interactions within a single lineage, both lineages 1 and 2 are the same.

Constructing LR expression profiles, denoted as *l(t)* and *r(t)*, occurs via a series of computational steps. (1) The ligand and receptor expression along with the cells in the lineage of interest are filtered from the gene expression matrix. (2) The ligand and receptor expression is binarized as presented in the equation below:

$$\boldsymbol{X}[i, j] = \begin{cases} 1, & \text{if } x \geq \delta \\ 0, & \text{otherwise} \end{cases}$$

$\boldsymbol{X}^{i,j}$ is the expression value for gene *i* in cell *j*. If the number of transcript counts encoding a particular ligand or receptor is greater than a tunable threshold δ for a particular cell, then that cell is expressing the ligand or receptor of interest. For the analyses presented in this chapter, δ is set to 0.

(3) A sliding window model is implemented to construct *l(t)* and *r(t)*. Parameters of this model are the sliding window width and the step size. Discretization of functions *l(t)* and *r(t)* are computed. In summary, a sliding window operates over pseudotime (**t**) which ranges from 0 to 1. For all the cells falling within each window width(**w**), the fraction of cells expressing the particular ligand or receptor is determined. Following the first

iteration, the sliding window moved forward by a step size (**s**) and this process is repeated. As **s** approaches 0, *l(t)* and *r(t)* become continuous functions over pseudotime. For computational efficiency, the analyses presented in this chapter used the following parameters: **w**=0.2 and **s**=0.02.

4.4.2 Constructing LR topologies

For each ligand-receptor pair, two expression profiles are calculated: *l(t)* and *r(t)* as described in section 4.4.1. These functions have been discretized and stored as individual arrays, denoted as *l* and *r*. The size of both arrays are the same and dependent on the parameters (**w** and **s**) used to construct them. The tensor product or outer product, $l^T r = l \otimes r$, is used to generate an LR topology.

Each LR topology encodes interactions between two lineages via a particular LR pair. For example, consider two different LR pairs. In the first LR pair, cells later in pseudotime are interacting with cells earlier in pseudotime. For the second LR pair, an autocrine interaction is observed where only cells later in pseudotime are interacting with each other. The LR topologies representing both of the these unique interactions will be distinct. Applying additional computational methods such as machine learning algorithms can dissect and uncover the different types of interactions encoded by LR topologies.

4.4.3 PCA analysis and supervised clustering of LR topologies

Principal components analysis (PCA): LR topologies are implemented as 2D matrices. Each of these matrices are flattened to construct a feature vector. Prior to running PCA, feature vectors are standardized ($\mu=0$, $\sigma=1$).

Supervised clustering analysis: the goal of this analysis is to identify the contribution of user defined interaction patterns for each observed LR interaction. For the analyses presented section 4.2.2 and 4.2.3, a total of five and four user predefined topologies were created, respectively. Convolving each of the empirically derived LR topologies with the user defined topologies of the same size results in a numerical score. A high score indicates that the particular user defined interaction pattern is strongly observed between the two lineages, while a score highlights that the observed pattern is not observed. Repeating this process for each LR topology and all the user defined topologies results in a matrix where the rows correspond to a particular user-defined interaction pattern (4 or 5) and the columns correspond to different LR pairs (**Figure 4-6**). To construct a clustergram from this matrix, we applied hierarchical clustering with euclidean distance and complete linkage using the python Seaborn package.
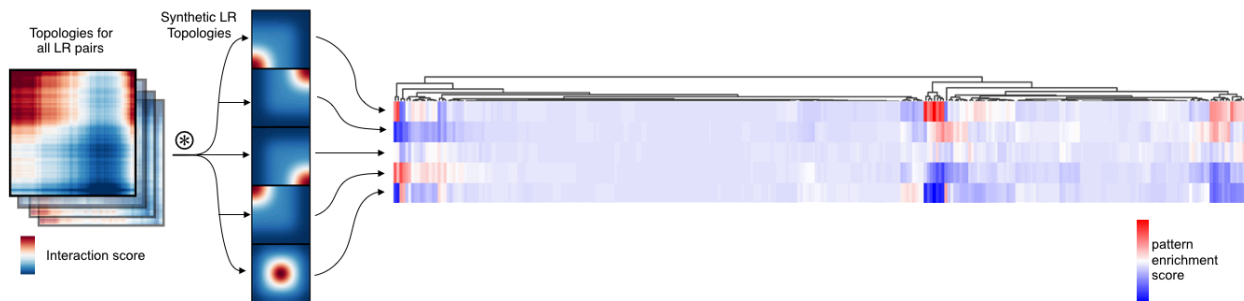
Figure 4-6: Supervised clustering of LR topologies. By convolving LR topologies with user-defined synthetic topologies, LR pairs can be sorted based on the type of signaling pattern they are displaying.

4.4.4 Statistical Significance Testing

Following supervised clustering, we identify how much specific interaction patterns are contributing to the empirical LR topologies. Determination of which of these interaction patterns is significant is accomplished for each LR pair individually via the following steps. Because LR topologies are computationally represented 2D matrices, we can model each matrix element via a gamma distribution (**Figure 4-7**). Based on the discovered the gamma distribution parameters, we generate a series of synthetic topologies that share the same distribution. For the current implementation this hyper-parameter is set to 100, but can be modified depending on the user and desired significance threshold. Each of these synthetic topologies is convolved with a user-defined topology of interest as detailed in section 4.4.3, to generate a score. Finally,

significance is computed by quantifying the number of synthetic topologies that scored

higher than the original LR topology divided by the total number of synthetic topologies.

In summary, this permutation based method quantifies the chances of observing a

particular interaction score by chance for the LR pair of interest. To correct for multiple

hypotheses, a Bonferonni correction was applied to the computed significance values

by dividing each significance score by the total number of LR pairs evaluated. The

significance threshold in the cluster gram was p=0.05.
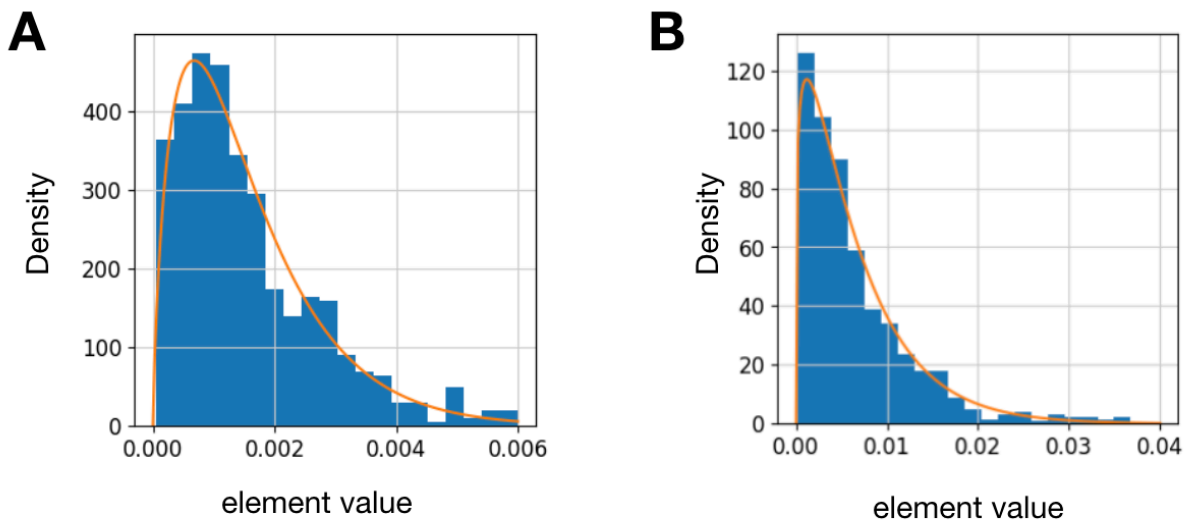
Figure 4-7: A gamma distribution fitted to a distribution of element values as described in section 4.4.4. Synthetic topologies are created by elements from sampling these gamma distributions.

4.4.5 Single-cell RNA-seq datasets, data preprocessing, and analysis

Two different scRNA-seq datasets were analyzed in this chapter. In section 4.2.2, scRNA-seq data from *Cook et al.* (2020)[140] consisting of A549 cancer cells with EMT induced by TGFB1 treatment was analyzed. Cell count data was downloaded from NCBI Gene Expression Omnibus (Accession No. GSE147405). Only cells that were left untreated or treated for 8 hrs, 1 day, 3 days, and 7days with TGFB1 were included. The pseudotime scores presented in the manuscript were used in our analyses.

In section 4.2.3, we analyzed the Kul3 colon cancer scRNA-seq dataset from *Lee et al.* (2020)[145]. Cell type labels, counts matrix, and normalized expression matrix were obtained from the NCBI Gene Expression Omnibus (Accession No. GSE132465). Pseudotime was computed for epithelial cells, myeloid cells, and fibroblast cell populations independently. To compute the psuedotime for epithelial cells, the relevant cell lines were first filtered from the normalized gene expression matrix. Epithelial cells classified as one of the following subsets were not included in further analyses: BEST4+ Enterocytes, Goblet cells, Intermediate Enterocytes, Mature Enterocytes, and Tuft cells. The expression matrix and metadata were stored as Scanpy objects. Cells were clustered based on gene expression using the Leiden algorithm (resolution=0.3)[149]. A single cell was randomly selected from a cluster with predominately normal epithelial stem cell population and was defined as a pseudotime of 0. Diffusion pseudotime (DPT) was used to determine a pseudotime value for the remaining cells[138]. Single cells were visualized using a UMAP projection. DPT, UMAP, and clustering was implemented from prebuilt functions from the Scanpy package. This process was similarly repeated for fibroblast cell populations.

For the myeloid cell population, two distinct cell populations were present in normal tissue, and therefore, identifying a single cluster to represent the beginning of pseudotime or root cell was challenging. To circumvent this problem, single cells were projected onto a 2D image using UMAP (Uniform Manifold Approximation and Projection). Each cell was assigned a numerical value representing the distance between itself and the nearest normal cell. These distance values were normalized to represent a pseudotime score between 0 and 1. The farther a cell is from a normal cell, the more differentiated it has become and the higher the pseudotime score. Normalized expression matrices were only used to compute pseudotime scores. For subsequent analyses presented in the methods above, the counts matrix was used.

4.4.6 Implementation Details

All analyses and methods were developed using Python v3.7.4. Clustergrams were constructed using the Seaborn package. All other figures were constructed using the Matplotlib. PCA analyses was performed using Scikit-Learn. Additional matrix operations were completed using the Numpy and Scipy packages. Single-cell analysis including pseudotime computation was accomplished using prebuilt functions from the Scanpy package.

Chapter 5 Discussion

In this thesis, I have presented new computational and imaging methods to improve our understanding of how intercellular communication can affect dynamic cellular processes. Technical advances over the past decade have provided a detailed characterization of mammalian tissue through the study of gene expression (i.e., single-cell RNA-sequencing), epigenetic state (i.e., scATAC-seq), spatial transcriptomics (i.e. slide-seq), protein localization (i.e., CycIF), and more. However, quantitative methods for capturing behavior for individual cells within a tissue remain limited. Static snapshots of tissue are insufficient to understand how spatiotemporally regulated processes such as tissue homeostasis, organ development, and embryogenesis operate.

Diseases such as cancer are also highly dynamic. For example, the relationship between cancer cell dissemination and the TME often involves a rare subset of cells that have gained invasive properties. Therefore, methods that can accurately model the TME and detect subtle changes during cancer progression are essential to obtain a complete picture of the dynamic processes that ultimately lead to treatment resistance and metastasis. Methods such as *in vivo* imaging allow us to monitor cells in real-time. However, due to limited multiplexing ability, it remains challenging to decipher the role of intercellular communication in modulating a cells' behavior.
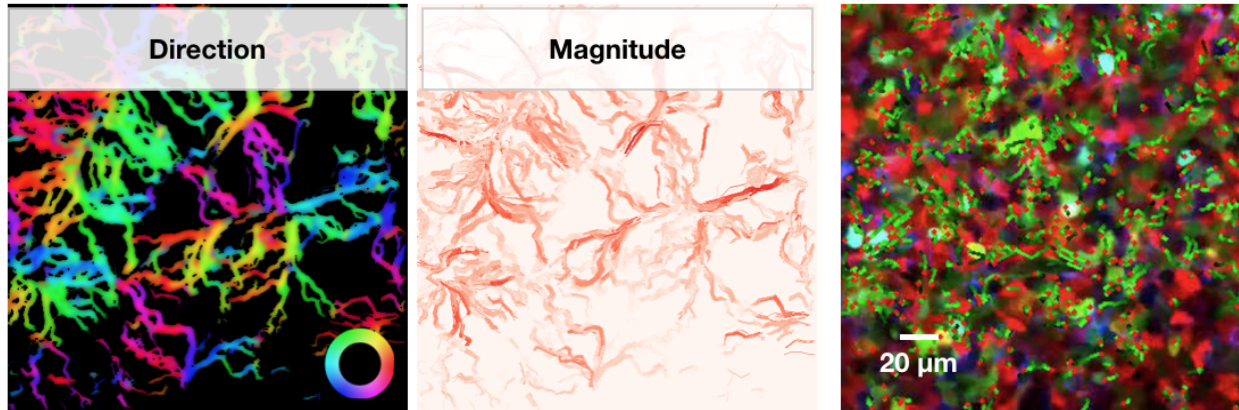
Figure 5-1. Applying DT to capture direction and magnitude of tumor microvasculature (left, middle) and cellular motion and perform pixel-by-pixel tracking in dense tissue (right).

To tackle this challenging problem, I specifically focus on the role of tumor-associated macrophages and cancer cell dynamics. This case study is fundamental to understanding the mechanisms that drive cancer progression. Tumor-associated macrophages (TAMs) represent an important class of immune infiltrates in the tumor microenvironment that has variable effects on cancer progression depending on their polarization state. Classically, TAMs exist along a spectrum of polarization states, with the extremes labeled as M2 or anti-inflammatory/pro-tumorigenic and M1 or pro-inflammatory/anti-tumorigenic[150]. Recently, single-cell transcriptomics has revealed several additional polarization states *in vivo* [151]. Based on these efforts, TAMs have also been suggested as targets for new immunotherapies[103] or combinatorial treatments to counter cancer bypass signaling[11].

I begin my thesis by detailing a novel pipeline to quantitatively study cytoskeletal dynamics of cancer cells (chapter 1), and how such dynamics correlate to higher-level features such as cell morphology and migration rates. I discovered that interaction with the 3D extracellular matrix and infiltrating immune cells (namely macrophages) can

independently lead to increased coherent microtubule alignment in metastasizing cancer cells (chapter 2).

In addition to studying how intercellular interactions affect sub-cellular dynamics, I inferred on a global level how intercellular interaction affect specific biological processes (chapter 3). I created a new computational method, called POLARIS, which combines traditional LR interaction analysis with single-cell pseudotime analysis to infer dynamic information from a static snapshot of gene expression values.

Despite the advancements presented in this thesis on understanding cellular dynamics, several improvements can enable more high throughput analysis of spatiotemporal dynamics. The developments presented here only capture a small number of dynamical features, namely microtubule dynamics, cell movement, and disease progression (via single-cell trajectory inference methods). Ideally, it would be beneficial to automatically capture dynamical features from *in vivo time-lapse* microscopy regardless of the experimental conditions. Analysis of subcellular dynamics such as lipid droplet behavior can be used to study cancer metabolism. High-resolution imaging of fluorescently labeled drugs can also provide insight into drug distribution within the tumor. Small optical probes can be used to study fluid flow in the tumor microvasculature and activation of specific molecular signaling pathways (i.e. phosphosignaling).

Action-recognitions methods in computer vision offer one exciting approach to address this problem. Dense trajectories (DT) have outperformed other action-recognition methods, except for neural networks (which require many curated videos under similar imaging conditions, limiting its generalizability)[152]. A proposed pipeline for

applying DT on time-lapse intravital microscopy to track the motion of various biological features is as follows. Implementation of DT yields a vector field capturing each pixel's velocity in a series of time-lapse images[153,154]. Each vector can be assigned a cell based on the prior cell segmentation results. DT vectors also store metadata capturing the environment around each pixel. This makes DT ideal for capturing local microenvironmental changes surrounding individual cells, especially relevant in cancer research. Furthermore, DT may potentially be able to quantify many different types of dynamics, including cytoskeletal changes and drug transport, compared to specialized tracking software (i.e., U-track[92]).

In addition to creating a more generalizable approach to capture cellular and sub-cellular dynamics by computational methods such as DT, another challenging problem involves understanding the link between dynamic measurements and molecular markers. This task requires developing new high throughput methods to simultaneously capture dynamic and molecular features *in vivo,* analogous to how spatial transcriptomic approaches capture spatial and molecular features.

In conclusion, I hope these discoveries improve our understanding of what interactions contribute to disease progression and make cancer cells motile and how to target this motility to prevent cancer metastasis. More generally, I hope this research paves the way for more detailed high-throughput dynamical studies to gain a functional understanding of biological processes, in addition to tissue structure and composition.
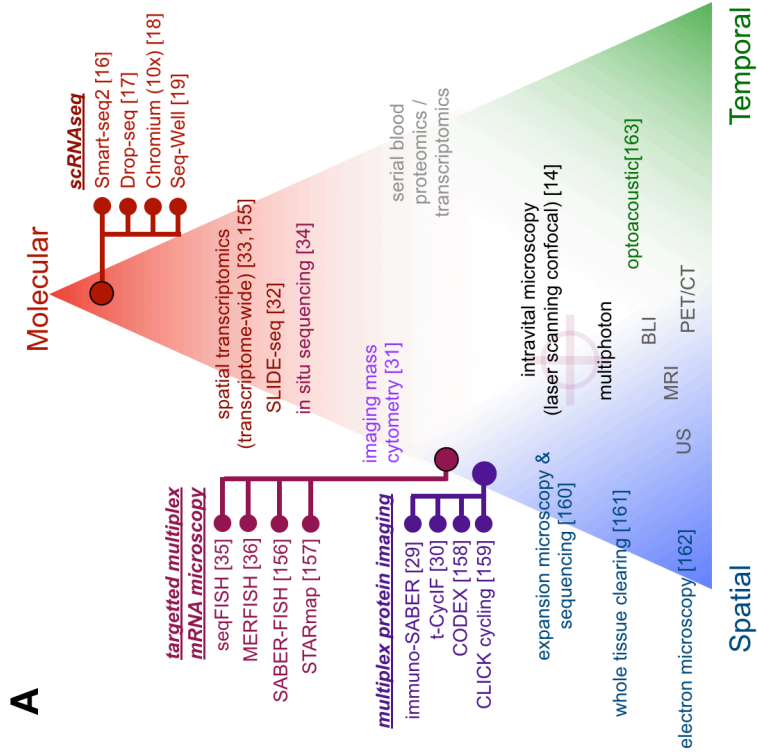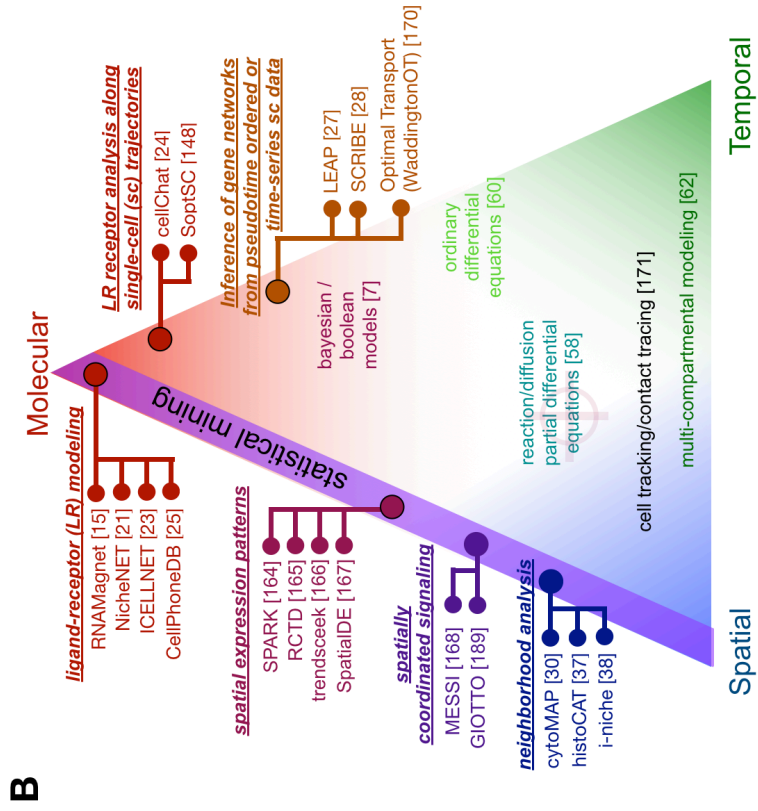
Appendix A Supplementary Information for Chapter 1

A

scRNAseq
Smart-seq2 [16]
Drop-seq [17]
Chromium (10x) [18]
Seq-Well [19]

Molecular

targetted multiplex mRNA microscopy
seqFISH [35]
MERFISH [36]
SABER-FISH [156]
STARmap [157]

spatial transcriptomics
(transcriptome-wide) [33,155]
SLIDE-seq [32]
in situ sequencing [34]

serial blood
proteomics /
transcriptomics

multiplex protein imaging
immuno-SABER [29]
t-CycIF [30]
CODEX [158]
CLICK cycling [159]

imaging mass
cytometry [31]

intravital microscopy
(laser scanning confocal) [14]
multiphoton
BLI
optoacoustic[163]

expansion microscopy &
sequencing [160]

MRI
PET/CT

whole tissue clearing [161]

US

electron microscopy[162]

Spatial

Temporal

B

Molecular

LR receptor analysis along single-cell (scl) trajectories
cellChat [24]
SoptSC [148]

Inference of gene networks from pseudotime ordered or time-series sc data
LEAP [27]
SCRIBE [28]
Optimal Transport
(WaddingtonOT) [170]

ligand-receptor (LR) modeling
RNAMagnet [15]
NicheNET [21]
ICELLNET [23]
CellPhoneDB [25]

bayesian /
boolean
models [7]

ordinary
differential
equations [60]

statistical mining

spatial expression patterns
SPARK [164]
RCTD [165]
trendsceek [166]
SpatialDE [167]

spatially coordinated signaling
MESSI [168]
GIOTTO [189]

reaction/diffusion
partial differential
equations [58]

cell tracking/contact tracing [171]

multi-compartmental modeling [62]

neighborhood analysis
cytoMAP [30]
histoCAT [37]
i-niche [38]

Spatial

Temporal

128

Figure A-1: (A) Experimental and (B) computational methods for studying intercellular communication in mammalian tissue. Each method highlighted above is approximately placed along a spectrum of molecular, spatial, and temporal resolutions based on the type of information captured or analyzed. For example, scRNA-seq methods capture detailed molecular information (gene expression), but not spatial and temporal properties of a tissue, and therefore, located at one extreme. Multiplex imaging technologies measure spatial and molecular information and are located along the spatial-molecular axis. Note: This is a highlight reel with examples, rather than a comprehensive list of methods.

Appendix B Supplementary Information for Chapter 2

A

in vivo MT tracks
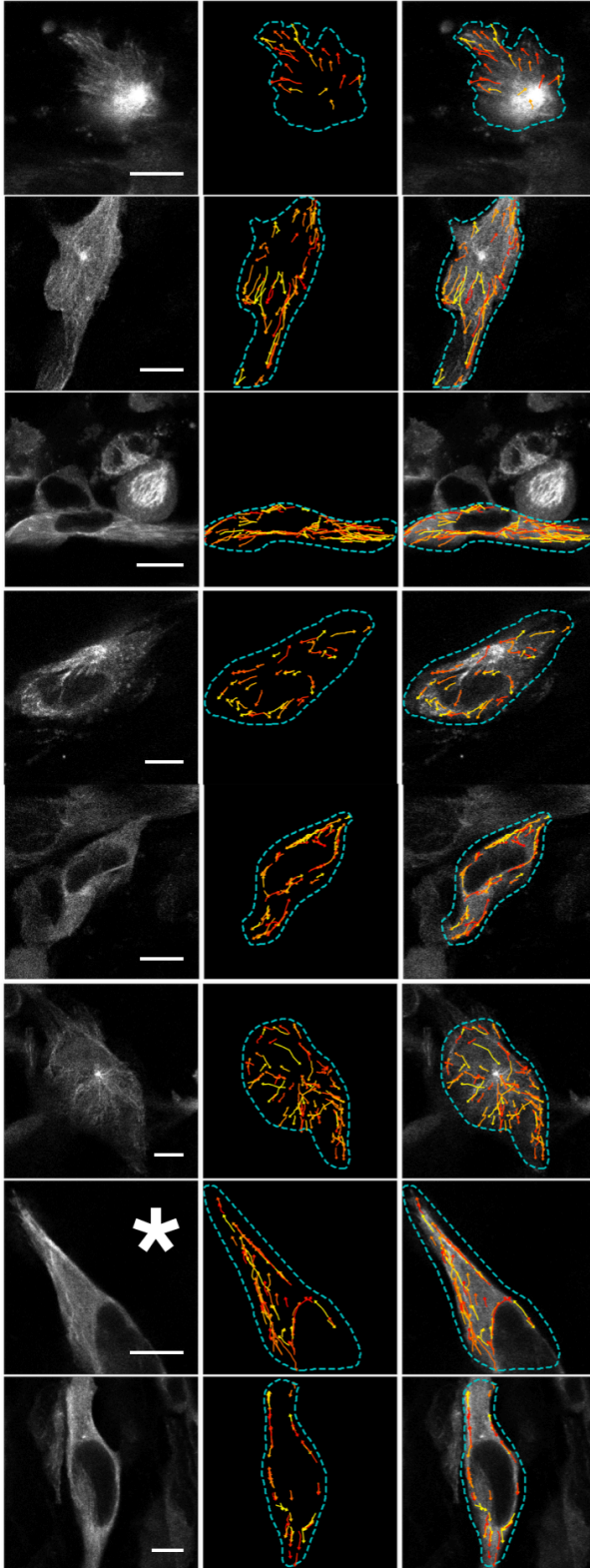
B

in vitro MT tracks

131
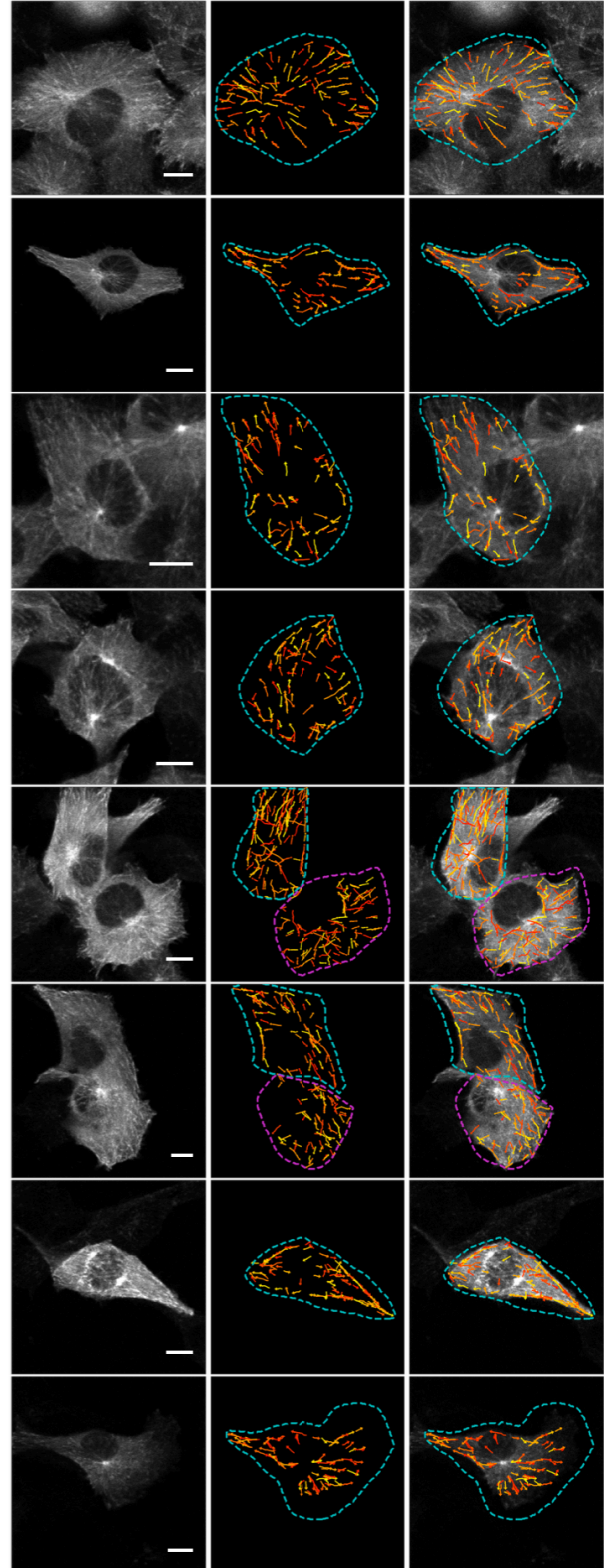
Figure B-1. Visualizing *in vivo* and *in vitro* MT tracks.

(A) Representative *in vivo* time-lapse images of HT1080 EB3-mApple cells growing in a dorsal window chamber were obtained via IVM (left). MT tracks were computationally identified (center) and randomly pseudo-colored from red to yellow. (B) Representative *in vitro* time-lapse images were obtained from HT1080 EB3-mApple cells in 2D culture using the same imaging system (left) and computational tracking software (center). (A-B) Scale bar, 10 µm. Asterisks mark cells excluded in analysis due to incomplete cell imaging within the field of view. A total of n=34 *in vivo* cells and n=39 *in vitro* cells were analyzed.
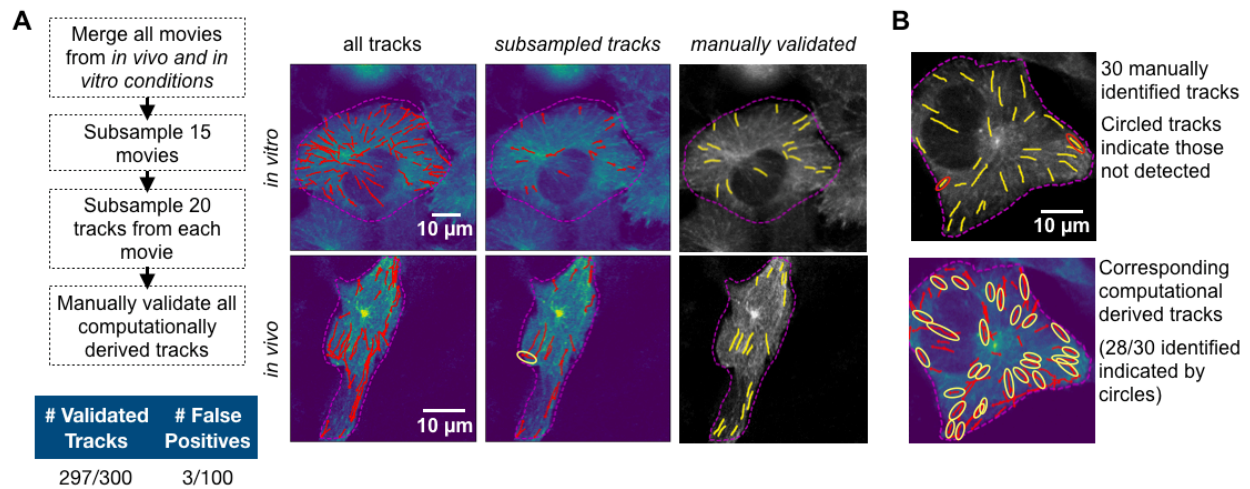
Figure B-2. (A) Workflow (left), example case (middle), and statistics (right) for hand-validation of MT tracking to assess false positive rate. (B) False negative estimation is challenging as confirming the identity of all tracks is a difficult task. Nevertheless, we identified 30 of the most visible tracks in one representative *in vitro* movie and determined how many of these tracks were computationally detected and analyzed.

MT feature	R^2	P-value
Curvature	0.02	0.38
Edge Distance	0.05	0.15
Distance to Major Axis	0.01	0.46
Orientation to Major Axis	0.01	0.66
Distance to Minor Axis	0.05	0.17
Displacement	0.22	0.00
Pathlength	0.19	0.01
Persistence	< 0.01	0.90
Speed	< 0.01	0.86
Max Speed	0.00	0.79
Min Speed	< 0.01	0.91
Speed SD	< 0.01	0.97
Local Coherence	0.01	0.66
Cellular Coherence	0.01	0.55
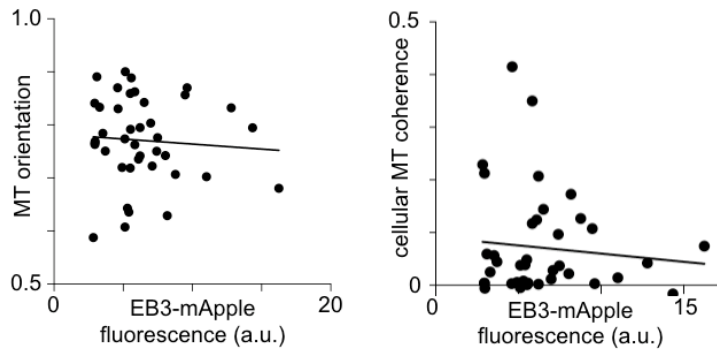
Figure B-3. Correlations between EB3 and cancer cell behavior. In HT1080 cells, EB3-mApple expression was examined for linear correlation with various MT features (Pearson's correlation coefficient; *two-tailed t-test; n=38 cells), with significant correlates highlighted in red. At right, corresponding cell-by-cell values for MT orientation and cellular MT coherence are shown (correlation not significant).
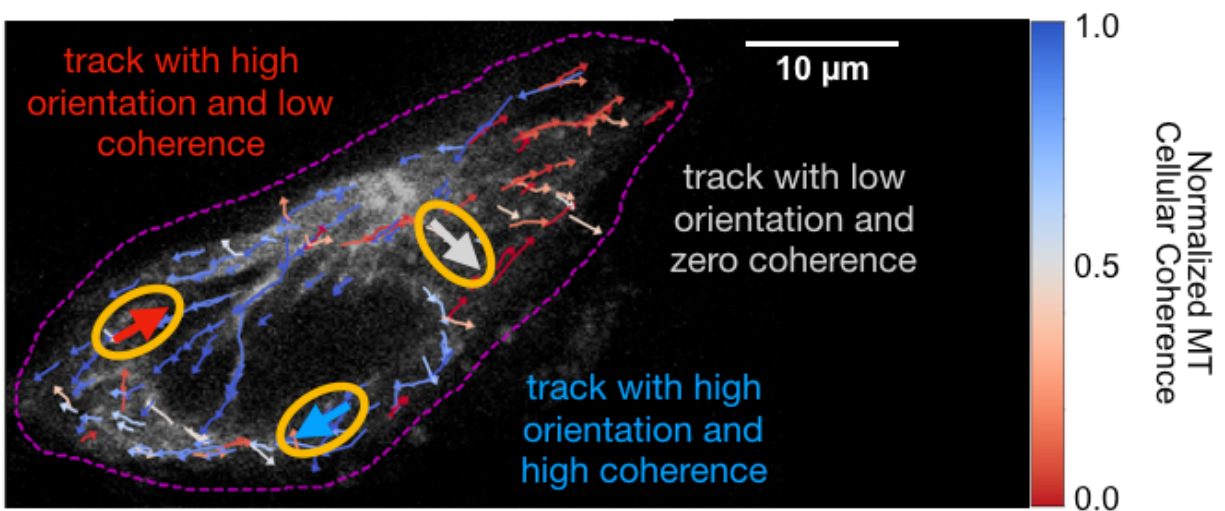
Figure B-4. Illustrative tracks showing varying levels of MT Orientation and Coherence (tracks are colored according to cellular coherence).
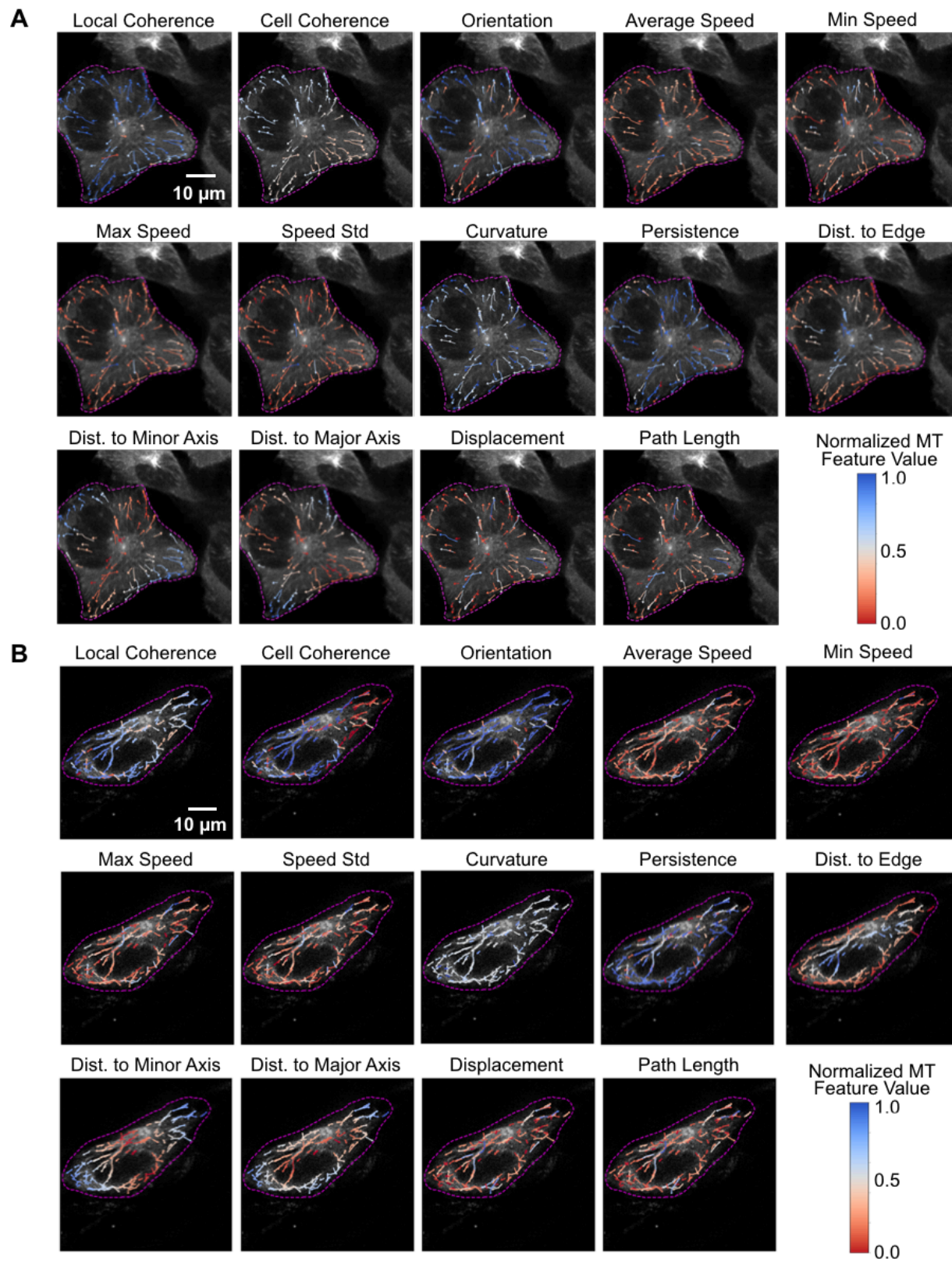
Figure B-5. Visualization of individual MT features.

(A) A representative HT1080 EB3-mApple cell grown in 2D culture is shown to visualize 14 MT track features. MT tracks are color coded based on the indicated track feature.

(B) A representative *in vivo* HT1080 EB3-mApple cell, where MT tracks are pseudo-colored according to the indicated feature above each image. Tracks were quantified for a total of n=73 *in vivo* and *in vitro* cells.
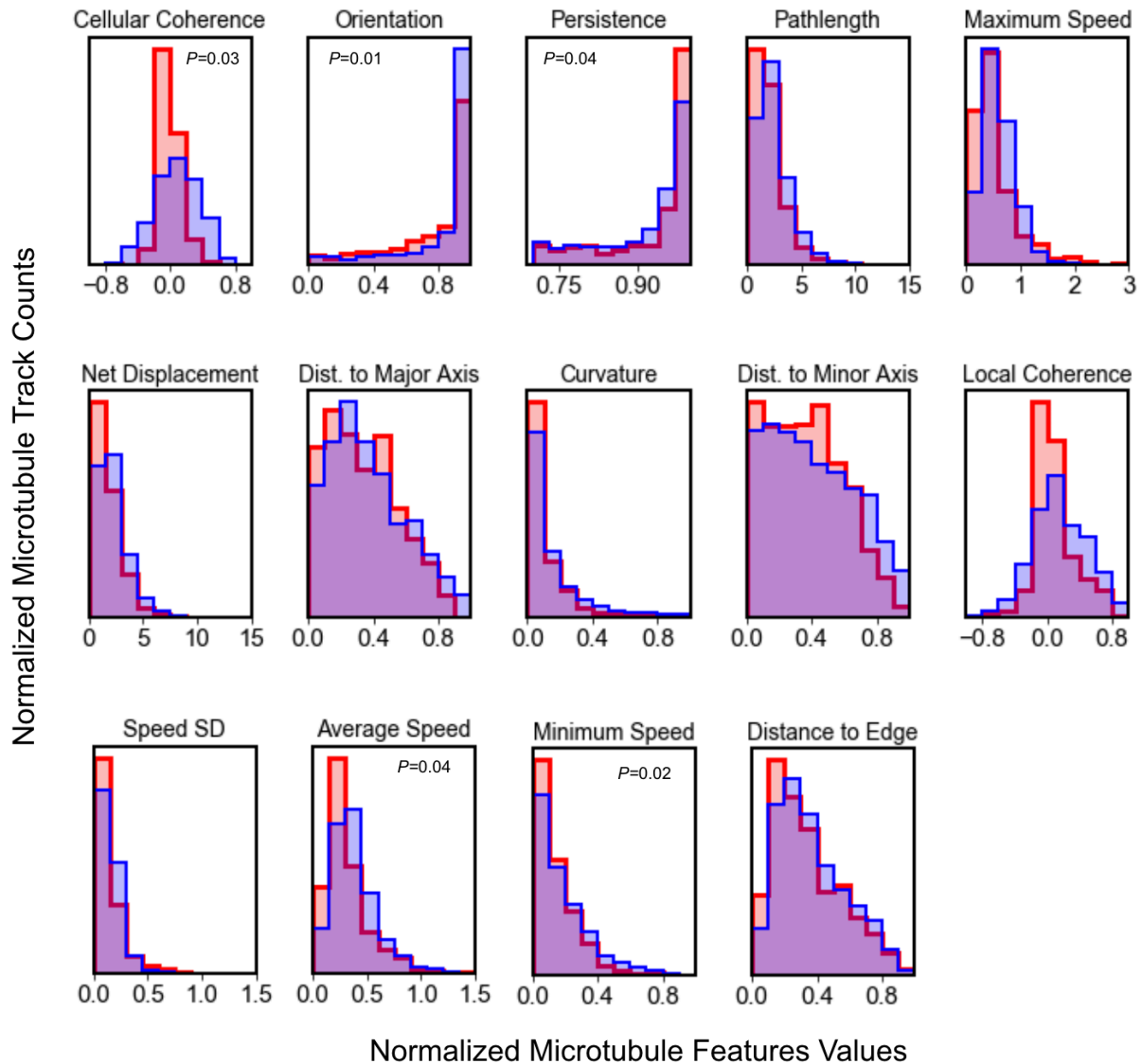
Figure B-6. Quantifying MT dynamics in ES2 xenografts. Distributions of MT dynamics imaged in ES2-EB3-mApple cells imaged *in vitro* or within ~2 week old subcutaneous xenografts in the dorsal window chamber model of nu/nu hosts (n=2,857 total tracks across 42 total cells and 5 tumors). *Two-tailed permutation test was performed for each distribution.

	Tracking Parameters (Threshold, Max Gap, Minimum Length)								P-Value
	4,2,4	4,4,3	3,0,4	3,2,4	3,3,4	5,4,3	4,0,3	5,0,3	
Orientation	0.68	0.67	0.69	0.68	0.68	0.66	0.67	0.66	1
Distance to Edge	269.09	261.74	267.27	271.08	269.66	248.70	261.74	250.99	0.97
Curvature	4.40	3.41	6.81	6.98	6.92	3.29	3.41	3.21	0.09
Distance to Minor Axis	0.45	0.45	0.46	0.46	0.46	0.46	0.45	0.45	1
Distance to Major Axis	0.40	0.40	0.42	0.42	0.42	0.40	0.40	0.40	1
Displacement (µm)	2.42	2.29	2.48	2.46	2.46	2.15	2.29	2.14	0.01*
Path Length (µm)	2.57	2.40	2.63	2.61	2.61	2.26	2.40	2.25	0.01*
Persistence	0.95	0.96	0.95	0.95	0.95	0.96	0.96	0.96	0.01*
Average Speed (µm/s)	0.31	0.37	0.33	0.33	0.33	0.34	0.37	0.34	0.97
Max Speed (µm/s)	0.52	0.58	0.55	0.54	0.55	0.55	0.58	0.55	1
Min Speed (µm/s)	0.15	0.20	0.16	0.16	0.16	0.17	0.20	0.17	0.68
Speed SD	0.13	0.14	0.14	0.14	0.14	0.14	0.14	0.14	0.99
Local Coherence	0.39	0.32	0.36	0.35	0.35	0.33	0.32	0.33	0.95
Cellular Coherence	0.22	0.17	0.17	0.17	0.16	0.19	0.17	0.19	0.97

Figure B-7. (*Continues on next page***).**
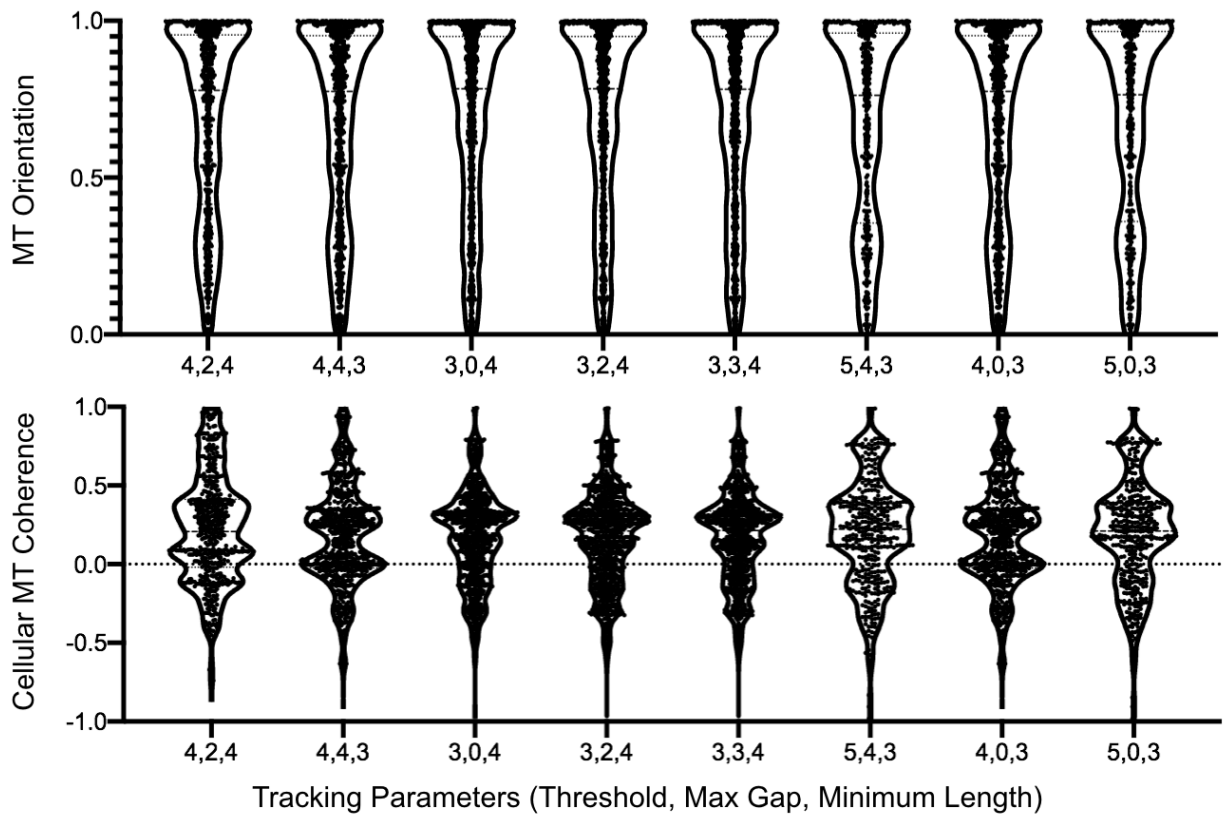
Figure B-7. Parameter sensitivity analysis in MT tracking. PlusTipTracker algorithm

parameters were varied and MT track features were recomputed using *in vitro* HT1080-

EB3-mApple cells, and single-track distributions are shown at bottom. Displacement,

persistence, and track length but not orientation or cellular MT coherence were sensitive

to the parameter changes (*kruskal-wallis (one-sided) based permutation test; n=15
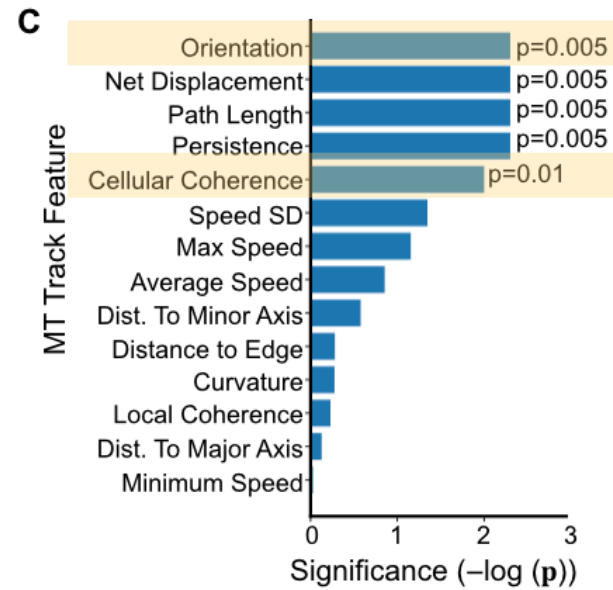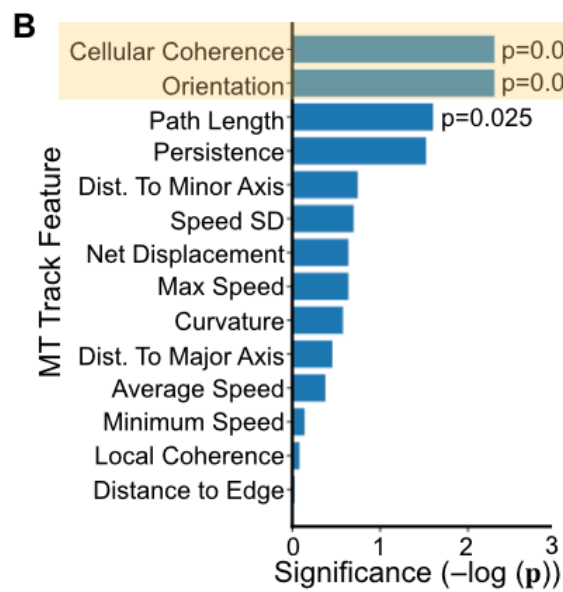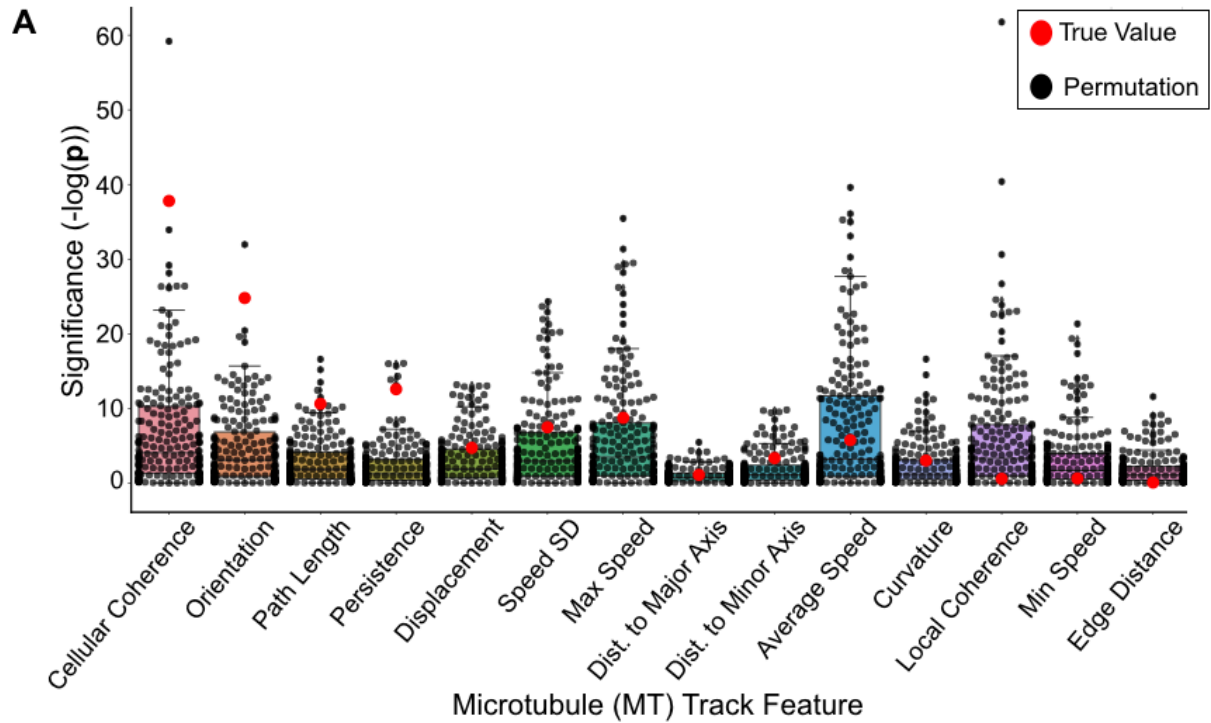
cells; center bar represent the median).

Figure B-8. (_Continues on next page)_

140
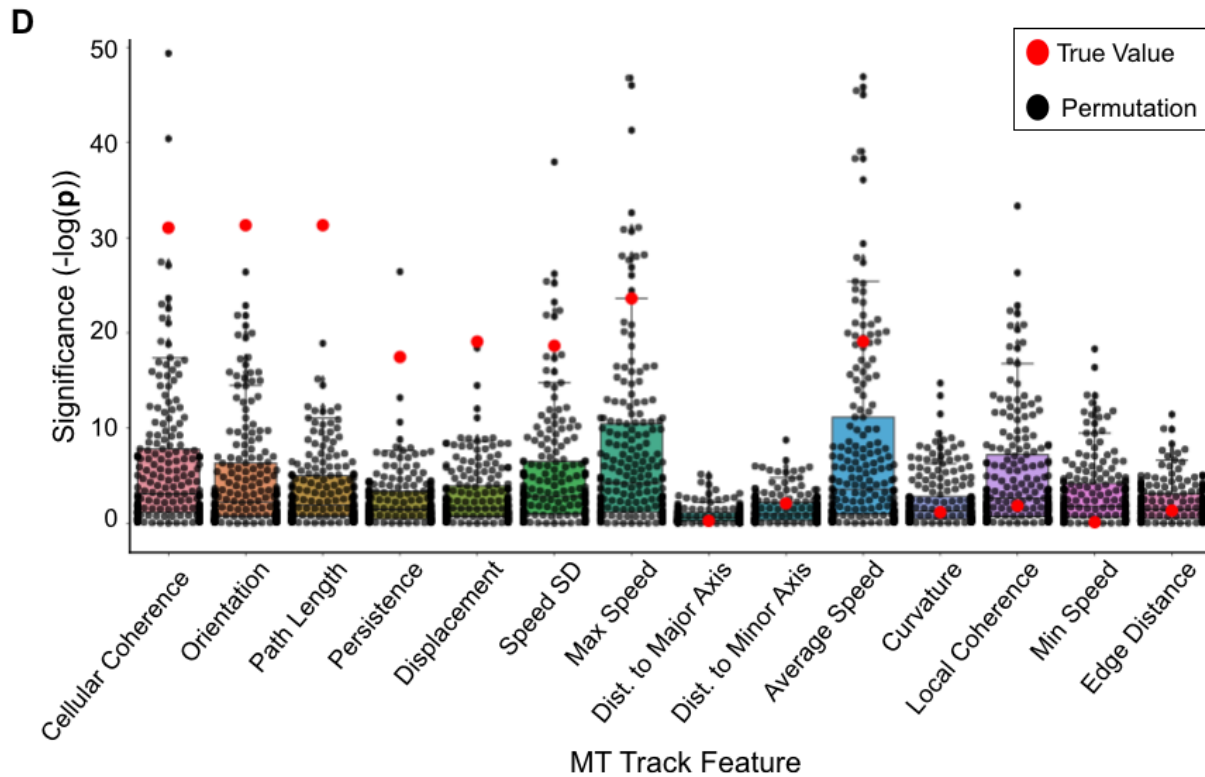
Figure B-8. Permutation testing of MT track statistics.

(A) A two-tailed wilcoxon rank-sum based permutation test was used to determine the statistical significance for each of the 14 MT track features between *in vivo* and *in vitro* HT1080 EB3-mApple cell populations. The wilcoxon statistic for the permutation (black) was compared to the wilcoxon statistic comparing the true *in vivo* and *in vitro* MT track distributions (red). (B) Corrected p-values were derived from the permutation test results shown in A (For A and B, n= 4983 tracks across 58 cells; 200 permutations). (C) To ensure that significance was not due to presence of incompletely imaged cells, the wilcoxon rank-sum permutation test was repeated after removing cells that were less than 80% visible. (D) Corresponding to C, the permutations (black) and true two-tailed

wilcoxon test statistic (red) comparing *in vivo* and *in vitro* HT1080 EB3-mApple included

cells mostly in the field of view (For C and D, n= 4673 tracks across 58 cells; 200

permutations). Additional un-occluded cells were added to the analysis to ensure that

the number of cells remains constant. P-values for B and C were computed using a two-

tailed permutation test. For A and D, a swarm plot overlays the box plot. The bars of the

box plot represent 1.5*IQR-Q1, Q1/25th percentile, median, 75th percentile, 1.5IQR*Q3,

and whiskers represent data points falling outside this range.

in vitro 3D cells
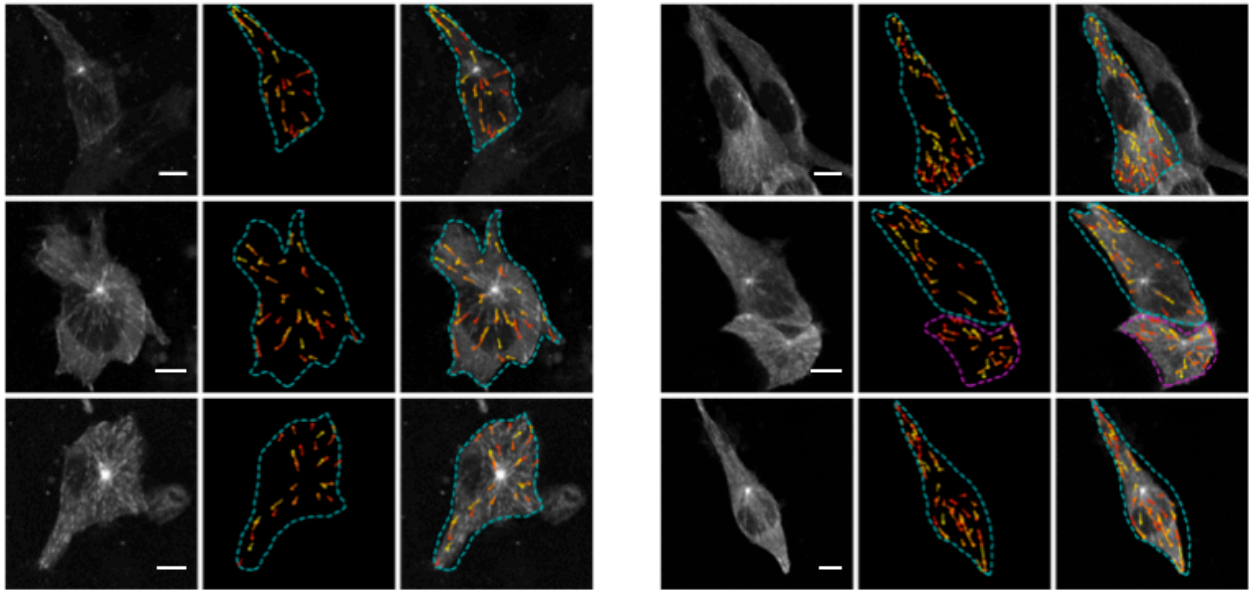
Figure B-9. Representative imaging of tumor cells in 3D culture.

Representative confocal images of HT1080 EB3-mApple cells grown in 3D collagen I gel culture with computationally-identified MT tracks randomly colored (scale bar=10μm).
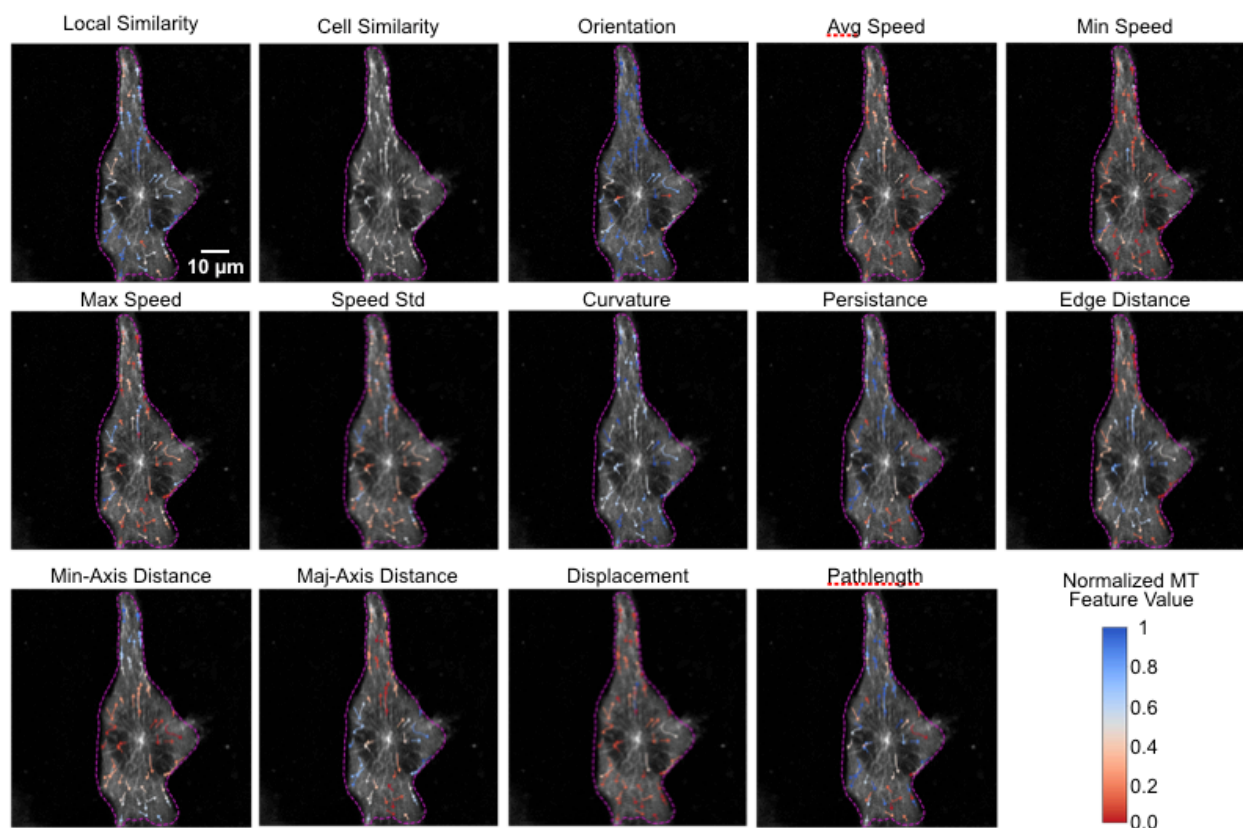
Figure B-10. Visualizing MT features of tumor cells in 3D culture.

A representative HT1080 EB3-mApple cell grown in 3D collagen I gel culture pseudo-colored according to the indicated MT feature above each image. A total of n=1325 tracks across n=12 *in vitro* 3D cells were analyzed.
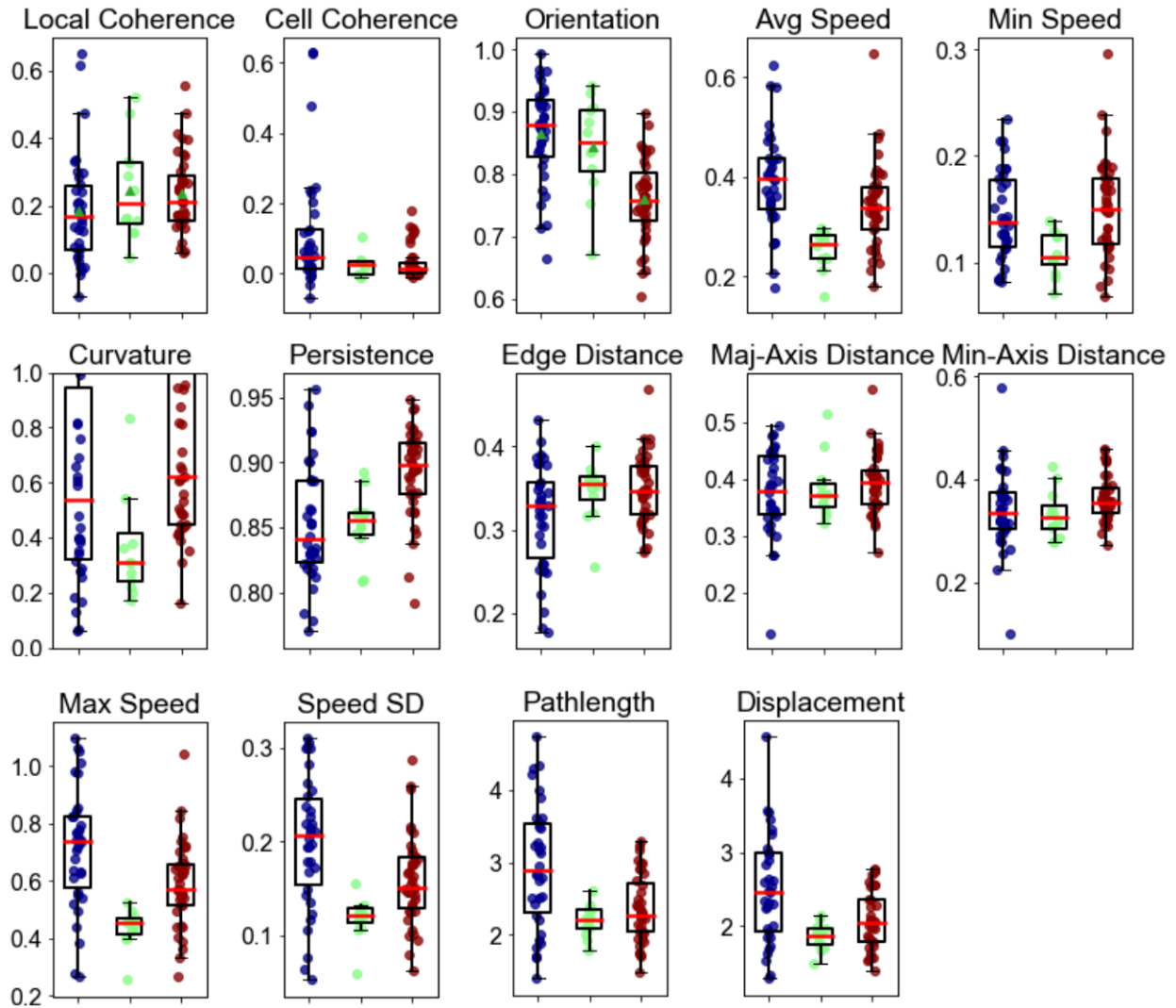
Figure B-11. Cell-average distributions of MT features.

Box plots show the cell medians for each MT track feature. HT1080 EB3-mApple cells were either grown on 2D culture (*in vitro*, red), grown in 3D collagen I gel (*in vitro* 3D, green), or grown *in vivo* (blue). The red bar denotes the median of the cell medians (total n=85 cells). For all, box plot defined as Q1/25%tile, median, Q3/75%tile with outliers falling outside Q3/Q1±1.5*IQR.

Appendix C Supplementary Information for Chapter 3
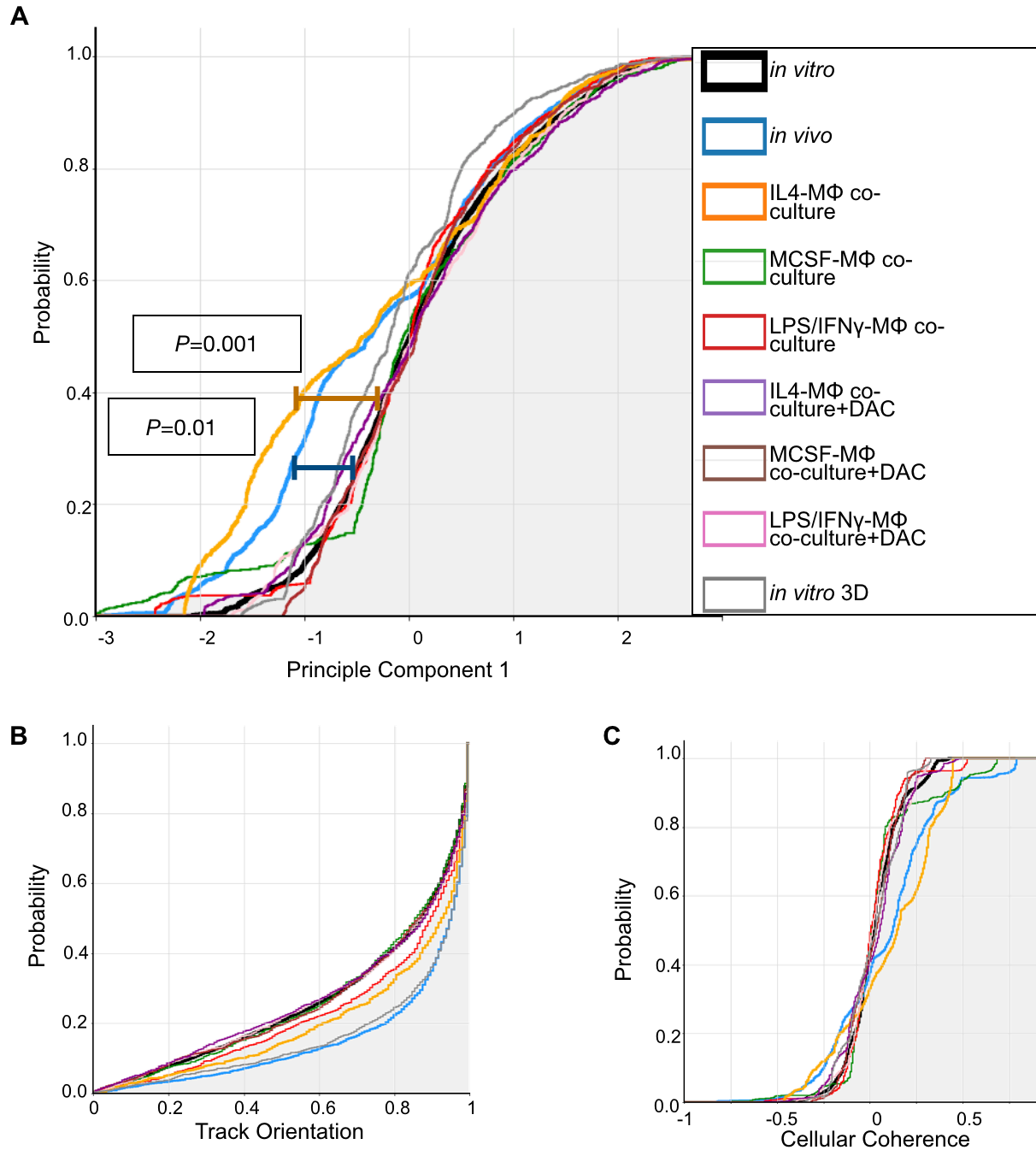
Figure C-1. (A) Covarying MT cellular coherence and orientation values were combined into a principal component for each MT track, and the cumulative probability distribution of principal component scores (PC scores) was then calculated for each culture condition (*two-tailed permutation test), reproduced for reference from **Figure 3-2C**. Corresponding to A, the cumulative probability distribution of (B) MT Orientation values

and (C) MT Cellular Coherence values were separately calculated for each culture

condition. For all (A-C), n=15,965 tracks from n=155 total cells. All box plots are defined

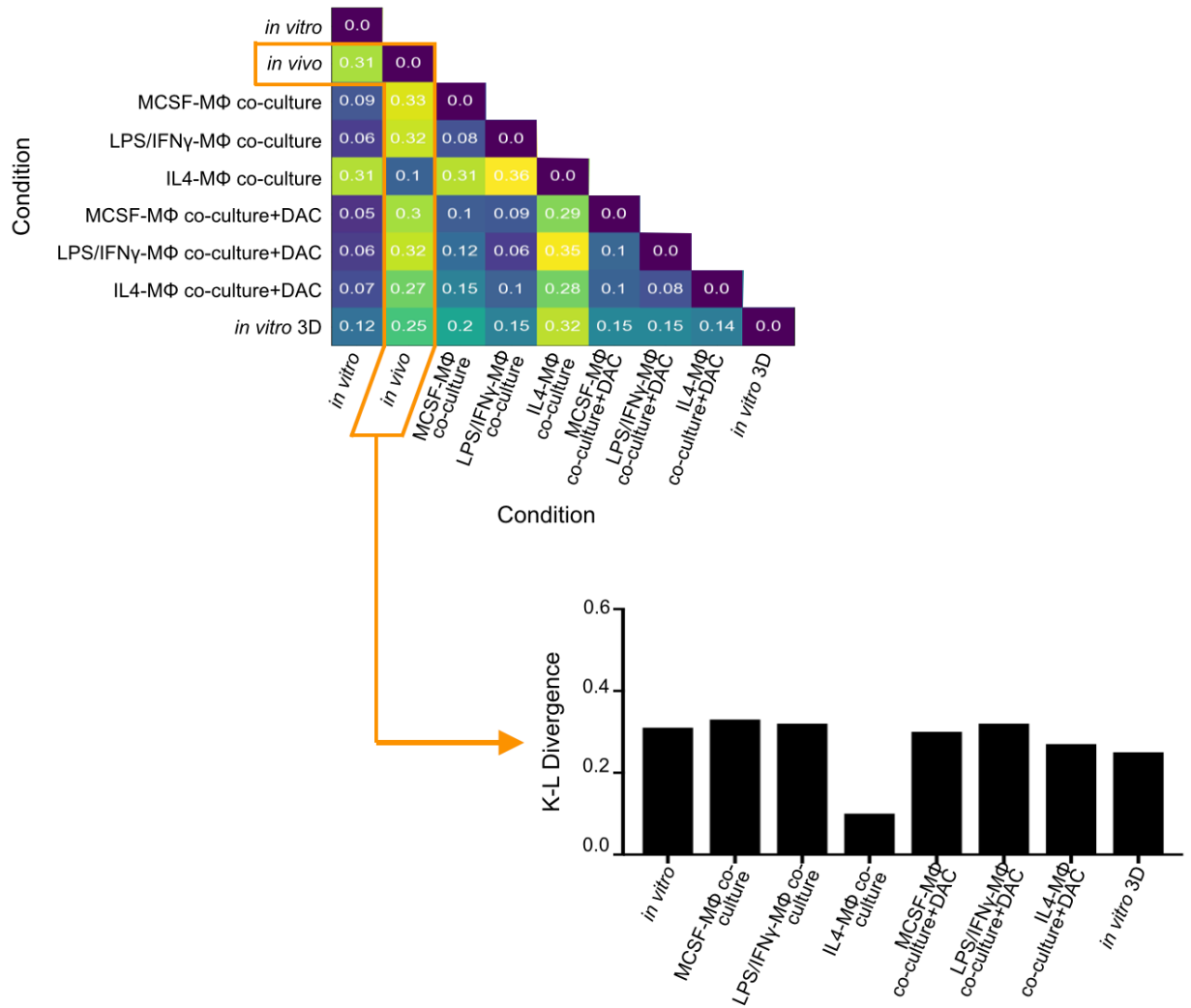as Q1/25%tile, median, Q3/75%tile with outliers falling outside Q3/Q1±1.5*IQR.

Figure C-2. Quantitative comparison of MT behavior under distinct culture conditions. From the PC scores in Figure C-1, the K-L divergence was computed between distributions from each culture condition. The bar-plot compares the K-L divergences of the *in vivo* PC score distribution to PC score distributions under all other conditions.
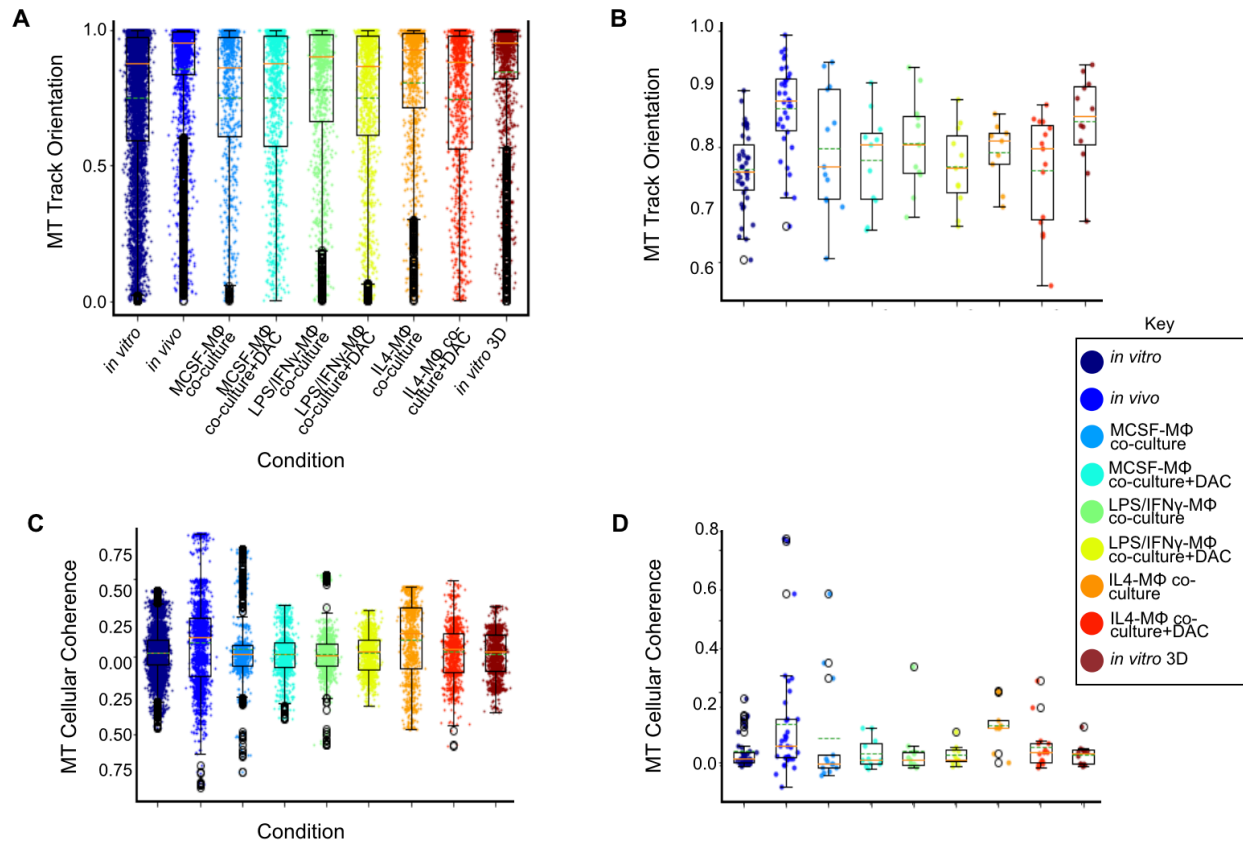
Figure C-3. Under each culture condition, the orientation value of (A) all tracks and the (B) cell-averages were calculated and visualized. Likewise the cellular coherence value for (C) all tracks and the (D) cell averages are shown. The red line denotes the median value of either all tracks(A, C) or the cell averages (B, D). For all (A-D), n=15,965 tracks from n=155 total cells. All box plots are defined as Q1/25%tile, median, Q3/75%tile with outliers falling outside Q3/Q1±1.5*IQR.
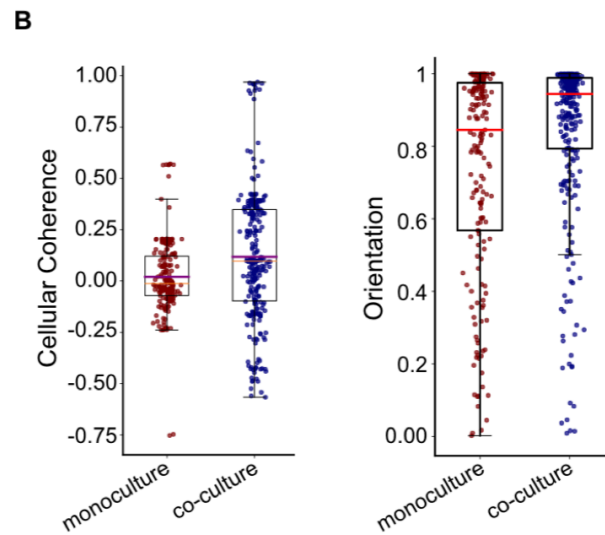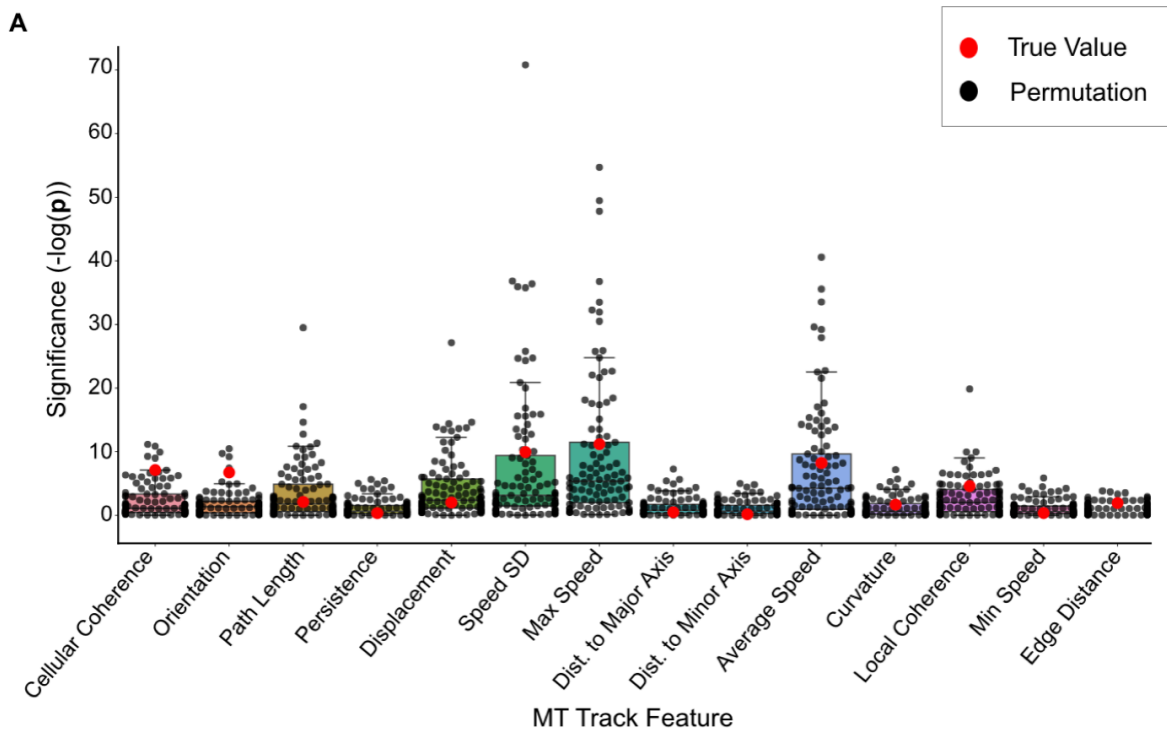
Figure C-4. Permutation statistics and individual track-level data in the ES2 co-culture model.

(A) A wilcoxon rank-sum based permutation test was used to determine the statistical significance for each of the 14 MT track features between ES2 EB3-mApple cells

cultured alone (monoculture) or cultured with IL4-MΦ (co-cultured). The wilcoxon

statistic for the permutation (black) was compared to the wilcoxon statistic comparing

the true mono-culture and co-culture MT track distributions (red). (B) Box plots show the

distribution of MT track orientation and cellular coherence features. Each point overlaid

on the box plot corresponds to an individual MT track from an ES2 EB3-mApple cell

grown in monoculture (red) or in co-culture with IL4-MΦ (blue)(red line denotes median).

(A-B) N=1,424 tracks across n=33 total ES2 cells were analyzed. All box plots are

defined as Q1/25%tile, median, Q3/75%tile with outliers falling outside Q3/Q1±1.5*IQR.

control co-culture
Y-27632 (ROCK inhibitor)
IPI-549 (Pi3kγ inhibitor)
erlotinib (EGFR inhibitor)
AXL FC Chimera
anti-Integrin β1 mAb
anti-CSF1R mAb
serabelisib (Pi3kα inhibitor)
UNC2025 (MERTK inhibitor)
AZD6482 (Pi3kβ inhibitor)
R848 (TLR7/8 agonist)
AMG319 (Pi3kδ inhibitor)
control monoculture

ES2 IL4-MΦ co-culture

Treatment Condition

control co-culture
Y-27632 (ROCK inhibitor)
IPI-549 (Pi3kγ inhibitor)
erlotinib (EGFR inhibitor)
AXL FC Chimera
anti-Integrin β1 mAb
anti-CSF1R mAb
serabelisib (Pi3kα inhibitor)
UNC2025 (MERTK inhibitor)
AZD6482 (Pi3kβ inhibitor)
R848 (TLR7/8 agonist)
AMG319 (Pi3kδ inhibitor)
control monoculture

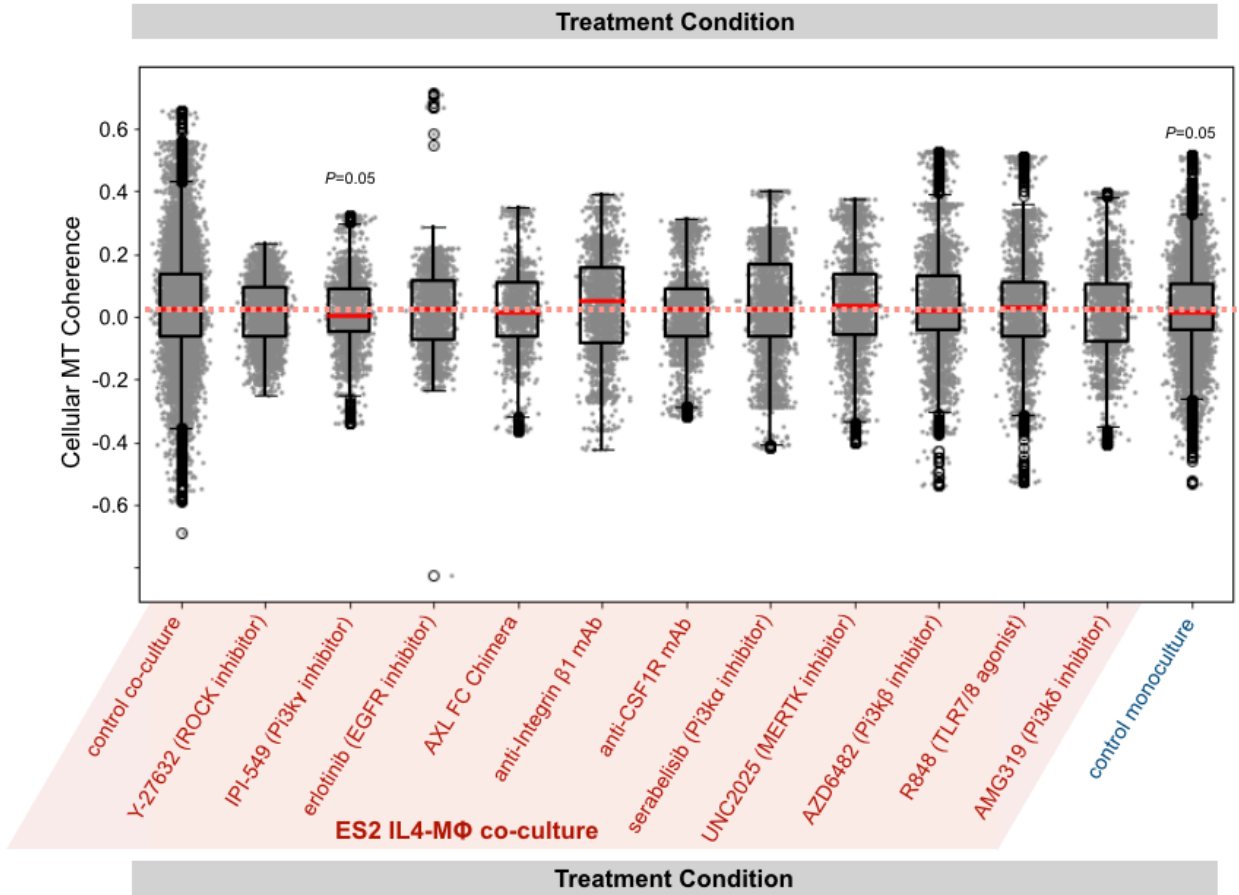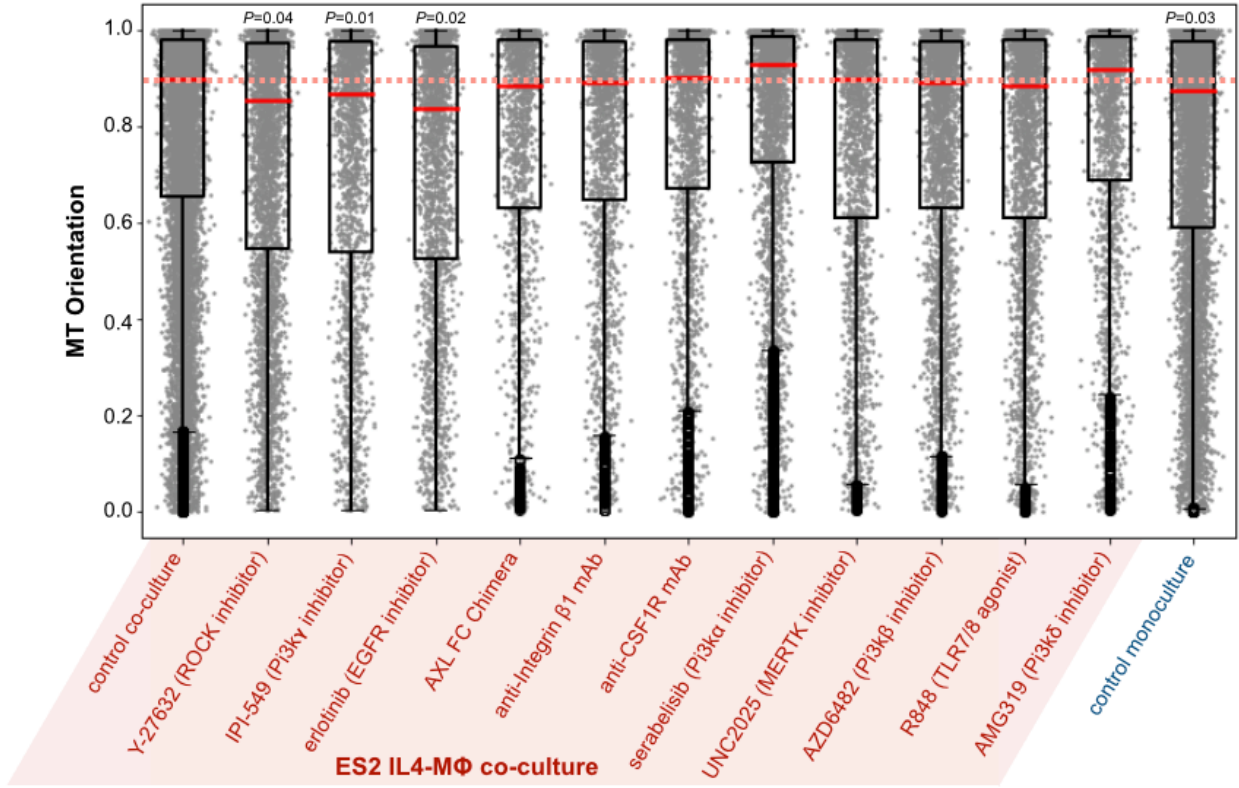ES2 IL4-MΦ co-culture

Treatment Condition

153

Figure C-5 ES2 MT dynamics in response to targeted reagents and drugs.

Corresponding to Figure 3-4, MT orientation and coherence were measured following treatment with the indicated targeted compounds in ES2-EB3-mApple cells, shown as single-track distributions (*two-tailed permutation test comparing treatment with untreated co-culture; n=10,968 tracks from n=118 total cells). Box plot bars represent the minimum, 25%tile, median, 75%tile, and maximum values.
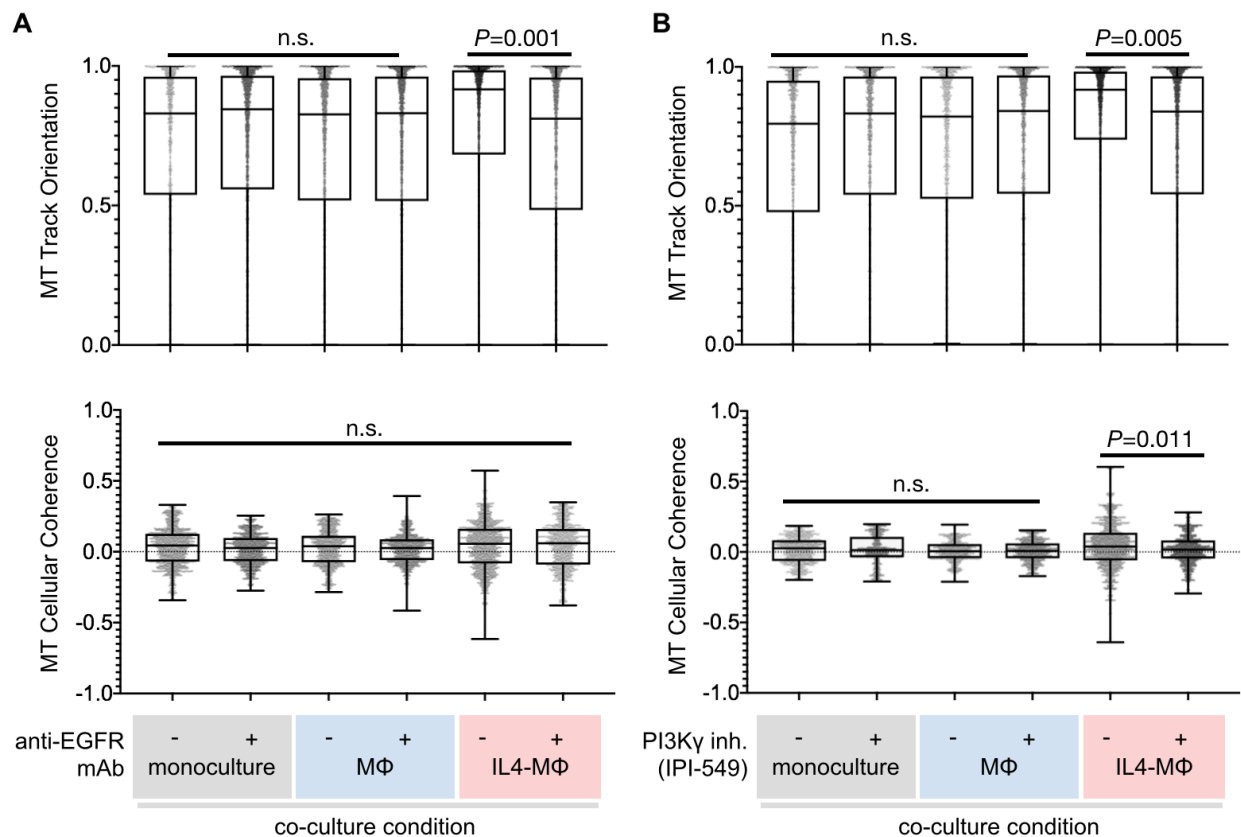
Figure C-6. HT1080 MT dynamics in response to targeted reagents and drugs.

Corresponding to Figure 3-5 and Figure 9-18, single-track distributions are shown for

HT1080-EB3-mApple cells following treatment with anti-EGFR antibody (A: n=13,380

tracks from n=80 total cells) and IPI-549 (B: n=16,427 tracks from n=112 total cells).

Box plot bars represent the minimum, 25%tile, median, 75%tile, and maximum values.

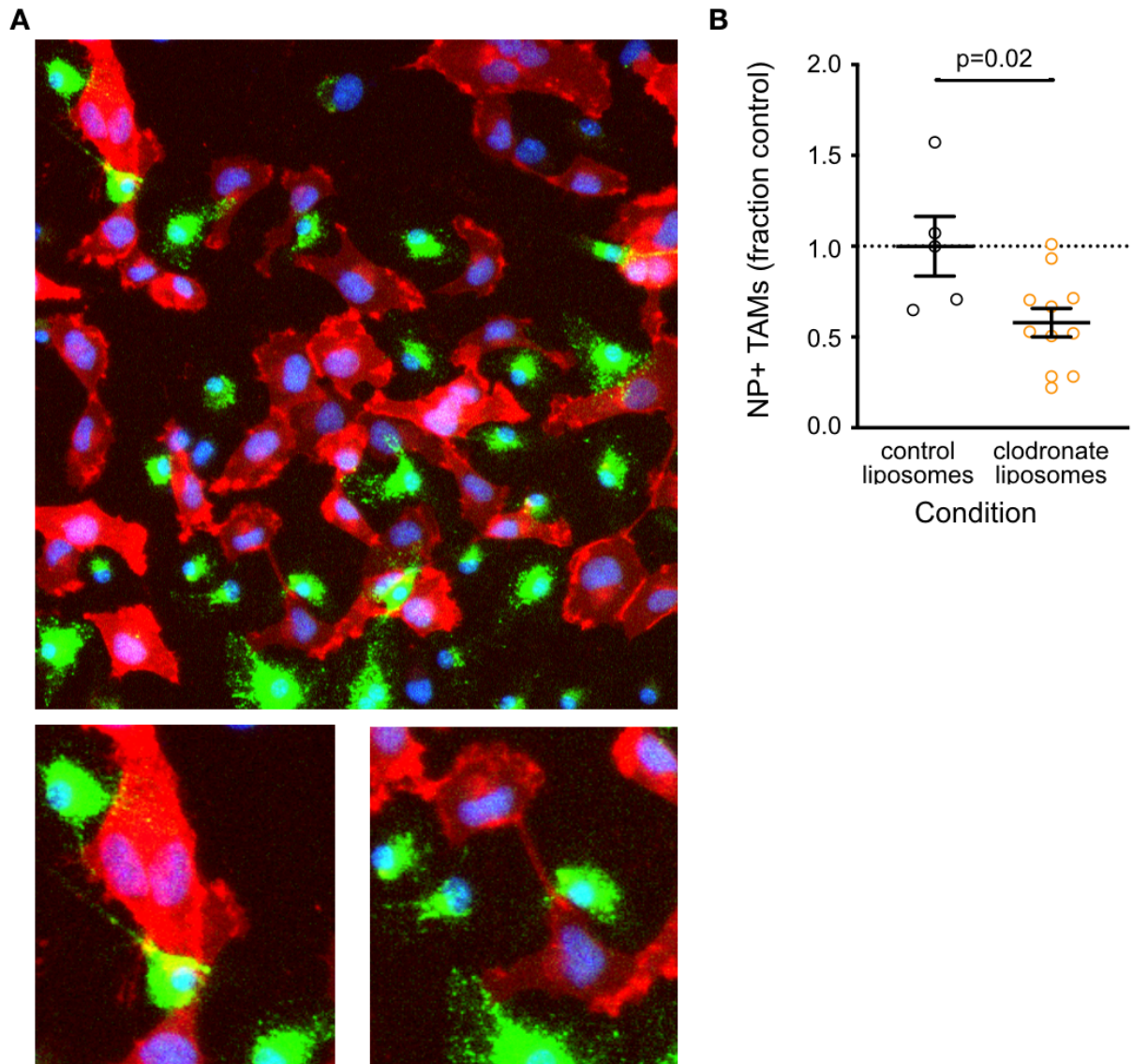Significance values were computed using a two-tailed permutation test.

Figure C-8 (A) Representative images of HT1080-mem-mApple cells in co-culture with

NP-labeled IL4-MΦ, highlighting instances of co-localized MΦ and tumor cell protrusion.

(B) Quantification of NP+ cells to determine relative MΦ content present in

intraperitoneal ES2-mClover tumors (two tailed unpaired t-test; n=16 tumors; error bars

denote mean±s.e.m.). Signficance tests used in linear regression analysis(A-D)

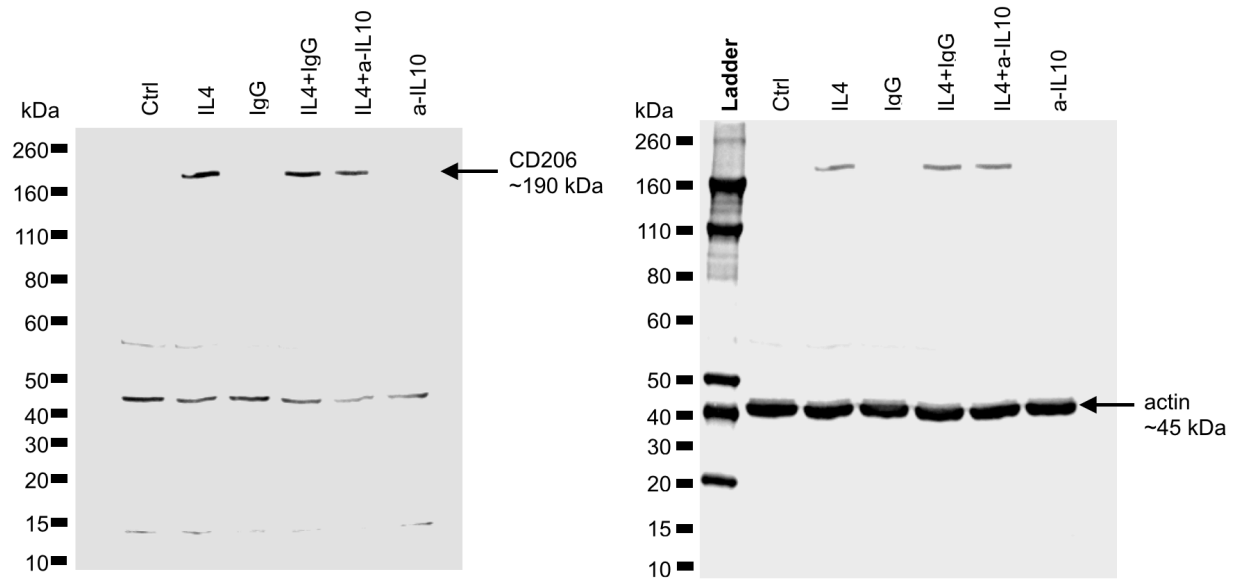measure if slope is significantly nonzero.

Figure C-9. (C) Full image of blot corresponding to Figure 3-16. The blot was probed

first with rabbit anti-CD206 primary antibody, followed by anti-rabbit secondary antibody

(left). The blot was washed and then probed with mouse anti-actin primary antibody,

followed by anti-mouse secondary antibody (right). CD206 band in the blot on the right

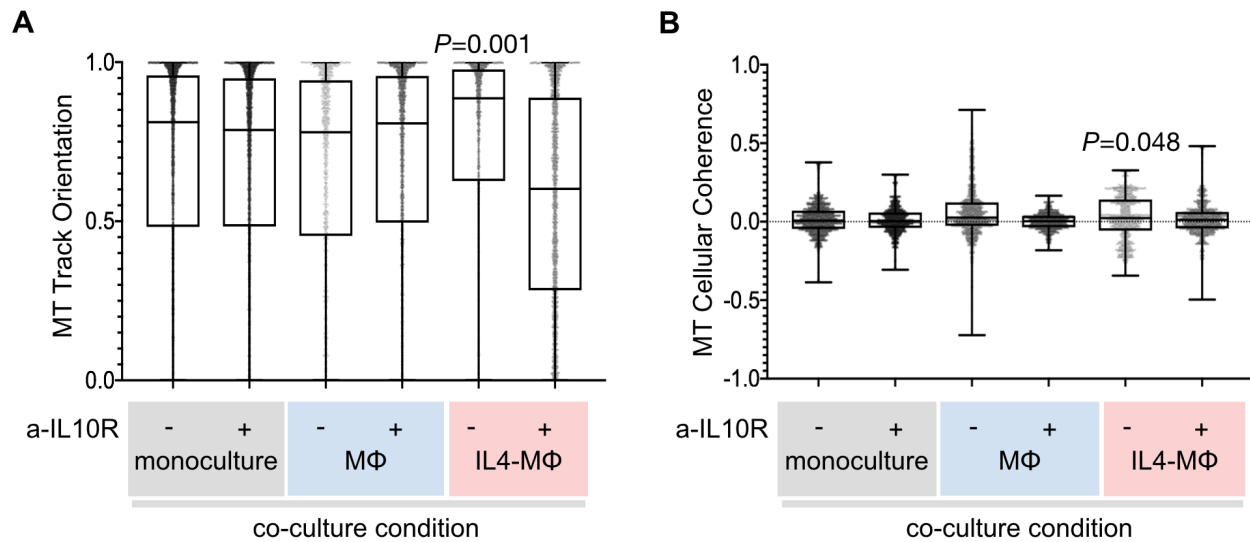is the result of residual HRP activity from the first blot.

Figure C-10. The effect of Anti-IL10R antibody treatment on MT dynamics. MT

orientation (A) and coherence (B) of HT1080-EB3-mApple cells were measured

following treatment with anti-IL10R antibody (A-B: n=21,218 tracks from 99 total cells).

Significance values were computed by a two tailed permutation comparing two groups:

IL4-MΦ co-culture vs all other cells. Box plot bars represent the minimum, 25%tile,
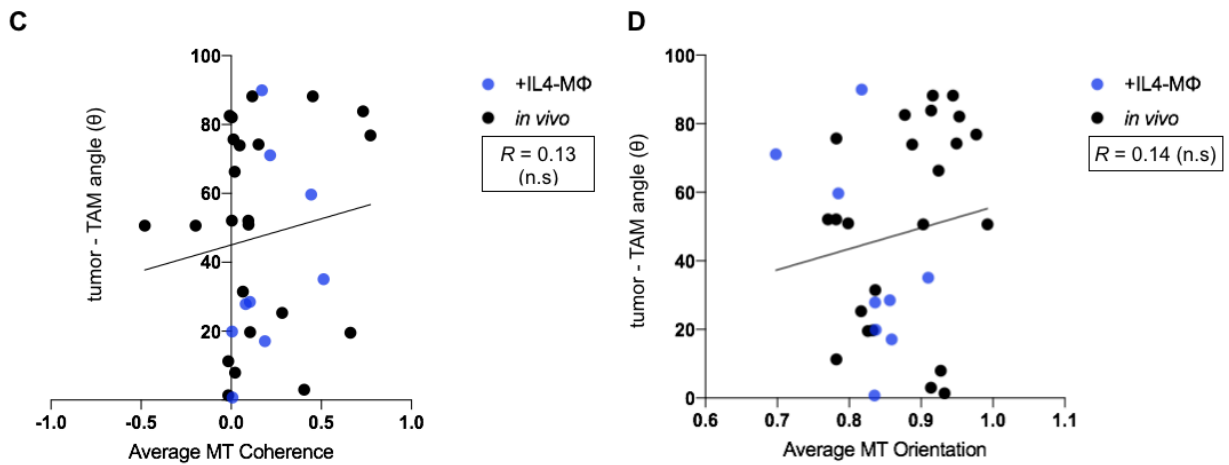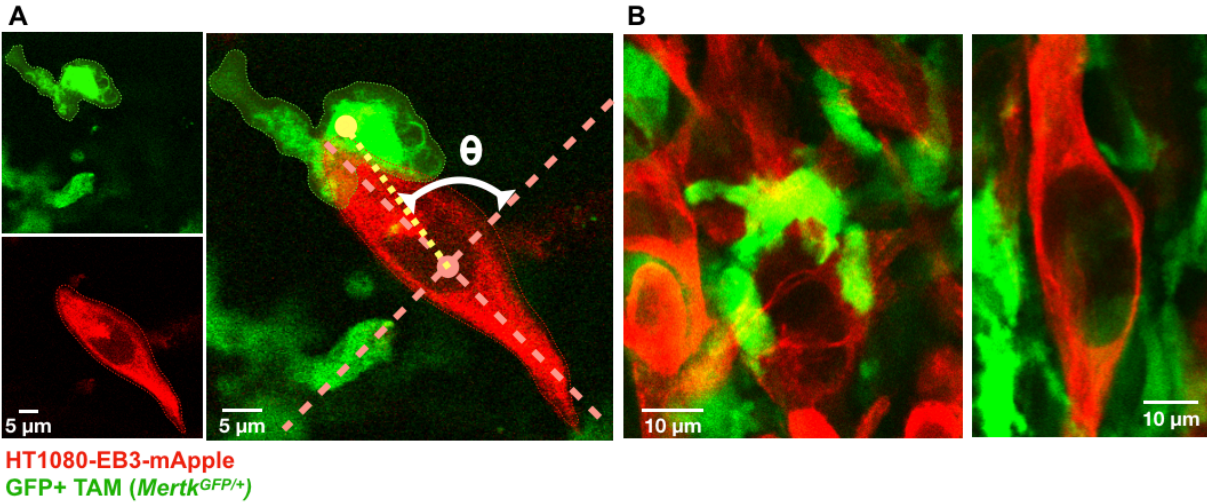
median, 75%tile, and maximum values.

Figure C-11. (A) Example of tumor cell near a TAM located at its major length axis, for which quantification of "tumor-macrophage angle" is possible, in this case leading to a cosine value near 1.0. (B) Such "tumor-macrophage angles" cannot be calculated from cases where no single TAM can be assigned as nearest to the tumor cell, and therefore were excluded from analysis of "tumor-macrophage angles." (B-D) Cell-by-cell quantification of cellular MT coherence (C) and orientation (D) relative to the measured tumor-macrophage angle (C-D: *two-tailed F-test; n=32 cells).

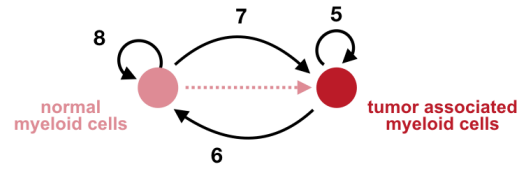# Appendix D Supplementary Information for Chapter 4

A

Epithelial - Epithelial Interactions (I - 4)
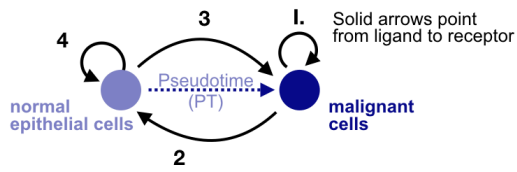
Myeloid - Myeloid Interactions (5 - 9)

Fibroblast - Fibroblast Interactions (9-12)
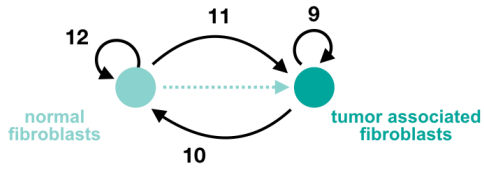
Epithelial - Myeloid Interactions (13 - 20)
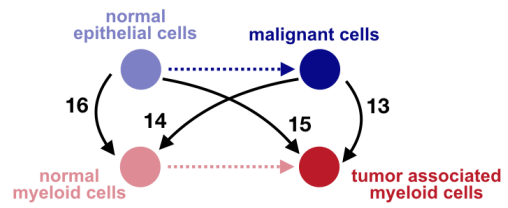
Epithelial - Fibroblast Interactions (21-28)
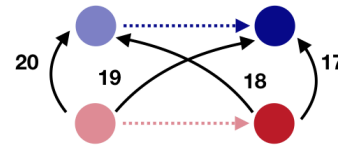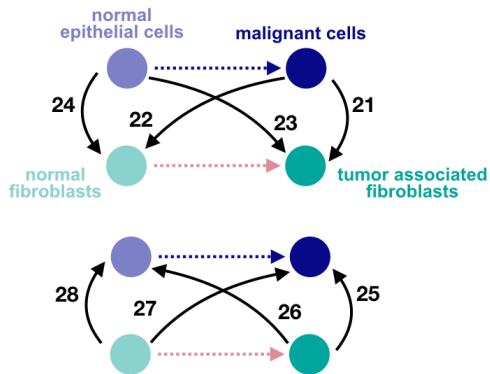
Figure C-1 (continued on the next page)

161

B

162
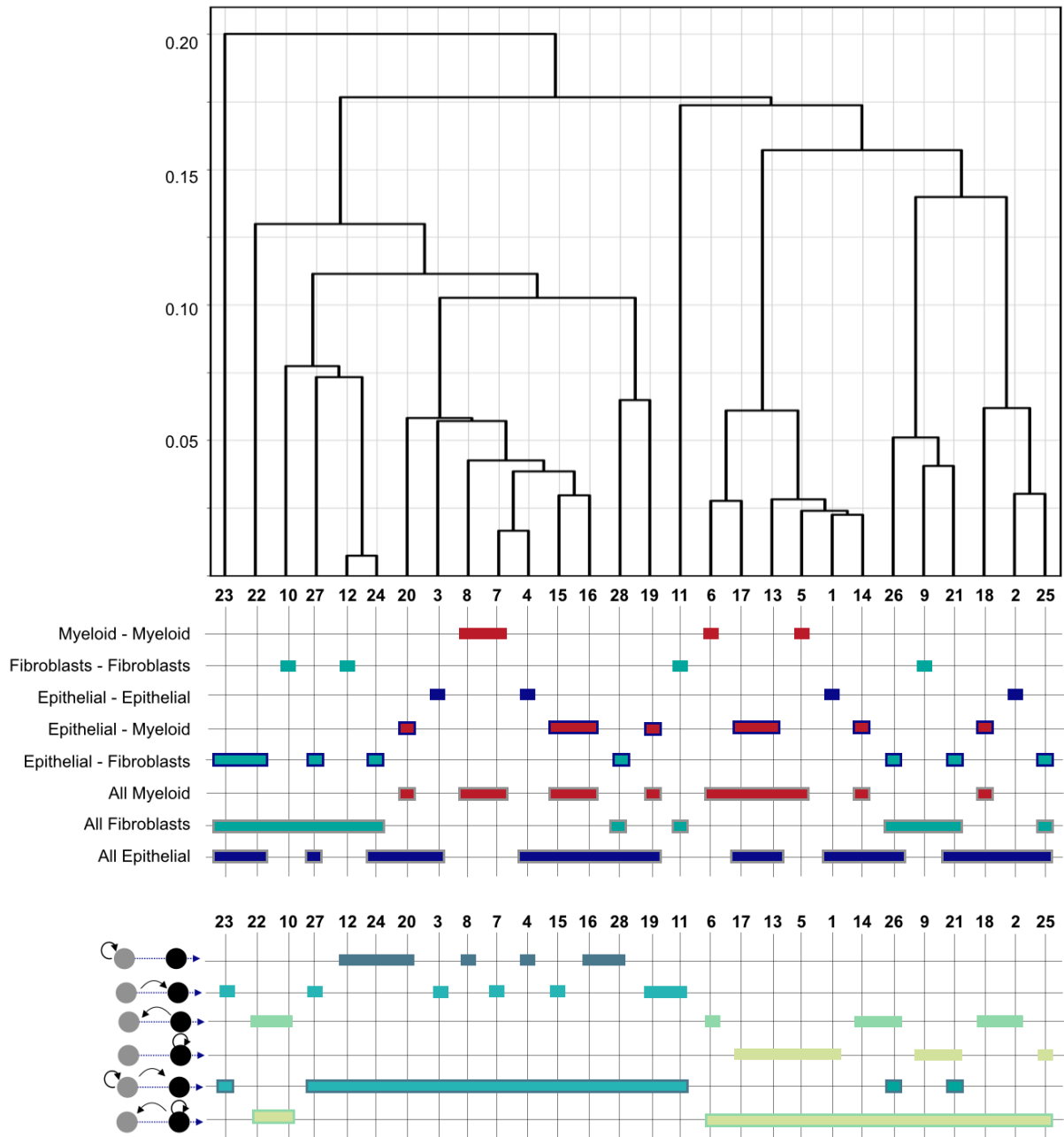
Figure C-1. PCA analysis was performed on Ligand-Receptor x Interaction pattern

matrix (example shown in Figure 4-5). Based on euclidean distances in PCA space a

clustergram was created for each of the 28 different interaction patterns (A). To

visualize specific patterns, each interaction was grouped by cell type (middle)and

signaling pattern (bottom). The signaling patterns from A clustered more strongly

together based on the directionality of signaling rather than the cell type involved.

Appendix E References

1. Regev, A. et al. The Human Cell Atlas. *Elife* **6**, (2017).

2. Tabula, M. C. A single-cell transcriptomic atlas characterizes ageing tissues in the mouse. *Nature* **583**, 590-595 (2020).

3. HuBMAP, C. The human body at cellular resolution: the NIH Human Biomolecular Atlas Program. *Nature* **574**, 187-192 (2019).

4. Deubner, J., Coulon, P. & Diester, I. Optogenetic approaches to study the mammalian brain. *Curr Opin Struct Biol* **57**, 157-163 (2019).

5. Purvis, J. E. & Lahav, G. Encoding and decoding cellular information through signaling dynamics. *Cell* **152**, 945-956 (2013).

6. Jeknić, S., Kudo, T. & Covert, M. W. Techniques for Studying Decoding of Single Cell Dynamics. *Front Immunol* **10**, 755 (2019).

7. Woodhouse, S., Piterman, N., Wintersteiger, C. M., Göttgens, B. & Fisher, J. SCNS: a graphical tool for reconstructing executable regulatory networks from single-cell genomic data. *BMC Syst Biol* **12**, 59 (2018).

8. Thurley, K., Wu, L. F. & Altschuler, S. J. Modeling Cell-to-Cell Communication Networks Using Response-Time Distributions. *Cell Syst* **6**, 355-367.e5 (2018).

9. Armingol, E., Officer, A., Harismendy, O. & Lewis, N. E. Deciphering cell-cell interactions and communication from gene expression. *Nat Rev Genet* **22**, 71-88 (2021).

10. Mehta, A. K. et al. Targeting immunosuppressive macrophages overcomes PARP inhibitor resistance in BRCA1-associated triple-negative breast cancer. *Nature Cancer* 1-17 (2020).

11. Wang, S. J. et al. Efficient blockade of locally reciprocated tumor-macrophage signaling using a TAM-avid nanotherapy. *Sci Adv* **6**, eaaz8521 (2020).

12. Zomer, A. et al. In Vivo imaging reveals extracellular vesicle-mediated phenocopying of metastatic behavior. *Cell* **161**, 1046-1057 (2015).

13. Stevenson, A. J. et al. Multiscale imaging of basal cell dynamics in the functionally mature mammary gland. *Proc Natl Acad Sci U S A* **117**, 26822-26832 (2020).

14. Luthria, G. et al. In vivo microscopy reveals macrophage polarization locally promotes coherent microtubule dynamics in migrating cancer cells. *Nat Commun* **11**, 3521 (2020).

15. Baccin, C. et al. Combined single-cell and spatial transcriptomics reveal the molecular, cellular and spatial bone marrow niche organization. *Nat Cell Biol* **22**, 38-48 (2020).

16. Picelli, S. et al. Smart-seq2 for sensitive full-length transcriptome profiling in single cells. *Nat Methods* **10**, 1096-1098 (2013).

17. Macosko, E. Z. et al. Highly Parallel Genome-wide Expression Profiling of Individual Cells Using Nanoliter Droplets. *Cell* **161**, 1202-1214 (2015).

18. Zheng, G. X. et al. Massively parallel digital transcriptional profiling of single cells. *Nat Commun* **8**, 14049 (2017).

19. Gierahn, T. M. et al. Seq-Well: portable, low-cost RNA sequencing of single cells at high throughput. *Nat Methods* **14**, 395-398 (2017).

20. Kumar, M. P. et al. Analysis of Single-Cell RNA-Seq Identifies Cell-Cell Communication Associated with Tumor Characteristics. *Cell Rep* **25**, 1458-1468.e4 (2018).

21. Browaeys, R., Saelens, W. & Saeys, Y. NicheNet: modeling intercellular communication by linking ligands to target genes. *Nat Methods* **17**, 159-162 (2020).

22. Skelly, D. A. et al. Single-Cell Transcriptional Profiling Reveals Cellular Diversity and Intercommunication in the Mouse Heart. *Cell Rep* **22**, 600-610 (2018).

23. Efremova, M., Vento-Tormo, M., Teichmann, S. A. & Vento-Tormo, R. CellPhoneDB: inferring cell-cell communication from combined expression of multi-subunit ligand-receptor complexes. *Nat Protoc* **15**, 1484-1506 (2020).

24. Jin, S. et al. Inference and analysis of cell-cell communication using CellChat. *bioRxiv* **doi**, 10.1101/2020.07.21.214387 (2020).

25. Noël, F. et al. ICELLNET: a transcriptome-based framework to dissect intercellular communication. *bioRxiv* **doi**, 10.1101/2020.03.05.976878 (2020).

26. Holland, C. H. et al. Robustness and applicability of transcription factor and pathway analysis tools on single-cell RNA-seq data. *Genome Biol* **21**, 36 (2020).

27. Qiu, X. et al. Inferring Causal Gene Regulatory Networks from Coupled Single-Cell Expression Dynamics Using Scribe. *Cell Syst* **10**, 265-274.e11 (2020).

28. Specht, A. T. & Li, J. LEAP: constructing gene co-expression networks for single-cell RNA-sequencing data using pseudotime ordering. *Bioinformatics* **33**, 764-766 (2017).

29. Lin, J. R. et al. Highly multiplexed immunofluorescence imaging of human tissues and tumors using t-CyCIF and conventional optical microscopes. *Elife* **7**, (2018).

30. Goltsev, Y. et al. Deep Profiling of Mouse Splenic Architecture with CODEX Multiplexed Imaging. *Cell* **174**, 968-981.e15 (2018).

31. Giesen, C. et al. Highly multiplexed imaging of tumor tissues with subcellular resolution by mass cytometry. *Nat Methods* **11**, 417-422 (2014).

32. Rodriques, S. G. et al. Slide-seq: A scalable technology for measuring genome-wide expression at high spatial resolution. *Science* **363**, 1463-1467 (2019).

33. Ståhl, P. L. et al. Visualization and analysis of gene expression in tissue sections by spatial transcriptomics. *Science* **353**, 78-82 (2016).

34. Lee, J. H. et al. Fluorescent in situ sequencing (FISSEQ) of RNA for gene expression profiling in intact cells and tissues. *Nat Protoc* **10**, 442-458 (2015).

35. Wang, X. et al. Three-dimensional intact-tissue sequencing of single-cell transcriptional states. *Science* **361**, (2018).

36. Kishi, J. Y. et al. SABER amplifies FISH: enhanced multiplexed imaging of RNA and DNA in cells and tissues. *Nat Methods* **16**, 533-544 (2019).

37. Schapiro, D. et al. histoCAT: analysis of cell phenotypes and interactions in multiplex image cytometry data. *Nat Methods* **14**, 873-876 (2017).

38. Stoltzfus, C. R. et al. CytoMAP: A Spatial Analysis Toolbox Reveals Features of Myeloid Cell Organization in Lymphoid Tissues. *Cell Rep* **31**, 107523 (2020).

39. Färkkilä, A. et al. Immunogenomic profiling determines responses to combined PARP and PD-1 inhibition in ovarian cancer. *Nat Commun* **11**, 1459 (2020).

40. Krueger, R. et al. Facetto: Combining Unsupervised and Supervised Learning for Hierarchical Phenotype Analysis in Multi-Channel Image Data. *IEEE Trans Vis Comput Graph* **26**, 227-237 (2020).

41. Cang, Z. & Nie, Q. Inferring spatial and signaling relationships between cells from single cell transcriptomic data. *Nat Commun* **11**, 2084 (2020).

42. Oyler-Yaniv, A. et al. A Tunable Diffusion-Consumption Mechanism of Cytokine Propagation Enables Plasticity in Cell-to-Cell Communication in the Immune System. *Immunity* **46**, 609-620 (2017).

43. Thibaut, R. et al. Bystander IFN-γ activity promotes widespread and sustained cytokine signaling altering the tumor microenvironment. *Nat Cancer* **1**, 302-314 (2020).

44. Hoekstra, M. E. et al. Long-distance modulation of bystander tumor cells by CD8^{+} T cell-secreted IFNγ. *Nat Cancer* **1**, 291-301 (2020).

45. Garris, C. S. et al. Successful Anti-PD-1 Cancer Immunotherapy Requires T Cell-Dendritic Cell Crosstalk Involving the Cytokines IFN-γ and IL-12. *Immunity* **49**, 1148-1161.e7 (2018).

46. Agliardi, G. et al. Intratumoral IL-12 delivery empowers CAR-T cell immunotherapy in a pre-clinical model of glioblastoma. *Nat Commun* **12**, 444 (2021).

47. Boulch, M. et al. A cross-talk between CAR T cell subsets and the tumor microenvironment is essential for sustained cytotoxic activity. *Sci Immunol* **6**, (2021).

48. Daassi, D., Mahoney, K. M. & Freeman, G. J. The importance of exosomal PDL1 in tumour immune evasion. *Nat Rev Immunol* **20**, 209-215 (2020).

49. Pucci, F. et al. SCS macrophages suppress melanoma by restricting tumor-derived vesicle-B cell interactions. *Science* **352**, 242-246 (2016).

50. Meyer, A. S., Zweemer, A. J. & Lauffenburger, D. A. The AXL Receptor is a Sensor of Ligand Spatial Heterogeneity. *Cell Syst* **1**, 25-36 (2015).

51. Choi, S. et al. Corticosterone inhibits GAS6 to govern hair follicle stem-cell quiescence. *Nature* (2021).

52. Hirata, E. et al. Intravital imaging reveals how BRAF inhibition generates drug-tolerant microenvironments with high integrin β1/FAK signaling. *Cancer Cell* **27**, 574-588 (2015).

53. Oki, T. et al. Imaging dynamic mTORC1 pathway activity in vivo reveals marked shifts that support time-specific inhibitor therapy in AML. *Nat Commun* **12**, 245 (2021).

54. Hiratsuka, T., Bordeu, I., Pruessner, G. & Watt, F. M. Regulation of ERK basal and pulsatile activity control proliferation and exit from the stem cell compartment in mammalian epidermis. *Proc Natl Acad Sci U S A* **117**, 17796-17807 (2020).

55. Muta, Y. et al. Composite regulation of ERK activity dynamics underlying tumour-specific traits in the intestine. *Nat Commun* **9**, 2174 (2018).

56. Kinjo, T. et al. FRET-assisted photoactivation of flavoproteins for in vivo two-photon optogenetics. *Nat Methods* **16**, 1029-1036 (2019).

57. Regot, S., Hughey, J. J., Bajar, B. T., Carrasco, S. & Covert, M. W. High-sensitivity measurements of multiple kinase activities in live single cells. *Cell* **157**, 1724-1734 (2014).

58. De Simone, A. et al. Control of osteoblast regeneration by a train of Erk activity waves. *Nature* (2021).

59. Simon, C. S., Rahman, S., Raina, D., Schröter, C. & Hadjantonakis, A. K. Live Visualization of ERK Activity in the Mouse Blastocyst Reveals Lineage-Specific Signaling Dynamics. *Dev Cell* **55**, 341-353.e5 (2020).

60. Gerosa, L. et al. Receptor-Driven ERK Pulses Reconfigure MAPK Signaling and Enable Persistence of Drug-Adapted BRAF-Mutant Melanoma Cells. *Cell Syst* **11**, 478-494.e9 (2020).

61. Thurber, G. M., Schmidt, M. M. & Wittrup, K. D. Antibody tumor penetration: transport opposed by systemic and antigen-mediated clearance. *Adv Drug Deliv Rev* **60**, 1421-1434 (2008).

62. Miller, M. A. et al. Modular Nanoparticulate Prodrug Design Enables Efficient Treatment of Solid Tumors Using Bioorthogonal Activation. *ACS Nano* **12**, 12814-12826 (2018).

63. Ridley, A. J. Rho GTPase signalling in cell migration. *Curr Opin Cell Biol* **36**, 103-112 (2015).

64. Wittmann, T. & Waterman-Storer, C. M. Cell motility: can Rho GTPases and microtubules point the way. *J Cell Sci* **114**, 3795-3803 (2001).

65. Mitchison, T. & Kirschner, M. Dynamic instability of microtubule growth. *Nature* **312**, 237-242 (1984).

66. Gittes, F., Mickey, B., Nettleton, J. & Howard, J. Flexural rigidity of microtubules and actin filaments measured from thermal fluctuations in shape. *J Cell Biol* **120**, 923-934 (1993).

67. Ridley, A. J. et al. Cell migration: integrating signals from front to back. *Science* **302**, 1704-1709 (2003).

68. Prentice-Mott, H. V. et al. Directional memory arises from long-lived cytoskeletal asymmetries in polarized chemotactic cells. *Proc Natl Acad Sci U S A* **113**, 1267-1272 (2016).

69. Etienne-Manneville, S. Microtubules in cell migration. *Annu Rev Cell Dev Biol* **29**, 471-499 (2013).

70. Chaffer, C. L. & Weinberg, R. A. A perspective on cancer cell metastasis. *Science* **331**, 1559-1564 (2011).

71. Fletcher, D. A. & Mullins, R. D. Cell mechanics and the cytoskeleton. *Nature* **463**, 485-492 (2010).

72. Bouchet, B. P. & Akhmanova, A. Microtubules in 3D cell motility. *J Cell Sci* **130**, 39-50 (2017).

73. Dogterom, M. & Koenderink, G. H. Actin-microtubule crosstalk in cell biology. *Nat Rev Mol Cell Biol* **20**, 38-54 (2019).

74. Bouchet, B. P. et al. Mesenchymal Cell Invasion Requires Cooperative Regulation of Persistent Microtubule Growth by SLAIN2 and CLASP1. *Dev Cell* **39**, 708-723 (2016).

75. Kim, H. D. et al. Epidermal growth factor-induced enhancement of glioblastoma cell migration in 3D arises from an intrinsic increase in speed but an extrinsic matrix- and proteolysis-dependent increase in persistence. *Mol Biol Cell* **19**, 4249-4259 (2008).

76. Li, R. et al. Macrophage-Secreted TNFα and TGFβ1 Influence Migration Speed and Persistence of Cancer Cells in 3D Tissue Culture via Independent Pathways. *Cancer Res* **77**, 279-290 (2017).

77. Meyer, A. S. et al. 2D protrusion but not motility predicts growth factor-induced cancer cell migration in 3D collagen. *J Cell Biol* **197**, 721-729 (2012).

78. Carey, S. P. et al. Comparative mechanisms of cancer cell migration through 3D matrix and physiological microtracks. *Am J Physiol Cell Physiol* **308**, C436-47 (2015).

79. Kikuchi, K. & Takahashi, K. WAVE2- and microtubule-dependent formation of long protrusions and invasion of cancer cells cultured on three-dimensional extracellular matrices. *Cancer Sci* **99**, 2252-2259 (2008).

80. Oyanagi, J., Ogawa, T., Sato, H., Higashi, S. & Miyazaki, K. Epithelial-mesenchymal transition stimulates human cancer cells to extend microtubule-based invasive protrusions and suppresses cell growth in collagen gel. *PLoS One* **7**, e53209 (2012).

81. Miller, M. A. & Weissleder, R. Imaging the pharmacology of nanomaterials by intravital microscopy: Toward understanding their biological behavior. *Adv Drug Deliv Rev* **113**, 61-86 (2017).

82. Matov, A. et al. Analysis of microtubule dynamic instability using a plus-end growth marker. *Nat Methods* **7**, 761-768 (2010).

83. Shaner, N. C. et al. Improving the photostability of bright monomeric orange and red fluorescent proteins. *Nat Methods* **5**, 545-551 (2008).

84. Stepanova, T. et al. Visualization of microtubule growth in cultured neurons via the use of EB3-GFP (end-binding protein 3-green fluorescent protein). *J Neurosci* **23**, 2655-2664 (2003).

85. Miller, M. A. et al. Modular Nanoparticulate Prodrug Design Enables Efficient Treatment of Solid Tumors Using Bioorthogonal Activation. *ACS Nano* (2018).

86. Pineda, J. J. et al. Site occupancy calibration of taxane pharmacology in live cells and tissues. *Proc Natl Acad Sci U S A* **115**, E11406-E11414 (2018).

87. Velez, D. O. et al. 3D collagen architecture induces a conserved migratory and transcriptional response linked to vasculogenic mimicry. *Nat Commun* **8**, 1651 (2017).

88. Petrie, R. J. & Yamada, K. M. At the leading edge of three-dimensional cell migration. *J Cell Sci* **125**, 5917-5926 (2012).

89. Chittajallu, D. R. et al. In vivo cell-cycle profiling in xenograft tumors by quantitative intravital microscopy. *Nat Methods* **12**, 577-585 (2015).

90. Laughney, A. M. et al. Single-cell pharmacokinetic imaging reveals a therapeutic strategy to overcome drug resistance to the microtubule inhibitor eribulin. *Sci Transl Med* **6**, 261ra152 (2014).

91. Miller, M. A. et al. Predicting therapeutic nanomedicine efficacy using a companion magnetic resonance imaging nanoparticle. *Sci Transl Med* **7**, 314ra183 (2015).

92. Applegate, K. T. et al. plusTipTracker: Quantitative image analysis software for the measurement of microtubule dynamics. *J Struct Biol* **176**, 168-184 (2011).

93. Salaycik, K. J., Fagerstrom, C. J., Murthy, K., Tulu, U. S. & Wadsworth, P. Quantification of microtubule nucleation, growth and dynamics in wound-edge cells. *J Cell Sci* **118**, 4113-4122 (2005).

94. Komarova, Y. A., Vorobjev, I. A. & Borisy, G. G. Life cycle of MTs: persistent growth in the cell interior, asymmetric transition frequencies and effects of the cell boundary. *J Cell Sci* **115**, 3527-3539 (2002).

95. Han, W. et al. Oriented collagen fibers direct tumor cell intravasation. *Proc Natl Acad Sci U S A* **113**, 11208-11213 (2016).

96. Kimura, K. et al. Endoplasmic-reticulum-mediated microtubule alignment governs cytoplasmic streaming. *Nat Cell Biol* **19**, 399-406 (2017).

97. Myers, K. A., Applegate, K. T., Danuser, G., Fischer, R. S. & Waterman, C. M. Distinct ECM mechanosensing pathways regulate microtubule dynamics to control endothelial cell branching morphogenesis. *J Cell Biol* **192**, 321-334 (2011).

98. Olson, D. J., Oh, D. & Houston, D. W. The dynamics of plus end polarization and microtubule assembly during Xenopus cortical rotation. *Dev Biol* **401**, 249-263 (2015).

99. Kleele, T. et al. An assay to image neuronal microtubule dynamics in mice. *Nat Commun* **5**, 4827 (2014).

100. Garcez, P. P. et al. Cenpj/CPAP regulates progenitor divisions and neuronal migration in the cerebral cortex downstream of Ascl1. *Nat Commun* **6**, 6474 (2015).

101. Ahmad, F. J., Pienkowski, T. P. & Baas, P. W. Regional differences in microtubule dynamics in the axon. *J Neurosci* **13**, 856-866 (1993).

102. Li, R. et al. Interstitial flow promotes macrophage polarization toward an M2 phenotype. *Mol Biol Cell* **29**, 1927-1940 (2018).

103. Miller, M. A. et al. Tumour-associated macrophages act as a slow-release reservoir of nano-therapeutic Pt(IV) pro-drug. *Nat Commun* **6**, 8692 (2015).

104. Thorsson, V. et al. The Immune Landscape of Cancer. *Immunity* **48**, 812-830.e14 (2018).

105. Lewis, C. E. & Pollard, J. W. Distinct role of macrophages in different tumor microenvironments. *Cancer Res* **66**, 605-612 (2006).

106. Engblom, C., Pfirschke, C. & Pittet, M. J. The role of myeloid cells in cancer therapies. *Nat Rev Cancer* **16**, 447-462 (2016).

107. Miller, M. A. et al. Radiation therapy primes tumors for nanotherapeutic delivery via macrophage-mediated vascular bursts. *Sci Transl Med* **9**, eaal0225 (2017).

108. Mohan, J. F. et al. Imaging the emergence and natural progression of spontaneous autoimmune diabetes. *Proc Natl Acad Sci U S A* **114**, E7776-E7785 (2017).

109. Cook, R. S. et al. MerTK inhibition in tumor leukocytes decreases tumor growth and metastasis. *J Clin Invest* **123**, 3231-3242 (2013).

110. Wallet, M. A. et al. MerTK regulates thymic selection of autoreactive T cells. *Proc Natl Acad Sci U S A* **106**, 4810-4815 (2009).

111. Jaguin, M., Houlbert, N., Fardel, O. & Lecureur, V. Polarization profiles of human M-CSF-generated macrophages and comparison of M1-markers in classically activated macrophages from GM-CSF and M-CSF origin. *Cell Immunol* **281**, 51-61 (2013).

112. Rodell, C. B. et al. TLR7/8-agonist-loaded nanoparticles promote the polarization of tumour-associated macrophages to enhance cancer immunotherapy. *Nat Biomed Eng* **2**, 578-588 (2018).

113. Goswami, S. et al. Macrophages promote the invasion of breast carcinoma cells via a colony-stimulating factor-1/epidermal growth factor paracrine loop. *Cancer Res* **65**, 5278-5283 (2005).

114. Hernandez, L. et al. The EGF/CSF-1 paracrine invasion loop can be triggered by heregulin beta1 and CXCL12. *Cancer Res* **69**, 3221-3227 (2009).

115. Lee, C. H. et al. Tumor-associated macrophages promote oral cancer progression through activation of the Axl signaling pathway. *Ann Surg Oncol* **21**, 1031-1037 (2014).

116. Mantovani, A., Sica, A. & Locati, M. Macrophage polarization comes of age. *Immunity* **23**, 344-346 (2005).

117. Takatori, N., Oonuma, K., Nishida, H. & Saiga, H. Polarization of PI3K Activity Initiated by Ooplasmic Segregation Guides Nuclear Migration in the Mesendoderm. *Dev Cell* **35**, 333-343 (2015).

118. Kaneda, M. M. et al. PI3Kγ is a molecular switch that controls immune suppression. *Nature* **539**, 437-442 (2016).

119. Hendriks, H. R. et al. Comparative antitumour activity of vinblastine-isoleucinate and related vinca alkaloids in human tumour xenografts. *Eur J Cancer* **28A**, 767-773 (1992).

120. Kim, H. Y. et al. Quantitative Imaging of Tumor Associated Macrophages and Their Response to Therapy Using 64Cu-Labeled Macrin. *ACS Nano* (2018).

121. Zeisberger, S. M. et al. Clodronate-liposome-mediated depletion of tumour-associated macrophages: a new and highly effective antiangiogenic therapy approach. *Br J Cancer* **95**, 272-281 (2006).

122. Ip, W. K. E., Hoshi, N., Shouval, D. S., Snapper, S. & Medzhitov, R. Anti-inflammatory effect of IL-10 mediated by metabolic reprogramming of macrophages. *Science* **356**, 513-519 (2017).

123. Baseler, W. A. et al. Autocrine IL-10 functions as a rheostat for M1 macrophage glycolytic commitment by tuning nitric oxide production. *Redox Biol* **10**, 12-23 (2016).

124. Tirosh, I. et al. Dissecting the multicellular ecosystem of metastatic melanoma by single-cell RNA-seq. *Science* **352**, 189-196 (2016).

125. Puram, S. V. et al. Single-Cell Transcriptomic Analysis of Primary and Metastatic Tumor Ecosystems in Head and Neck Cancer. *Cell* **171**, 1611-1624.e24 (2017).

126. Shih, A. J. et al. Identification of grade and origin specific cell populations in serous epithelial ovarian cancer by single cell RNA-seq. *PLoS One* **13**, e0206785 (2018).

127. Miller, M. A. et al. Targeting autocrine HB-EGF signaling with specific ADAM12 inhibition using recombinant ADAM12 prodomain. *Sci Rep* **5**, 15150 (2015).

128. Zhang, W. et al. Polarization of macrophages in the tumor microenvironment is influenced by EGFR signaling within colon cancer cells. *Oncotarget* **7**, 75366-75378 (2016).

129. Reemst, K., Noctor, S. C., Lucassen, P. J. & Hol, E. M. The Indispensable Roles of Microglia and Astrocytes during Brain Development. *Front Hum Neurosci* **10**, 566 (2016).

130. Norden, D. M., Trojanowski, P. J., Walker, F. R. & Godbout, J. P. Insensitivity of astrocytes to interleukin 10 signaling following peripheral immune challenge results in prolonged microglial activation in the aged brain. *Neurobiol Aging* **44**, 22-41 (2016).

131. Almolda, B. et al. Alterations in microglial phenotype and hippocampal neuronal function in transgenic mice with astrocyte-targeted production of interleukin-10. *Brain Behav Immun* **45**, 80-97 (2015).

132. Afik, R. et al. Tumor macrophages are pivotal constructors of tumor collagenous matrix. *J Exp Med* **213**, 2315-2331 (2016).

133. Li, R. et al. Single-Cell Intravital Microscopy of Trastuzumab Quantifies Heterogeneous in vivo Kinetics. *Cytometry A* (2019).

134. Weinreb, C., Wolock, S. & Klein, A. M. SPRING: a kinetic interface for visualizing high dimensional single-cell expression data. *Bioinformatics* **34**, 1246-1248 (2018).

135. Pardoll, D. M. The blockade of immune checkpoints in cancer immunotherapy. *Nat Rev Cancer* **12**, 252-264 (2012).

136. Ramilowski, J. A. et al. A draft network of ligand-receptor-mediated multicellular signalling in human. *Nat Commun* **6**, 7866 (2015).

137. Chen, H. et al. Single-cell trajectories reconstruction, exploration and mapping of omics data with STREAM. *Nat Commun* **10**, 1903 (2019).

138. Haghverdi, L., Büttner, M., Wolf, F. A., Buettner, F. & Theis, F. J. Diffusion pseudotime robustly reconstructs lineage branching. *Nat Methods* **13**, 845-848 (2016).

139. Van den Berge, K. et al. Trajectory-based differential expression analysis for single-cell sequencing data. *Nat Commun* **11**, 1201 (2020).

140. Cook, D. P. & Vanderhyden, B. C. Context specificity of the EMT transcriptional response. *Nat Commun* **11**, 2142 (2020).

141. Zeisberg, M. & Neilson, E. G. Biomarkers for epithelial-mesenchymal transitions. *J Clin Invest* **119**, 1429-1437 (2009).

142. Wang, Q. et al. CircCSPP1 Functions as a ceRNA to Promote Colorectal Carcinoma Cell EMT and Liver Metastasis by Upregulating COL1A1. *Front Oncol* **10**, 850 (2020).

143. Parker, M. W. et al. Fibrotic extracellular matrix activates a profibrotic positive feedback loop. *J Clin Invest* **124**, 1622-1635 (2014).

144. Tieng, F. Y. F. et al. Single Cell Transcriptome in Colorectal Cancer-Current Updates on Its Application in Metastasis, Chemoresistance and the Roles of Circulating Tumor Cells. *Front Pharmacol* **11**, 135 (2020).

145. Lee, H. O. et al. Lineage-dependent gene expression programs influence the immune landscape of colorectal cancer. *Nat Genet* **52**, 594-603 (2020).

146. Gulhati, P. et al. mTORC1 and mTORC2 regulate EMT, motility, and metastasis of colorectal cancer via RhoA and Rac1 signaling pathways. *Cancer Res* **71**, 3246-3256 (2011).

147. Du, L. et al. CD44 is of functional importance for colorectal cancer stem cells. *Clin Cancer Res* **14**, 6751-6760 (2008).

148. Wang, S., Karikomi, M., MacLean, A. L. & Nie, Q. Cell lineage and communication network inference via optimization for single-cell transcriptomics. *Nucleic Acids Res* **47**, e66 (2019).

149. Traag, V. A., Waltman, L. & van Eck, N. J. From Louvain to Leiden: guaranteeing well-connected communities. *Sci Rep* **9**, 5233 (2019).

150. Martinez, F. O. & Gordon, S. The M1 and M2 paradigm of macrophage activation: time for reassessment. *F1000Prime Rep* **6**, 13 (2014).

151. Weissleder, R. & Pittet, M. J. The expanding landscape of inflammatory cells affecting cancer therapy. *Nat Biomed Eng* **4**, 489-498 (2020).

152. Georgiou, T., Liu, Y., Chen, W. & Lew, M. A survey of traditional and deep learning-based feature descriptors for high dimensional data in computer vision. *International Journal of Multimedia Information Retrieval* **9**, 135-170 (2020).

153. Wang, H. & Schmid, C. Action recognition with improved trajectories. **Proceedings of the IEEE international conference on computer vision**, 3551-3558 (2013).

154. Xiao, X., Hu, H. & Wang, W. Trajectories-based motion neighborhood feature for human action recognition. **2017 IEEE International Conference on Image Processing**, 4147-4151 (2017).

155. Vickovic, S. et al. High-definition spatial transcriptomics for in situ tissue profiling. *Nat Methods* **16**, 987-990 (2019).

156. Lubeck, E., Coskun, A. F., Zhiyentayev, T., Ahmad, M. & Cai, L. Single-cell in situ RNA profiling by sequential hybridization. *Nat Methods* **11**, 360-361 (2014).

157. Chen, K. H., Boettiger, A. N., Moffitt, J. R., Wang, S. & Zhuang, X. RNA imaging. Spatially resolved, highly multiplexed RNA profiling in single cells. *Science* **348**, aaa6090 (2015).

158. Saka, S. K. et al. Immuno-SABER enables highly multiplexed and amplified protein imaging in tissues. *Nat Biotechnol* **37**, 1080-1090 (2019).

159. Ko, J., Oh, J., Ahmed, M. S., Carlson, J. C. T. & Weissleder, R. Ultra-fast Cycling for Multiplexed Cellular Fluorescence Imaging. *Angew Chem Int Ed Engl* **59**, 6839-6846 (2020).

160. Alon, S. et al. Expansion sequencing: Spatially precise in situ transcriptomics in intact biological systems. *Science* **371**, (2021).

161. Susaki, E. A. et al. Advanced CUBIC protocols for whole-brain and whole-body clearing and imaging. *Nat Protoc* **10**, 1709-1727 (2015).

162. Sartori-Rupp, A. et al. Correlative cryo-electron microscopy reveals the structure of TNTs in neuronal cells. *Nat Commun* **10**, 342 (2019).

163. Gottschalk, S. et al. Rapid volumetric optoacoustic imaging of neural dynamics across the mouse brain. *Nat Biomed Eng* **3**, 392-401 (2019).

164. Sun, S., Zhu, J. & Zhou, X. Statistical analysis of spatial expression patterns for spatially resolved transcriptomic studies. *Nat Methods* **17**, 193-200 (2020).

165. Cable, D. M. et al. Robust decomposition of cell type mixtures in spatial transcriptomics. *Nat Biotechnol* (2021).

166. Edsgärd, D., Johnsson, P. & Sandberg, R. Identification of spatial expression trends in single-cell gene expression data. *Nat Methods* **15**, 339-342 (2018).

167. Svensson, V., Teichmann, S. A. & Stegle, O. SpatialDE: identification of spatially variable genes. *Nat Methods* **15**, 343-346 (2018).

168. Li, D., Ding, J. & Bar-Joseph, Z. Identifying signaling genes in spatial single cell expression data. *Bioinformatics* (2020).

169. Dries, R. et al. Giotto, a pipeline for integrative analysis and visualization of single-cell spatial transcriptomic data. *bioRxiv* **doi**, 10.1101/701680 (2019).

170. Schiebinger, G. et al. Optimal-Transport Analysis of Single-Cell Gene Expression Identifies Developmental Trajectories in Reprogramming. *Cell* **176**, 1517 (2019).

171. Upadhaya, S. et al. Intravital Imaging Reveals Motility of Adult Hematopoietic Stem Cells in the Bone Marrow Niche. *Cell Stem Cell* **27**, 336-345.e4 (2020).